



**The
Research
Experience
for
Undergraduates
Program**

**Research
Accomplishments
2000**

Table of Contents

| | | | |
|--|-----------|--|-----------|
| The NNUN REU 2000 Participants | 2 | Stanford Nanofabrication Facility | 53 |
| The NNUN Research Experience for Undergraduates Program, 2000 | 3 | Molecular Beam Epitaxy of Nanostructures | 54 |
| The National Nanofabrication Users Network | 4 | Electrical Conductivity in Oriented DNA | 56 |
| <i>THE NNUN REU RESEARCH ACCOMPLISHMENTS, 2000</i> | | Novel Carbon Nanotube Tips: En Route to High Resolution and Ultra Sensitive Force Detection in Magnetic Force Microscopy | 58 |
| Cornell Nanofabrication Facility | 5 | High Resolution Imaging with a Uniform Axial Magnetic Field | 60 |
| Curved Silicon Electronics | 6 | Electrical Conductivity in Oriented DNA | 62 |
| Lithographic Evaluation of Acrylate-Based Cycloaliphatic Copolymers | 8 | Deactivation Kinetics of Supersaturated, Laser Annealed Dopants in Silicon | 64 |
| Development of Plasma Etching Processes for the Fabrication of Porous Vertical Structures | 10 | A Microfluidic Device for DNA Analysis by Pyrosequencing | 66 |
| Fabrication of a Microscale SPR Device | 12 | Releasing Metal Cantilever Beams for Use as Switches in MicroElectroMechanical Systems (MEMS) | 68 |
| Controlling Cell Motility Using Microfabrication Technology | 14 | Aspect Ratio Dependant Microtrenching in High-Density Plasma Etched Microstructures | 70 |
| Studies of Silicon Surface Migration in the Formation of Sub-Surface Voids | 16 | Etch Characterization of Nb Disks for Superconductor Penetration Depth Measurements | 72 |
| Evaluation of Collagen as a Membrane Material | 18 | Wet-Oxidation of Digitally Alloyed AlGaAs | 74 |
| Nanofabrication and Optimization of Organic Thin Film Transistors | 20 | Characterization of the Aspect Ratio Dependent Etch for MicroElectroMechanical Systems (MEMS) | 76 |
| Creating a Sapphire Substrate for the Growth of Gallium Nitride | 22 | University of California Santa Barbara | 79 |
| Damascene Tungsten and Polycrystalline Silicon in an Oxide Matrix | 24 | Spin Transport Across Interfaces | 80 |
| Patterning Polymeric Materials | 26 | Stress in Thick GaN-Films | 82 |
| Howard University | 29 | Synthesis and Characterization of Low-Dimensional Materials Using Non-Lithographic Techniques | 84 |
| Excessive Nutrients in the Anacostia and Potomac Rivers | 30 | Fabrication of Ordered Arrays of InAs Quantum Dots | 86 |
| Engineering Porphyrin Encapsulated Vesicles for Metal Removal from Wastewater | 32 | Self Assembled Monolayers of Alkanethiols on Gold Substrates | 88 |
| SiC Retina for Subretinal Applications | 34 | Ferromagnetic Clusters and Annealed GaMnAs | 90 |
| Organic Material Binding to Inorganic Material at a Nanoscale Level | 36 | Characterization of InGaAs Oxide Aperture HBTs | 92 |
| The Penn State Nanofabrication Facility | 39 | The Dynamic Phase Behavior of a Biological Monolayer System | 94 |
| Coating & Etching Glass Substrates for DNA Microarray | 40 | 400-500 μm Etching of Silicon | 96 |
| Mass Spectrometry Analysis of Ubiquitin on Deposited Column/Void Network Silicon Thin Films | 42 | Index | 98 |
| The Absorption Kinetics of des-Pro ³ ,[Ala ² ,6]-Bradykinin on Deposited Column/Void Network Silicon Thin Films .. | 44 | | |
| Electrical Properties of TEOS in MIM Structures | 46 | | |
| Fabrication of Silicon Masters for Micro-Contact Printing ... | 48 | | |
| Silver Writing by Laser-Liquid Interaction Technique | 50 | | |

The NNUN REU Interns, 2000

| Intern | School Affiliation | Field of Study | NNUN SITE | Page |
|----------------------------------|----------------------------------|-----------------------|------------------|-------------|
| Ms. Karen Ahle | Harvey Mudd College | Engr | SNF | 54 |
| Mr. Leonid Viktorovich Alekseyev | CalTech | Physics/EE | CNF | 6 |
| Ms. Anna Asanbaeva | UCLA | ChemEng/Biomed | SNF | 56 |
| Mr. David Badillo Torres | University of PR Aguadilla | Bio/MicroBio | PSU | 40 |
| Mr. Austin Brown | Harvey Mudd College | Physics/CompSci | UCSB | 80 |
| Ms. Kwanza Nicole Brown | Eastern College | Bio/PreMed | PSU | 42 |
| Ms. Molly Burton | Adams State College | Bio / Chem | CNF | 8 |
| Mr. Van Ortega Cayetano | New York University | Chem/ChemEngr | SNF | 58 |
| Mr. Steven Charles | Brigham Young University | MechEngr/Math | UCSB | 82 |
| Mr. Charlie Alexander Collins II | Lincoln University | Chem /Business | UCSB | 84 |
| Mr. Luis Jose Cruz-Rivera | Prairie View A&M University | EE | SNF | 60 |
| Ms. Nga Nguyet Dinh | University of Nebraska Lincoln | BioChem | PSU | 44 |
| Mr. Erik Douglas | Purdue University | EE | SNF | 62 |
| Mr. William Fadgen | University of Texas Dallas | Physics | PSU | 46 |
| Ms. Flora Felsovalyi | Cornell University | AgBioEngr | CNF | 10 |
| Mr. Andrew Gapin | Georgia Inst of Technology | MatSci | UCSB | 86 |
| Mr. Nicarter Gordon | University of the Virgin Islands | Biology | UCSB | 88 |
| Ms. Nathalie Guébels | UCSB | EE | UCSB | 90 |
| Mr. Jesus Angel Tena Guzman | UCSB | EE | UCSB | 92 |
| Mr. Corey Harris | Washington University (St Louis) | ChemEng | SNF | 64 |
| Mr. Scott Harrison | Rice University | ChemEng | SNF | 66 |
| Ms. Tamisha Hawkins | Xavier University of Louisiana | Bio PreMed | Howard | 30 |
| Mr. Jeremy Hoff | Duke University | BioMed/EE | CNF | 12 |
| Mr. Jonathan Hong | University of Pennsylvania | BioEngr | CNF | 14 |
| Mr. Jesse Hwang | Yale University | MechEngr | SNF | 68 |
| Mr. Jevon Johnson | Xavier University of Louisiana | Biology/Chem | PSU | 48 |
| Ms. Andrea Lewis | Princeton University | ChemEng | Howard | 32 |
| Ms. Wendi Maeda | University of Hawaii Manoa | EE | CNF | 16 |
| Ms. Jenea McLaughlin | University of Pennsylvania | BioEngr | Howard | 34 |
| Ms. Kieche Meleson | UCSB | Chem | UCSB | 94 |
| Mr. Aghapi Mordovanaki | University of MI Dearborn | EE/Physics | SNF | 70 |
| Ms. Catherine Newman | University of CA Berkeley | MechEngr | CNF | 18 |
| Ms. Ly Xuan Thi Nguyen | Colorado State University | Biochem | PSU | 50 |
| Ms. Sasha Rodriguez Gonzalez | Louisiana State University / PR | Industrial Engr | Howard | 36 |
| Mr. Jason Slinker | Southern Nazarene University | Physics/Chem/Math | CNF | 20 |
| Ms. Sharelle Speller | Spelman College | ChemEng | CNF | 22 |
| Ms. Virginia Starke | NM Inst of Mining and Tech | Physics/Math | CNF | 24 |
| Ms. Jennifer Sui | University of CA Davis | Chem/Psych | CNF | 26 |
| Mr. Eric Taketatsu | University of Hawaii Manoa | EE | SNF | 72 |
| Ms. Andrea Tao | Harvard University | Chem/Physics | SNF | 74 |
| Mr. Christopher Utley | UCSB | EE | UCSB | 96 |
| Mr. James Ryan Williams | Santa Clara University | PhysicsEngr | SNF | 76 |

The NNUN Research Experience for Undergraduates Program, 2000



The NNUN REU Convocation at The Pennsylvania State University, August 2000

Early in 2000, the NSF generously accepted the NNUN's REU proposal, and we moved forward with our second series of programs, this time with three years of helpful and successful experience to lead us.

For the NNUN REU Program 2000, we awarded forty-two internships to students from thirty-five colleges and universities — nineteen women, and twenty-five minority students, and we gave each of them the unique opportunity to try on a challenging, frustrating, and exciting new career, for ten weeks. Each site offered up a summer of exploration and research, encouraging their interns to absorb a vast amount of information, sometimes in disciplines new to the student, and involving them in cutting-edge nanotechnology resources.

But perhaps we should let the students speak for themselves — from the evaluations. Here are a few of their responses:

"The REU made me seriously consider solid state and my subfield in Physics. Plans: Masters and Doctorate in Physics."

"The research will be very useful to me, especially the hands-on, experimental aspect of it ... I would recommend the program."

"I think the program made me want to obtain a Ph.D. more than I did before."

"I value the research experience I've gained ... it's an excellent opportunity."

"This was my first active research experience and it was great exposure. Encouraged me to pursue research in grad school."

"I am considering a career in microelectronics manufacturing. It has strongly influenced my choice to go to grad school ... I would strongly recommend [the program]."

"Before this summer I was a pre-med student, where now, after I've seen different opportunities through REU, I'm considering grad school for my future plans."

"My plans now change because I was going to medical school, but now I might attend graduate school first."

"It was really good to see what graduate level research was like and work on a real project."

We are indebted to Drs. Rajinder Khosla and Theresa Maldonado at NSF for their support and guidance. We also received financial support from the following corporations:

Agilent Technologies, Advanced Micro Devices, Analog Devices, Applied Materials, Bosch Corporation, Ericsson, Hewlett Packard, Infineon, Hitachi Ltd, IBM, Intel, Integrated Devices Technology, Lam Research, National Semiconductor, Panasonic, Philips, Taiwan, Semiconductor Manufacturing Co., Texas Instruments, Varian Semiconductor Equipment Associates, and Xerox.

And finally, I would like to thank my NNUN REU counterparts and cohorts — Denise, Marsha, Yvette, James, Lisa, Debbie, Jane, Mike, Liu-Yen and Holly. We had a grand summer! Thank you.

*Melanie-Claire Mallison
NNUN REU Program Coordinator*

The National Nanofabrication Users Network (NNUN)

URL: <http://www.nnun.org/>

Stanford Nanofabrication Facility

Prof. David M. Bloom, Director

Stanford University

Edward L. Ginzton Lab, 450 Via Palou

Stanford CA 94305-4085

Voice: 650-725-4893

Fax: (650-725-2288

URL: <http://www-snf.stanford.edu/>

Cornell Nanofabrication Facility

Prof. Sandip Tiwari, Director

CNF Knight Laboratory

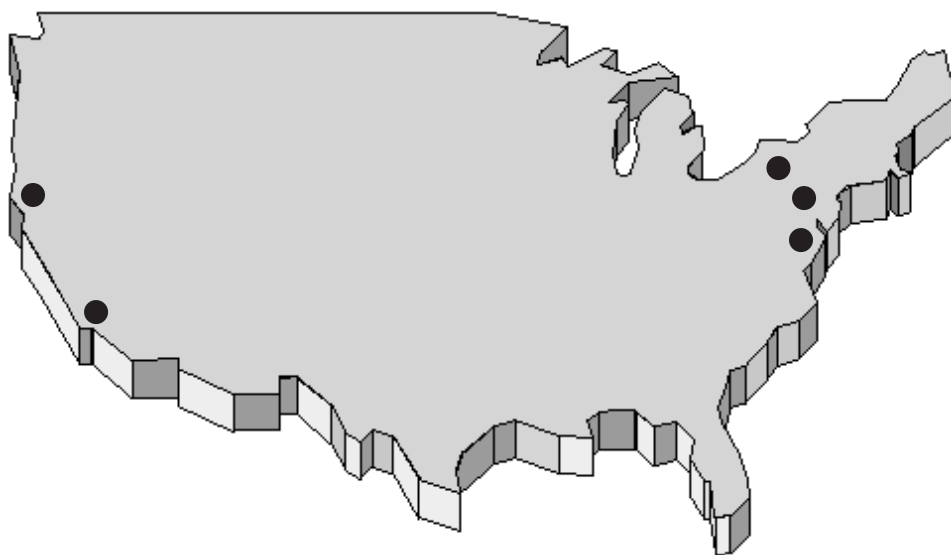
Cornell University

Ithaca, New York 14853-5403

Voice: (607) 255-2329

Fax: (607) 255-8601

URL: <http://www.cnf.cornell.edu/>



University of California at Santa Barbara

(UCSB) - Nanofabrication Facility

Prof. Evelyn Hu, Director

Department of Electrical & Computer Engineering

Santa Barbara, CA 93106-9560

Voice: (805) 893-4130

Fax: (805) 893-8170

URL: <http://www.nanotech.ucsb.edu/>

The Penn State Nanofabrication Facility

Prof. Stephen Fonash, Director

189 Materials Research Institute

The Pennsylvania State University

University Park, PA 16802

Voice: (814) 865-4931

Fax: (814) 865-3018

URL: <http://www.nanofab.psu.edu/>

Materials Science Center for Excellence

Prof. Gary Harris, Director

Howard University School of Engineering

2300 Sixth St, NW

Washington, D.C. 20059

Voice: (202) 806-6618

Fax: (202) 806-5367

URL: <http://www.msce.howard.edu/~nanonet/NNUN.HTM>

Cornell Nanofabrication Facility 2000 REU Participants



REU Intern

School Affiliation

Principal Investigator

Front Row:

| | | |
|-------------------------------|----------------------------------|-----------------|
| Ms. Wendi Maeda | University of Hawaii Manoa | Michael Skvarla |
| Ms. Sharelle Speller | Spelman College | Jack Blakely |
| Ms. Molly Burton | Adams State College | Dotsevi Sogah |
| Ms. Jennifer Sui | University of CA Davis | Chris Ober |
| Mr. Leonid V. Alekseyev | CalTech | Dieter Ast |

Back Row:

| | | |
|----------------------------|------------------------------------|------------------|
| Ms. Virginia Starke | NM Inst of Mining and Tech | Sandip Tiwari |
| Mr. Jason Slinker | Southern Nazarene University | George Malliaras |
| Mr. Jeremy Hoff | Duke University | Carl Batt |
| Ms. Catherine Newman | University of CA Berkeley | Michael Spencer |
| Mr. Jonathan Hong | University of Pennsylvania | Mark Saltzman |

Not Pictured:

| | | |
|----------------------------|--------------------------|----------------|
| Ms. Flora Felsovalyi | Cornell University | Hercules Neves |
|----------------------------|--------------------------|----------------|

Curved Silicon Electronics

REU Intern: Leonid Alekseyev, Physics Dept, Stanford University

Principal Investigator: Dieter Ast, Materials Science & Engr, Cornell University, dast@msc.cornell.edu

Mentor: Danny Chen, Materials Science & Engr, Cornell University

Introduction:

A single lens produces an image focused on a spherical surface. In many optical systems, however, gathered light forms an image on a flat detection or recording medium (e.g. photographic film, or a CCD.) To produce a sharp, focused image in the plane of a flat detector, an optical system must employ many lens elements. Such an arrangement inherently decreases the system's light-gathering capabilities, narrows its field of view, and makes the optical apparatus bulky. These effects are highly undesirable in several applications — one prominent example being tactical or scientific image intensification systems.

An ability to put an image detector along a curvilinear focal plane would remedy these problems, producing lightweight and compact optical systems with high sensitivity and wide field of view. By far, the best example of a system with a curved image detection apparatus is the human eye, in which a single lens focuses on a curved retina, producing an impressive field of view and resolution.

The goal of this particular project was to investigate the feasibility of composing the image detector out of an array of small silicon tiles, bridged together by elastic, extensible interconnections. Such a device would be capable of closely conforming to a curved surface, while the inherent gaps between the tiles would be small enough to have relatively little effect on the quality of the resulting image.

Numerical Analysis:

An algorithm has been developed to calculate the coordinates of the corners of any given tile based on its position on the sphere. The algorithm represents each tile with two vectors, using the rotation matrixes to obtain the spatial configuration of tiles tangent to given points on the sphere. Based on this data, a numerical algorithm is being developed to calculate the optimal arrangement of the tiles on a sphere, and to calculate and possibly minimize the area of the gaps between adjacent tiles.

Approach:

Our approach to forming a curved surface was to process the Si wafer such that if the wafer would be 'cut' into many 1cm² sized tiles, the tiles would be held together by extensible Al metallization lines. To achieve this goal, the future tiles were connected by zig-zag metallization lines. Since there was a concern that cutting or cleaving the wafer into tiles might damage these lines, the lines were elevated above the plane of the wafer between future tiles. To achieve this elevation, stripes of photoresists or deposited oxide were used. After processing the wafer, grooves were cut in the back

of the wafer using a diamond saw such that the grooves were centered underneath these lines, fabricated on the front. Final separation of the tiles can then be done via cleaving or dry-etching.

Fabrication:

The fabrication of the devices involved using lithography and aluminum deposition to create a set of metallization air bridges, and subsequently cleaving the wafer into a set of interconnected chips. To make the metallization lines form air bridges, temporary, 2 mm wide, 3 μm thick release lines were first patterned along the location of future cleave lines using photoresist or PECVD oxide. A 1-2 μm layer of aluminum was subsequently blanket deposited on the wafer using either an e-beam evaporator, or a sputtering system. This layer was then patterned, using photolithography, to form deformable interconnections. One section of each interconnect used a snake-like 20 μm wide design to introduce a degree of elasticity and extensibility into the connections. Excess aluminum was removed using a wet etch process. A protective layer of photoresist was then deposited, and back-side alignment was performed to replicate the release layer pattern on the back of the

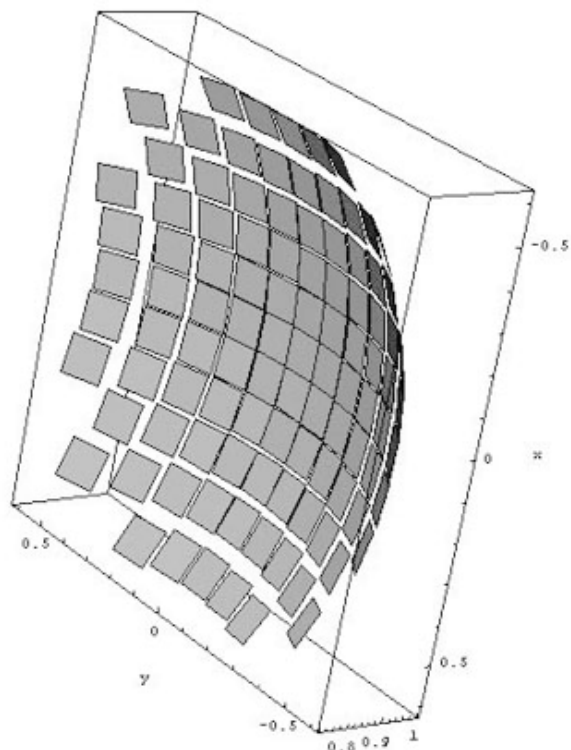


Figure 1: A mathematica rendering of square tiles on a spherical surface illustrates the geometry of the device we attempted to fabricate.

wafer, thereby marking the location of the cleave lines. Using these markings, a series of grooves was made on the back side of the wafer using a thin diamond wafering saw. The release layer was then removed, and the wafer cleaved into individual chips.

The majority of samples were manufactured using photoresist release layers. Unfortunately, photoresist created a less than ideal substrate for aluminum deposition, leading to some cratering, or in

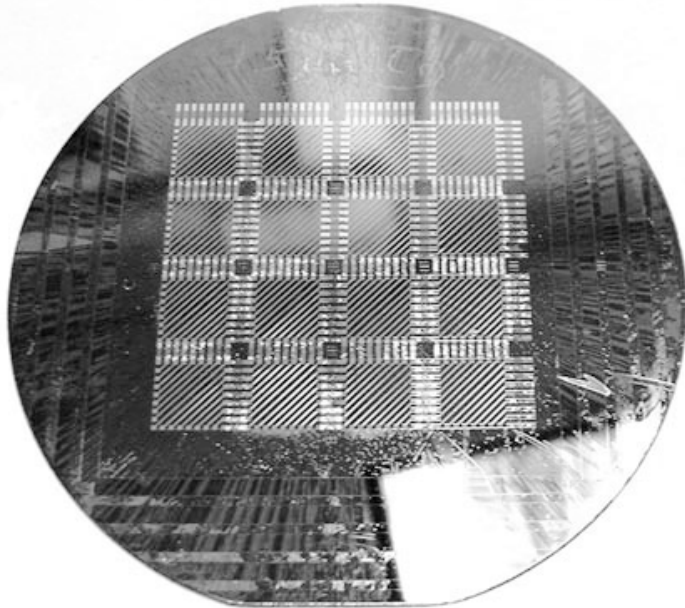


Figure 2: The wafer with patterned metallization lines before cleaving.

the extreme case, flaking in the aluminum film. The likely cause was heating of the photoresist (baked at a low temperature only) during the Al deposition. Most importantly, the majority of metallization lines were broken and washed off during the removal of photoresist. Using various methods of depositing aluminum, as well as various film thicknesses from 1 to 2 μm , proved to be ineffective against the destruction of interconnections.

Experiments have been being performed to investigate the use of release layers made out of PECVD oxide. Such release layers proved to be far less susceptible to stresses during the aluminum deposition, leading to a higher quality aluminum film. Disintegration of the metallization lines would be prevented by using wet etch to remove the release layers, a process putting less stress on the interconnections than removing photoresist release layers in acetone. 777 etch proved to be effective in removing PECVD oxide, while having no observable effects on the aluminum layer.

Furthermore, using a photo-imageable polyimide coating to pattern the aluminum lines was investigated. Such coatings strengthen the interconnections, and provided extra elasticity. Current samples are characterized by highly sloping walls in the imaged polyimide, effectively nearly doubling the width of metallization lines, but it should have no negative effects on the interconnections themselves.

Results and Conclusions:

Aluminum deposition via sputtering results in better adhesion of the film to the substrate than deposition through evaporation. Evaporating aluminum with a thin layer of chromium as a precursor

does not appear to increase adhesion by much. However, the sputtered film experiences higher stresses.

Photoresist release layers are easy to pattern and process, however photoresist cannot withstand the temperatures involved in sputtering combined with the stresses in sputtered aluminum film. SiO_2 presents a better, high-temperature resistant substrate for metal films, but it is more difficult to deposit and process.

In general, the aluminum interconnections appear to be easy to break (Figure 3) and wash away during the removal of the photoresist release layer. Using thicker aluminum films strengthen the connections somewhat, but the deposition and processing becomes more challenging as thicker films incur more stress. Reinforcing the connections with a layer of polyimide is a good way to strengthen the connections, however it brings in some processing difficulties as polyimide requires high-temperature cure (incompatible with photoresist release layer). In addition, the lithographic processing of polyimide is complicated.

Cutting the wafer to ensure easy cleaving while keeping the interconnections intact presents the greatest fabrication challenge. Using a laser scribe is complex and expensive, however it allows placing the cuts with great precision and uniformity. A wafer saw presents a much less delicate process, inducing mechanical vibrations in the wafer, and not giving satisfactory control over the placement of the cut and uniformity of the cut's depth. As a result of this, attempts to score the wafer for easy cleaving often resulted in cracks propagating along the cut, breaking the interconnections.

Future Work:

Fabrication of the devices using PECVD oxide as a release layer and with the aluminum interconnections strengthened with the photo-imageable polyimide will be attempted.

Subsequently, the usage of various etching techniques to etch grooves all the way from the backside of the wafer to the front, for the controlled cleaving of the wafer, might be studied. Additionally, using a different metal for interconnections might be explored.

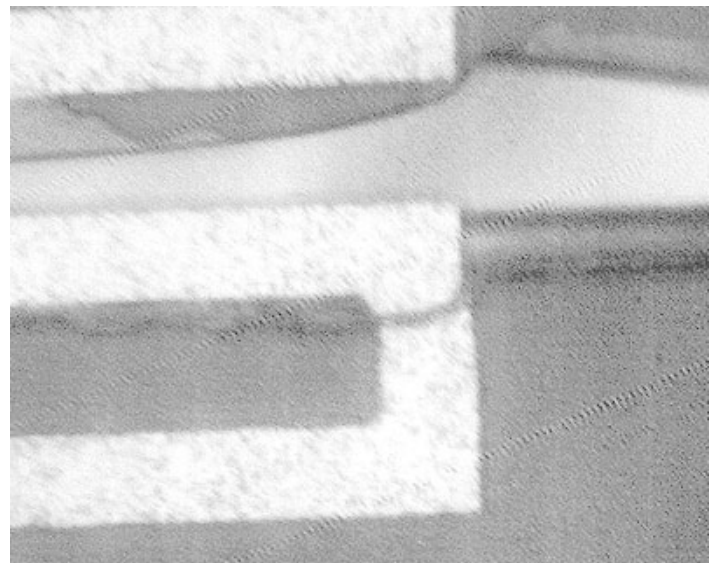


Figure 3: During cleaving of the wafer, cracks destroyed many Al interconnections.

Lithographic Evaluation of Acrylate-Based Cycloaliphatic Copolymers

REU Intern: Molly Burton, Biology and Chemistry, Adams State College

Principal Investigator: Dotsevi Sogah, Chemistry and ChemBio, Cornell University, dys2@cornell.edu

Mentor: Armah Kpissay, Chemistry and Chemical Biology, Cornell University

Abstract:

Chemically amplified resist, used in lithography, is a very important technology for the microelectronics industry. The trend of the industry is towards shorter wavelengths. Argon fluoride lithography (193nm) has problems with transparency, etch resistance, and solubility. In an attempt to better understand how these problems can be improved, polymers derived from optically active and racemic acrylate monomers will be used in a resist. Cycloaliphatic units will be incorporated into the main chain to enhance etch resistance and thermal stability. An acid-labile group, which allows for chemical amplification and aqueous base solubility, will also be part of the copolymer.

The focus of the project is to study the effect of acid content on the dissolution rate. Acrylate-based cycloaliphatic copolymers and homopolymers derived from (\pm) (R,R) endo,exo-bicyclo[2,2,2]-octane-2,3-dimethyl bisacrylate (TM6, TM7), and tetrahydropyranyl methacrylate (TM5) were prepared with varying acid compositions by free radical methods for use in ArF lithography.

Introduction:

A resist is a thin layer of polymeric material that is coated onto a substrate. The resist is modified to stay in some areas and is removed from others by exposure and development. Negative resist yields an insoluble, cross-linked polymer [1]. Negative resist also swells and is distorted in the dissolving process. For these reasons, positive resists are the choice of microlithography.

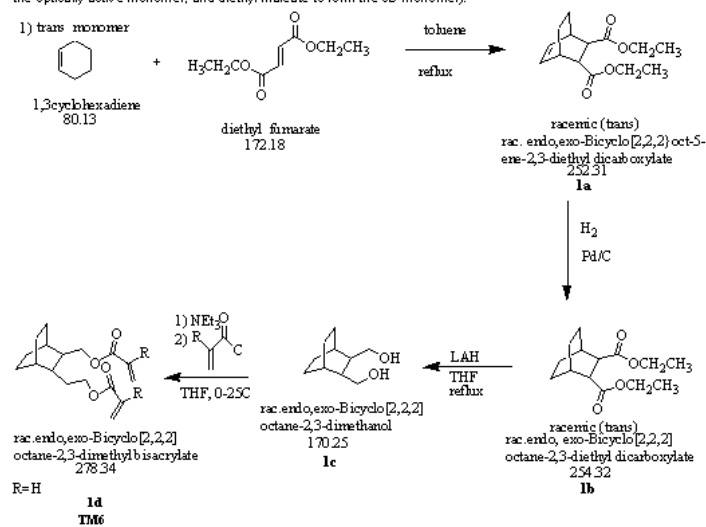
The dissolution rate is the rate at which the polymer is dissolved into a solvent. Interferometry is a relatively cheap and accurate way to measure the dissolution rate of thin polymer films. In addition, interferometry can provide information on the thickness of the transition layer between the dissolving polymer and the solvent [1-3]. A flat, polished silicon wafer coated with a polymer film of about 1.0 to 2.0 μm thickness is suspended in a vertical plane inside a transparent cylindrical container partially filled with a selected liquid [1, 3]. A beam of unpolarized light of wavelength 6328 \AA from a 2 mW He-Ne laser is directed obliquely at the film-coated substrate. The angle of incidence is typically 10° . The reflected light beam is collected by a silicon photocell coupled through a transimpedance amplifier to a chart recorder. The photocell operates in the zero bias photodiode mode so that the photocurrent is proportional to the intensity of light.

Argon fluoride lithography has problems with the transparency, etch resistance, and solubility of the polymers used [2]. In an attempt to better understand how these problems can be improved, acrylate-based cycloaliphatic copolymers will be used. Polymers

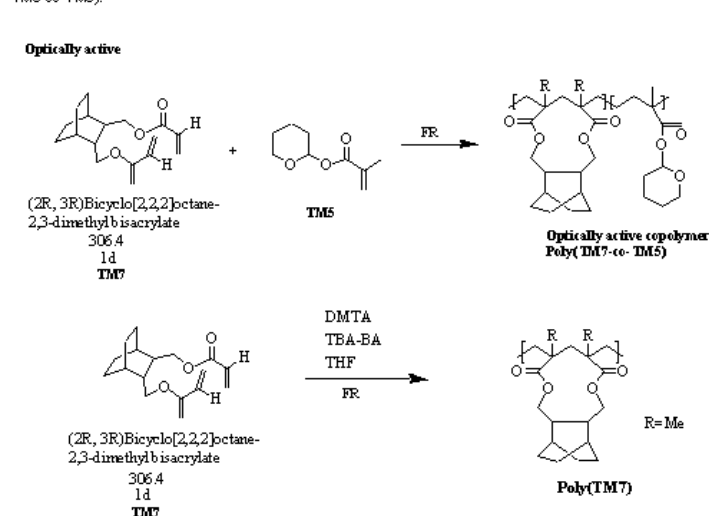
that are all aliphatic cyclopolymers are known to be very thermally stable and have UV-transparency. Our goal is to study the effect of acid content, as well as explore the effect of geometry, on dissolution rate.

Acrylate-based cycloaliphatic copolymers and homopolymers derived from (\pm) (R,R) endo,exo-bicyclo[2,2,2]-octane-2,3-dimethyl bisacrylate (TM6, TM7), and tetrahydropyranyl methacrylate (TM5) were prepared with varying acid compositions by free radical methods for use in ArF lithography.

Scheme 1- Synthesis of Monomers (Procedure repeated with Bis[(S)-1-ethoxy-carbonyl]ethylfumarate to form the optically active monomer, and diethyl maleate to form the cis monomer).



Scheme 2- Synthesis of Polymers and Polymerization of Monomers (Procedure repeated with TM6 to form TM6-co-TM5).



Procedure:

The monomers were made according to Scheme 1. The monomers were then used to make the polymers, as described in Scheme 2 (the cis monomer was not polymerized). The transracemic and optically active copolymers were made in varying compositions (Table 1). F1 and F2 were the actual compositions, while f1 and f2 were the desired compositions of TM7/TM6 versus TM5. Each of the copolymers were then used to make resist. The actual amount of material (copolymer), PAG (triphenyl sulfonium trifluoromethane sulfonate), and solvent (1-methoxy-2-propanol-acetate) used to make the resists are shown in Table 3. The resists were then taken to CNF, where they were spin coated onto 3-inch silicon wafers for 30 seconds at 1500rpm yielding films 252-389 nm thick. The wafers were pre-baked at 90°C for 60 seconds. The wafers were exposed to 248nm radiation. The wafer was finally post-baked at 100°C for 90 seconds. The wafers were then used to measure the dissolution rate. The dissolution rates were calculated using the formula:

$$dp = \frac{\lambda(\text{nm})}{2[n_2^2 - n_1^2 \sin^2 \theta_1]^{1/2}}$$

with $\lambda = 632.8\text{nm}$, $\theta_1 = 10^\circ$, $n_1 = 1.333$, $n_2 = 1.54$.

Results and Conclusions:

The dissolution rate was measured for all of the copolymers. Only the copolymers with a molecular weight less than 7000 g/mol gave a measurable value (Table 4). The measured dissolution rates were lower than current values. By using a different method of polymerization, GTP versus FR, we would have been able to control the molecular weight of our copolymers. This would have allowed the dissolution rates of all of the copolymers to be measured.

References:

- 1) Rodriguez, F.; Krasicky, P.D.; Groele, R.J. "Dissolution Rate Measurements". Solid State Technology 1985, May, 125-131.
- 2) Itani, Toshiro; Yoshino, Hiroshi; Hashimoto, Shuichi; Yamana, Mitsuharu; Miyasaka, Mami; Tanabe, Hiroyoshi. "Dissolution characteristics of chemically amplified 193 nm resists". American Vacuum Society, Nov./Dec. 1998, 3726-3729.
- 3) Krasicky, P.; Groele, R.; Rodriguez, F; "A Laser Interferometer for Monitoring Thin Film Processes Application to Polymer Dissolution". Chem. Eng. Comm. 1987, Vol. 54, 279-99.

Acknowledgements:

None of the work completed would have been possible without the help of the following institutions/people: NNUN, CNF, Melanie-Claire Mallison, Dr. Dotsevi Sogah, Armah Kpissay, and Cornell University.

| Polymer | Method | f1 | F1 | f2 | F2 | % yield | Mn |
|------------|--------|-----|------|-----|------|---------|-------|
| TM7-co-TM5 | FR | 0.5 | 0.55 | 0.5 | 0.45 | 78 | 6592 |
| TM7-co-TM5 | FR | 0.6 | 0.59 | 0.4 | 0.41 | 100 | 17040 |
| TM7-co-TM5 | FR | 0.7 | 0.88 | 0.3 | 0.22 | 89 | 6328 |
| TM7-co-TM5 | FR | 0.8 | 0.82 | 0.2 | 0.18 | 94 | 11820 |
| TM6-co-TM5 | FR | 0.5 | 0.51 | 0.5 | 0.49 | 91 | 15860 |
| TM6-co-TM5 | FR | 0.6 | 0.67 | 0.4 | 0.33 | 97 | 15370 |
| TM6-co-TM5 | FR | 0.7 | 0.77 | 0.3 | 0.23 | 100 | 15650 |
| TM6-co-TM5 | FR | 0.8 | 0.81 | 0.2 | 0.19 | 97 | 20590 |

Table 1

| Copolymer | Material (g) | F1 | PAG (g) | Solvent (ml) |
|------------|--------------|------|---------|--------------|
| TM6-co-TM5 | 1.5 | 0.55 | 0.075 | 14 |
| TM6-co-TM5 | 1.5 | 0.59 | 0.075 | 14 |
| TM6-co-TM5 | 1 | 0.88 | 0.05 | 10 |
| TM6-co-TM5 | 1 | 0.82 | 0.05 | 10 |
| TM7-co-TM5 | 1 | 0.51 | 0.05 | 10 |
| TM7-co-TM5 | 1 | 0.67 | 0.05 | 10 |
| TM7-co-TM5 | 1 | 0.77 | 0.05 | 10 |
| TM7-co-TM5 | 1 | 0.81 | 0.05 | 10 |

Table 2

| Polymer | Composition | Mn | Dissolution Rate (nm/s) |
|------------------|-------------|------|-------------------------|
| Poly(TM6-co-TM7) | F1= 0.88 | 6328 | 44.2 |
| Poly(TM6-co-TM7) | F1= 0.55 | 6592 | 40.6 |

Table 3

Development of Plasma Etching Processes for the Fabrication of Porous Vertical Structures

REU Intern: Flora Felsovalyi, Agricultural and Biological Engineering, Cornell University

Principal Investigator: Hercules Neves, Electrical Engineering, Cornell University, Herc@ee.cornell.edu

Mentor: Ricky Soong, Bioengineering, Cornell University

Abstract:

The main objective of this project is to implement plasma etching techniques to fabricate porous vertical structures in a silicon substrate. These structures will serve as synthetic membranes for integration with biological molecules.

Several processing steps were performed prior to silicon etching. Various different types of membranes were designed: both straight and jagged-edged sides were made, and the width of these structures was varied between 10 and 0.6 μm . Photolithography was used to define these features on the resist layer of oxidized membranes.

Next, the Plasma Therm SLR-770 was used extensively to provide the silicon etching. In order to obtain the desired structure, several etching parameters were varied: polymer deposition time, plasma etch rates, and RF power. The resulting structures were analyzed using the scanning electron microscope, and the etching was repeated using different parameters to obtain better results. Imaging showed that ridges were formed on the sides of the structure due to slightly isotropic plasma etching. Initial results showed that on the jagged-edged structures, pores appeared in a grid-like manner and that this structure may be compatible with biological materials.

Introduction:

In order to create this vertical structure, we rely on the etching properties of the Plasma Therm 770 Bosch Etcher. By manipulating several etching parameters, the machine will etch in a ridge-like manner, due to slight anisotropic etching. Therefore, on a straight vertical wall, it will create long parallel ridges. If the machine etches on both sides of a membrane simultaneously, and if we minimize the distance between the walls, then long slits will form because the etching on both sides will meet. This will result in a one dimensional membrane because the slits are only formed in the vertical direction. In order to create a two dimensional grid-like membrane, we created jagged edges on the membrane, making some parts thinner, where the silicon would be etched all the way through, and thicker parts, where the etching would not go through. This way, we tried to create a vertical membrane with systematic, grid-like pores.

Procedure:

Before photolithography was implemented to transfer the membrane patterns onto the wafers, the silicon wafers were oxidized. This layer of silicon oxide acts as a mask to protect the top of the membranes from being etched away. Next, the 10x i-line stepper was used to transfer the membrane patterns onto the silicon wafers. The membrane design was created in a CAD program, and

then transferred to a mask. Each mask contains forty membranes, with three different parameters which are varied. Half the membranes have straight edges, used as a control, and the other half are jagged-edged. Two different membrane lengths are also used (one is twice as long as the other) in order to test the effects of stress and strain on the membrane. Finally, the most important parameter which is varied is the thickness of the membrane. It ranges from 10 μm to 1 μm in increments of two μm and from 0.9 to 0.6 in increments of 0.1 μm .

The first step in etching was to etch away the layer of silicon oxide where no membranes are present. Next, the Plasma Therm 770 was used for the main etching. This machine etches mainly anisotropically, however, creating appropriate combinations of the five parameters can result in slightly isotropic etching. The ICP RP

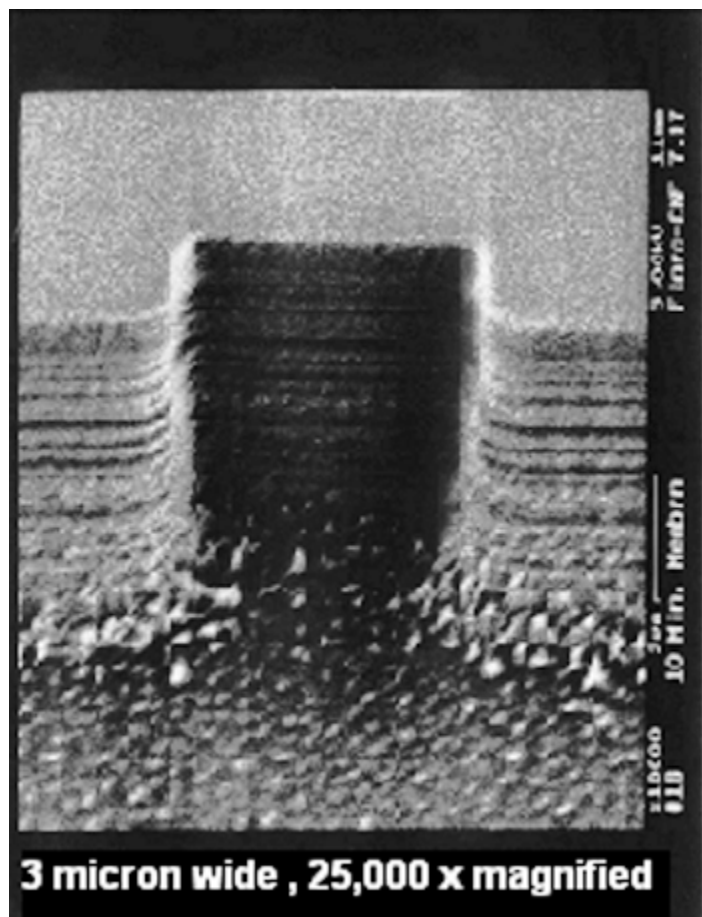


Figure 1

Power determines how many ionized species will be shot at the silicon, thus the higher this power, the more etching that will result. The REI RF Power directs these ionized species straight down perpendicular to the wafer to create an anisotropic etch. Therefore decreasing this power will create a more isotropic etch. The third parameter is deposition time; a polymer layer is deposited on the sides of the wall to protect it from isotropic etching. It is favorable to our experiment to decrease this time. And finally there are two etching steps, Etch A and Etch B. A etches the plasma while B etches the silicon.

Once a grid-like pattern of holes is created, the next step will be to control the size of these pores. This can be done by oxidizing the silicon, and then using hydrofluoric acid to etch the silicon oxide isotropically. The etch time will depend on the size we want our pores to be. Finally, upon completion of this step, we will integrate our membrane with biological molecules to give our membrane specific characteristics.

Results and Conclusion:

We observed that ridge-like structures do in fact form on the sides of straight-edged membranes. (See Figure 1) This means that the Plasma Therm does in fact etch both isotropically and anisotropically. We also observed the beginnings of pore-like structure formation. (See Figure 2) However, these pores were not present evenly throughout the entire membrane.

The next step in this project will be to find the appropriate parameters of etching in order to create a systematic grid of pores. Then, once the correct pore size is achieved, this membrane can be integrated with biological molecules. Our results show us that plasma etching technique can be used to create a vertical membrane.

Acknowledgments:

I would like to thank Herc Neves and Ricky Soong for all the help they provided. I would also like to thank the National Science Foundation, the CNF Staff, and Melanie-Claire Mallison for supporting this program.

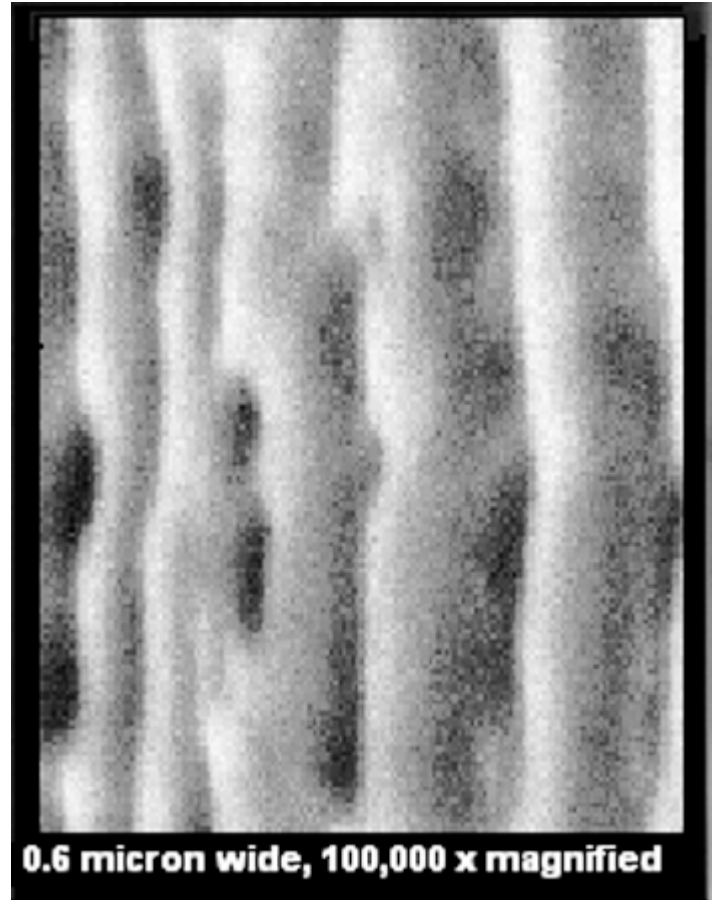


Figure 2

Fabrication of a Microscale SPR Device

REU Intern: Jeremy Hoff, Electrical and Biomedical Engineering, Duke University

Principal Investigator: Carl Batt, Food Science, Cornell University, cab10@cornell.edu

Mentor: Christine Campagnolo, Cornell University, cc179@cornell.edu

Abstract:

The focus of this project was to fabricate a microscale flowcell for an SPR biosensing device. Our objectives were to (1) minimize the flow cell volume, thereby reducing the amount of reagents required per experiment, (2) to optimize the topology of the flow cell, so as to encourage mixing between surface immobilized reagents and those passing through the flow cell, and (3) to act as a prototype for a multi-sample parallel SPR device.

The surface plasmon resonance (SPR) effect allows us to measure small changes in refractive index (RI) at a surface. Measurement of the SPR minimum reflectance angle over time provides a highly sensitive optical biosensing technique for detection of biomolecular interactions at a thin metal surface.

In this paper, the fabrication of microscale flow cell device is reported. Due to issues involving a fault in the bonding of the flow cell and the alignment of the instrument's optics with which the flow cell was to be tested, the performance of the microfabricated devices remains unexplored. Future work will continue with the devices once the bonding has been reinforced and the optics realigned.

Introduction:

Surface Plasmon Resonance (SPR) is an optical phenomenon which can be used for the detection of macromolecular interactions at a sensor surface. In SPR detection, light is coupled into a waveguide. The light is totally internally reflected at the surface of the waveguide, which elicits an evanescent wave normal to the surface of the waveguide. At the appropriate incident angle (the SPR minimum), the wavevector of the evanescent wave couples with the electromagnetic surface wave of a thin film of gold (50nm) placed on the waveguide surface. This results in an excitation of the electrons in the gold film, observable as a minimum of the reflected light in the waveguide at this incident angle. The SPR minimum is highly sensitive to changes in the refractive index of the gold sensor surface.

As macromolecules interact with the gold surface, the refractive index of the gold changes. By tracking the resulting SPR minima changes, we can characterize the binding interactions of molecules bound upon the gold sensor surface and solution passed over that surface (Figure 1).

Figure 1, above right: SPR minimum change as a result of protein-protein interactions. Here streptavidin is immobilized on the sensor surface via a DTSSP cross-linker and anti-streptavidin is subsequently introduced, resulting in an increase in the SPR minimum as the antibody binds to the immobilized target.

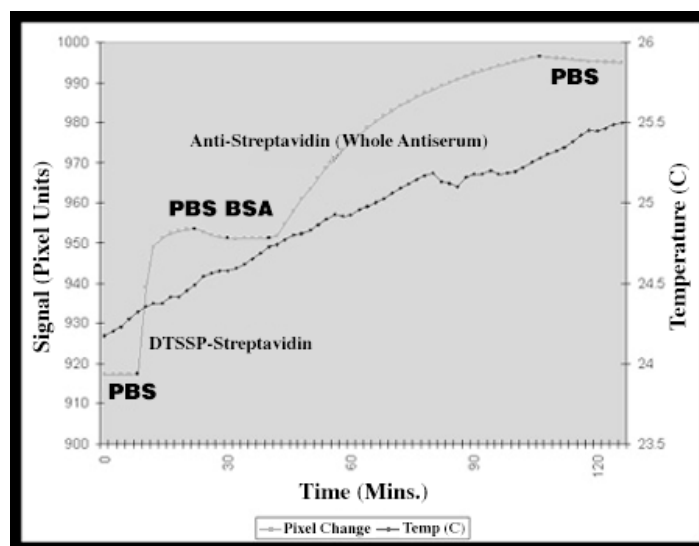


Figure 1

This method of detecting macromolecular binding provides several advantages. We are able to qualitatively and quantitatively characterize reversible binding interactions among biological macromolecules via observation of a physical quantity (refractive index). Thus there is no need for reagent labeling. Further, data is collected and analyzed in real-time. Also, because we are concerned only with refractive index changes at the gold surface itself (i.e. the reflectivity of the surface), very small reagent volumes can be used.

Miniaturization of the flow cell improves the biosensing ability of the SPR instrument. By decreasing the dimensions of the flow cell, the efficiency with which the mobile binding partner interacts with the immobilized target is increased. Less reagent is necessary for detection, and detection time is reduced, leading to faster real-time data acquisition. Parallel SPR detection is also possible with incorporation of multiple flow cells onto a single chip/wafer.

Experimental Procedure:

A number of 3" diameter, 1mm thick 7740 pyrex glass wafers were obtained and cleaned with Nanostrip. Approximately 70nm Cr was thermally evaporated on both sides of the wafers. Approximately 18 μm of Shipley 1820 photoresist was spun on each side and one side patterned in a 5x stepper with the flow cell mask. The wafers were developed in 300MIF and etched with buffered oxide etch (1:6 HF:ammonium flouride) for 100 hours. The remaining photoresist and chrome was stripped from the wafer. A 15Å chrome adhesion layer and 50nm gold were thermally evaporated on the face of the flow cell wafer.

Approximately 12 μm of 1813 photoresist was spun on the wafer face and patterned in a 5x stepper with the sensor mask. The resist pattern was developed and the wafer etched in Au etchant. The remaining photoresist was stripped.

Inlet and outlet holes were drilled approximately 3" apart in a polystyrene culture slide, which was then epoxied to the face of the flowcell. Micropipet tips were epoxied to the inlet and outlet holes.

Results and Conclusions:

An SPR scan of the microscale flow cell initiated in air and PBS buffer solution revealed unexpected results (Figure 2). The unexpected results are likely due to the SPR instrument not reading properly. Possible contamination of the gold surface during fabrication has been ruled out by the controls performed with two instruments using blank gold slides. The data demonstrated that the instrument externally configured for the microfabricated flow cell did not demonstrate the minimum reflectance dip characteristic to SPR, whereas another instrument with the same optics set up was able to detect the reflectance minimum. This data suggested the configuration of the internal optics for the instrument externally configured for the microfabricated device needed to be evaluated. In addition, poor sealing by the epoxy, leading to leakage from the flow cell was also an issue. This issue can be addressed by reinforcing the sealant.

Figure 2: Comparison of SPR scans from unmodified and the externally modified instruments. Instrument 2 has been externally configured for the microfabricated flow cell. (A) SPR scans from Instrument 1, showing expected SPR curve. (B) Scan from Instrument 2 with macroscale flow cell. Note that the scan already deviates from the expected curve. (C) Scan from Instrument 2 with microscale flow cell. The results differ greatly from the expected curve.

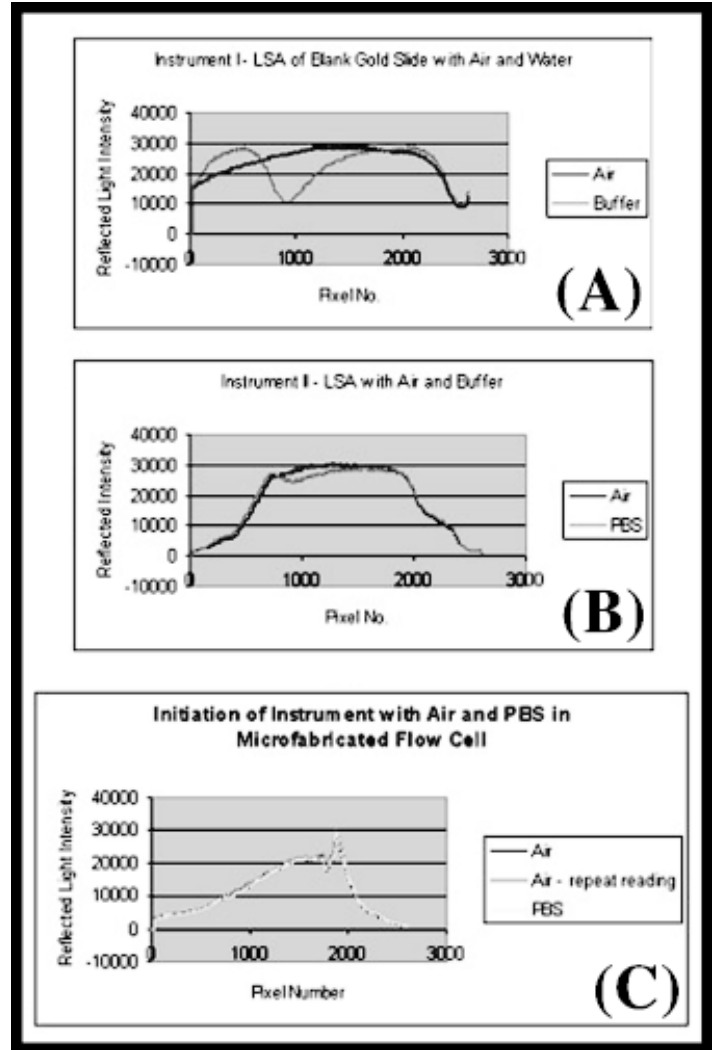


Figure 2

Controlling Cell Motility Using Microfabrication Technology

REU Intern: Jonathan Hong, Bioengineering and Systems Engineering, University of Pennsylvania

Principal Investigator: W. Mark Saltzman, Chemical Engr, Cornell Univ, saltzman@cheme.cornell.edu

Mentor: Jian Tan, Chemical Engineering, Cornell University

Abstract:

In this study, nanofabrication techniques were used to create various topologies to create a suitable product for tissue engineering research. Nanofabrication techniques were utilized to determine optimal exposure times at a constant focus 251 (silicon) and 281 (glass) for different arrays of concentric rings and bars. In both cases, the non-uniformity across the entire pattern necessitated the use of range of exposure times to attain optimum clarity. Finer patterns achieved optimum clarity at lower exposure times, but at the expense of the clarity of patterns of larger separation. Optimal exposure times for the patterns and designs ranged from 0.24-0.88 secs. on silicon (with oxide mask) wafers. Optimal exposure times for the same patterns and designs on glass ranged from 0.38 to 2.00+ secs. Higher exposure times were necessary when a stronger resist was applied. Etched silicon wafers will be utilized in future research as a mold to produce hydrogels with inverse images. On the glass surface, chemical patterns will be produced. Cells will be applied to the patterned surfaces of both images in future cell motility studies.

Introduction:

The evolving field of bioengineering has demonstrated a greater need for current technology to be capable of serving a greater number of purposes in biological processes. The maximization of a current technology's potential is attainable through variations in the characteristics of the materials critical in biological processes, especially the shape and composition of the material. While most researchers have focused on varying chemical patterns, only a few studies have used physical patterns to manipulate cell behaviors [1]. Surface topography, a key component in determining a material's shape is especially crucial to cell motility. While some cells such as macrophages [2] may be more mobile on a rough surface, different types of cells such as fibroblasts [2] will prefer smooth surfaces. Likewise, variations of the same pattern (i.e. spacing) can have different effects on a cell's motility. The primary objective was to design different arrays of patterns on different substrates using photolithographic techniques for use in further cell motility studies. To maximize cell motility study capabilities, it was necessary to determine the optimum conditions that produced the most favorable pattern so it could be mass-produced.

Procedure:

Standard photolithography techniques were utilized at the CNF (Cornell Nanofabrication Facility) to construct the necessary patterns and arrays. First, the patterns and arrays, concentric circles and bars ranging in feature separation from 2 μm - 18 μm by increments of 2 μm , were designed on CAD. Following the pattern design, the design files were transferred to a PG 3600 optical pattern

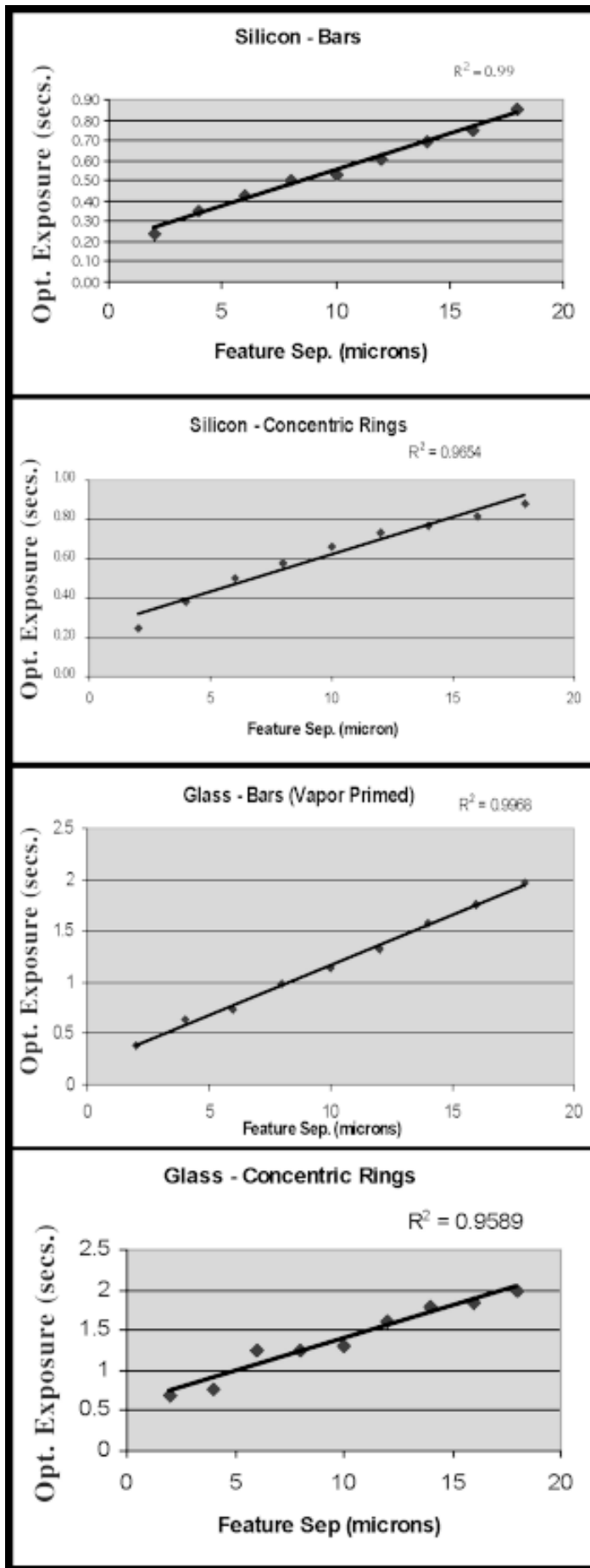
generator which exposed the CAD pattern onto the chrome mask. After mask processing, via development, chrome wet etching and resist strip, the mask was ready for use in conjunction with the 5:1 g-line stepper and substrates.

Before the exposition of substrate could occur, it was necessary to prepare the substrates. For silicon, a 2000 \AA oxide etch mask was planted on the wafer surface to protect the mask during the silicon etch process. To ensure adhesion of the pattern on glass, a meticulous cleaning process was conducted. After the 25 x 25 glass squares were cut from 25 x 75 x 1 mm slides, they were initially cleaned in Nanostrip and placed in a PlasmaTherm 72 to burn the oxide off the glass. Following the oxide burn, the glass was vapor-primed in a Yield Engineering System Oven using HMDS. Shipley 1813 and 1827 photoresists were spun onto the silicon wafers and glass squares respectively at 5500 rpm for 30 secs. to obtain desired thickness of 1.2 μm with the 1813 on silicon and 2.0 μm thickness with the 1827 on glass. The silicon samples were baked on a hot plate at 90°C for 60 secs. Glass samples were baked on a hot plate at 115°C for 90 secs. Using a GCA 6300 5:1 g-line stepper, the patterns were exposed onto the different substrates with a focus of 251 for silicon and 281 for silicon at time periods from as low as 0.15 secs. to 2.00 secs.

Immediately following exposure, the samples were baked on a hotplate for 60 seconds at 115°C for glass and 90°C for silicon. Following the post-bake exposure, samples were developed for one minute in 300 MIF, with the exposed area washed away and rinsed in DI water. Samples were nitrogen blow-dried and stored for etching (silicon only) by Plasmatherm 72 Reactive Ion Etcher and PlasmaTherm 720 Reactive Ion Etcher. The PlasmaTherm 72, etching oxide at a rate of 328 \AA of oxide per minute, was set to etch the 2000 \AA oxide layer in 6.15 minutes. The PlasmaTherm 720, etching silicon at approx. 0.1 μm per minute, was set to etch the silicon for 20 minutes to create the desired 2 μm deep etch in preparation for future cell motility studies.

Results and Conclusions:

It was found that the optimal exposure varied from sample to sample due primarily to varying environmental and sample conditions. Consequently, the process for determining optimum exposure for each array of each pattern was performed a minimum of two times on different pieces of the same type of substrate. The mean of the "extremes" or the mean of the dosages that first showed signs of underexposure and overexposure of the particular array was used to represent the optimum dosage for that particular array. Also, with the non-uniform appearance of the pattern, optimum clarity of one array would be attained at the expense of other arrays, clarity causing over or underexposure of certain arrays depending



on the dosage. Consequently, a range of exposures was necessary to represent the optimum clarity of all nine of the arrays, rather than just one dosage. The optimum exposure times were plotted as a function of feature separation for glass and silicon in which the exposed patterns were rings and bars. The four graphs are shown opposite (fig. 1).

Linear regression analysis was performed on all four graphs and the R-squared values were relatively close to one, indicative of a linear trend between optimum exposure time and feature separation. As expected, the stronger photoresist used on glass (1827) had a range of optimum exposures significantly higher than that of the 1813 photoresist used on the silicon.

In comparing the two patterns on individual substrates, it was found that the range of optimum exposures for concentric rings was slightly higher than its counterpart. The general behavior for the concentric rings to have a higher requirement of exposure time for the same feature separations can be attributed to the content of the patterns. The pattern of concentric rings is significantly more complex than the bar pattern, demonstrating a need for a higher optimum dosage at the respective feature separations. It was also apparent that the range of arrays with acceptable clarity expanded with the increase in feature separation. Thus, at a 2- μm feature separation, arrays of acceptable clarity existed for a range of less than 0.04 secs., whereas the range of acceptable arrays for the 18- μm existed over a time period of 0.4 secs, almost 10x of the 2- μm array.

A special case in which a range of exposures was not necessary to capture the optimum exposures for all the arrays occurred with the glass substrate. During the exposition process, the 5:1 g-line stepper outputted "wafer too thick" but following development, the die for which the error statement was displayed showed all nine arrays with optimum clarity, all considerably better in clarity than several of the optimum dies that had been exposed under normal processes. In future studies, it would seem feasible to intentionally create a "wafer too thick" situation on glass to obtain a pattern of maximum clarity thus saving time by negating the need to use multiple dosages to obtain multiple dies each with its own optimum arrays.

Following the etching of the optimum patterns on the silicon, the substrate will be used as a mold to create a hydrogel surface for future cell motility studies. For the glass, there will be no etching but rather, a mineralization process will be conducted on its surface using the patterned photoresist as an outline.

Acknowledgments:

The author would like to thank W. Mark Saltzman for the opportunity to conduct cell motility research, Jian Tan for providing guidance and advice in this research project, and CNF and Staff for providing the training and assistance with CNF lab tools. The author would also like to thank NNUN and NSF for providing the funds and opportunity for this research experience.

References:

1. Tan, J, Shen, H, Carter, KL, Saltzman, WM; Controlling human polymorphonuclear leukocytes motility using microfabrication technology. *J Biomed Mater Res* 2000, 51: 694-702.
2. Rich AM, Harris AK; Anomalous preferences of cultured macrophages for hydrophobic and roughened substrata. *J Cell Sci* 1981, 50:1-7.

Studies of Silicon Surface Migration in the Formation of Sub-Surface Voids

REU Intern: Wendi Maeda, Electrical Engineering, University of Hawaii at Manoa

**Principal Investigator: Michael Skvarla, Cornell Nanofabrication Facility, Cornell University,
skvarla@cnf.cornell.edu**

Abstract:

The focus of this project is to characterize void formations as a function of pore size, etch depth, and repeat spacing. Photolithographic techniques are primarily used, with an e-beam used for comparison. Using a two-level aligned exposure, pores are created in the first level while etching and analysis is performed with the second. After the completion of the first level, the wafers are annealed. At high temperatures, atoms migrate and tend to minimize the surface energy, creating sub-surface voids. Organizing matrices of pores lead to the formation of extended sub-surface structures, which have applications in many areas, including fluid transport systems, sensor actuators, and MEMS devices. Advantages of this technique include a more robust structure, as well as the capability of mass production, due to the use of photolithography.

Introduction:

The proposed technique for the formation of sub-surface voids was derived from research done at the Toshiba Corporation, Microelectronics Engineering Laboratory [1]. Investigations were performed on the formation of Empty Spaces in Silicon (ESS) due to the phenomenon of high temperature surface migration. During high temperature surface migration, atoms on the surface of a silicon wafer migrate so as to minimize the surface energy. According to observation, ESS were created once deep etches were placed in a high temperature hydrogen ambient. By aligning rows or matrices of pores, sub-surface channels and areas can be created if

$$D < 3.76 \times R$$

where D = the distance between pores and R = the radius of the pores.

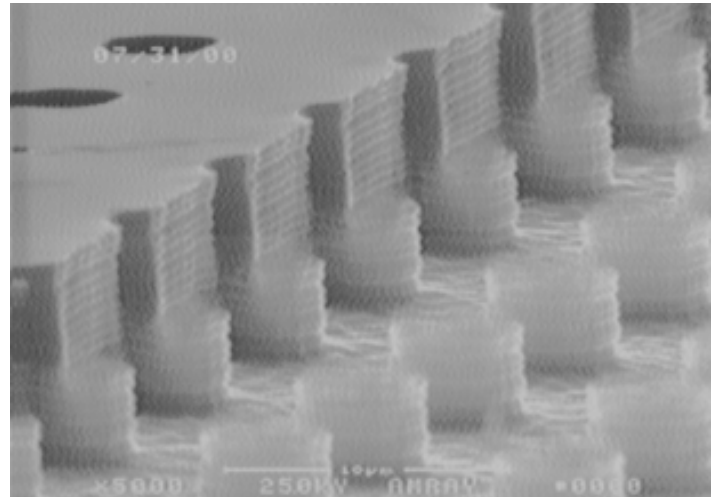
The purposes of this project were to: 1) develop a repeatable fabrication process for this technology, and 2) characterize void formations as a function of pore size, etch depth, and spacing of pores. It would be advantageous to develop a photolithographic fabrication process since it will lead to the mass production of devices using this sub-surface void technology.

A design of pores with various sizes, ranging from 0.2 - 2 μm , and spacing was created using CAD. Since the fabrication process required the use of a two-level aligned exposure, two masks were fabricated using an optical pattern generator. The first mask was used to create the pores, while the second mask was used for the analysis portion of the experiment. Next, the silicon wafers were spun with 620-7i photoresist to create a 0.6 μm layer and pre-baked at 90°C for 60 sec. The last step of the photolithographic process

was to perform an exposure of the pores using a 10x i-line stepper and to post-bake the wafers for 60 sec. at 115°C. Electron beam lithography was used to create smaller features (0.2 and 0.4 μm).

Once the wafers were exposed, they were deep etched using the PlasmaTherm 770 ICP Bosch Etcher. Smaller features were etched at a rate of 1.3 $\mu\text{m}/\text{min}$., while larger features were etched at a rate of 2.0 $\mu\text{m}/\text{min}$. Next, most of the photoresist was stripped using a reactive ion etcher, while the remaining resist was stripped using acetone and isopropyl alcohol.

The wafers were then cleaned in base and acid baths and annealed in a hydrogen ambient for 4 hours at 1100°C. After annealing, the wafers were exposed and etched for analysis. The second level etch was performed such that the original pore trenches were sliced in half and revealed. A scanning electron microscope was used to examine the trenches in detail.



Results and Conclusions:

Upon analysis, annealed etched trenches began showing signs of sub-surface void formation. Trenches on annealed wafers ballooned out at the top, then tapered at the bottom. In comparison, trenches on wafers that were not annealed were etched straight down, without any change in trench shape. The size of the pore in the picture above was 0.8 μm , with an etch depth of approximately 6 μm .

Polymers deposited on the side walls during etching of the pores remained present during the final etching and examination. These contaminants left cloudy cylindrical shapes that can be seen in the SEM picture on the opposite page. The pore size was 2.0 μm , with an etch depth of 10 μm .

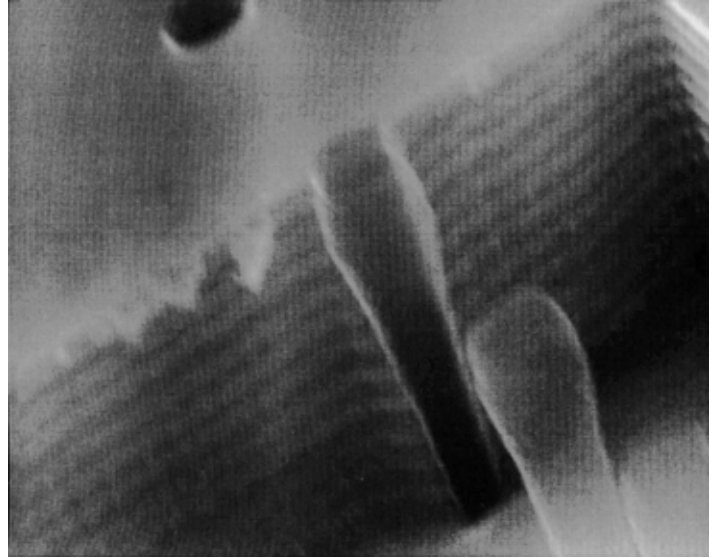
In order to obtain correlations between pore size and sub-surface void formation, more experiments need to be performed. For future work, wafers need to be annealed for longer times (> 6 hours), or smaller features need to be examined, in order to see significant sub-surface void formation. Also, experiments could be run with various shapes and etch depths.

Reference:

[1] Sato, T. et al., IEDM, p.517-520, 1999.

Acknowledgments:

First, I would like to thank the National Science Foundation for funding this project. I would also like to thank the National Nanofabrication Users Network and the Cornell Nanofabrication Facility staff for allowing me this opportunity to gain experience in nanofabrication. Finally, special thanks to my Principal Investigator, Mike Skvarla, for his guidance on the project.



Evaluation of Collagen as a Membrane Material

REU Intern: Catherine Newman, Mechanical Engineering, University of California at Berkeley

Principal Investigator: Michael Spencer, Electrical Engineering, Cornell University,
Spencer@ee.cornell.edu

Abstract:

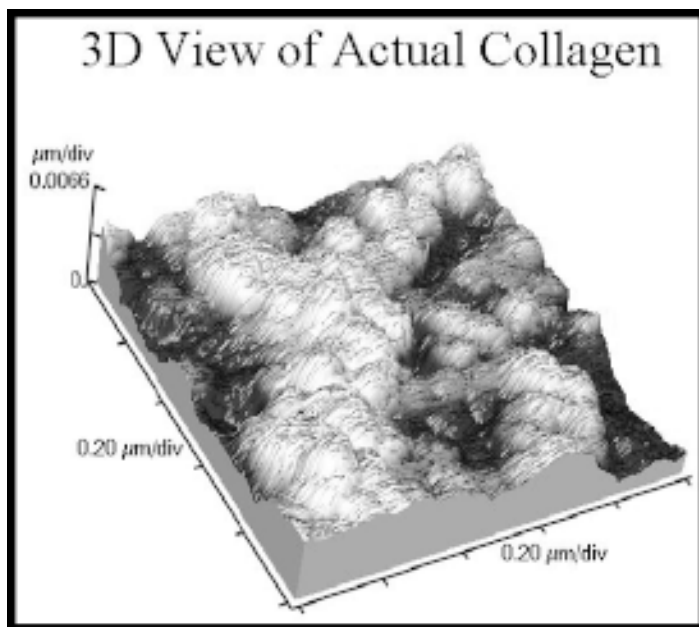
Collagen is a candidate material for micro-cell culturing and other porous patternable membrane applications. In an attempt to integrate biological materials with nanofabrication, this project's goal has been to construct a stable collagen membrane onto a silicon wafer and to develop a relationship between the membranes thickness and its pore size.

To obtain the "mounted" membrane, a viscous collagen is spun onto a silicon wafer, using various spin speeds and layers. Experiments have been performed to determine the optimum conditions for producing the collagen membrane. The collagen is characterized by Atomic Force Microscope (AFM) and other techniques before and after cross-linking in order to establish the relationship between the pores' diameter and membrane's thickness.

Introduction:

Collagen is a well-known protein found in all multi-cellular animals. Type I collagen, characterized by its triple helical structure and derived from calf's skin, was used in this study of collagen as a membrane material.

Collagen can be used to create a porous membrane when first a single strand of collagen binds with others to form long fibers. These fibers then bind side by side to form fibrils. These fibrils are analogous to today's fiber optic cables, however their size can range anywhere from .5 to 3 μm .



The initial goals of the project were to first study the mesh like structure formed when aqueous collagen fibrils are spun onto a silicon wafer, and second to develop a relationship between the membrane's thickness and its pore diameter.

Experimental Procedure:

Using an aqueous collagen, the solution is spun onto a 3 inch wafer. Twenty drops of collagen, at a concentration of 6 mg/ml, is applied to the wafer and then spun at 2500 rpm for twenty seconds. The wafer is then baked at 200 degrees farenhight for 30 seconds.

To obtain a thicker "membrane" on the surface of the wafer, these two steps are the repeated. Spin-bake-spin-bake-etc. This was done until five wafers were coated with layers ranging from 1 to 5 μm . Once the collagen is on the surface, it must be cross-linked. This must be done because the Fibrils of type I collagen do not self-adhere to each other. By cross-linking with a 1% Gluderaldehyde solution, the individual stands bond and a single membrane is created.

Results:

The five 3 inch wafers were examined using AFM and Alfa Stepper. Sample One had a layer approximately 1.5 μm thick, but the membrane was so thin that there were large areas with no well defined pores. Sample Two (40 drops) had a thickness of approximately 3 μm and had more smaller undefined regions than the first sample. In sample Three (60 drops), the surface began to form a uniform membrane with well-defined pores. The pores in sample Three ranged from 5/10 to 2/10 μm . Sample Four (80 drops) had the most promising results. The membrane's surface was very uniform and its pores were the most defined of the five samples. The pore diameter of the this sample was, on average, 2/10 μm . Sample Five, with an indeterminable thickness, appeared to be very smooth, however, the collagen appeared to "fill in" the existing pores. Furthermore, it was unclear if the remaining pores ran all the way through the membrane.

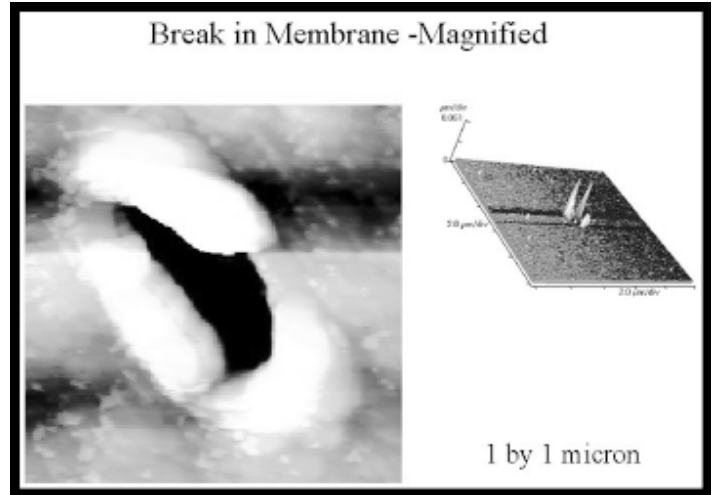
Conclusions:

With only five useable samples, a well-defined relationship between the pore size and thickness could not be determined. In the future, steps might be taken to prevent gaseous pockets, formed during baking, from creating tears in the membrane.

Also, further research could improve the membrane's uniformity over the entire surface of the wafer.

Acknowledgments:

Special Thanks To: Professor Michael Spencer, Cornell University, Tony Price, Hemant Bengale, Greg Baxter, James Griffin, Marsha — for her daily smiles, Ms. Molly Burton and Miss. Virginia Stark — for the camping lesson, and all of the CNF REUs — for a wonderful summer.



Nanofabrication and Optimization of Organic Thin Film Transistors

REU Intern: Jason Slinker, Physics, Chemistry, and Math, Southern Nazarene University

Principal Investigator: George Malliaras, MatSci and Engr, Cornell Univ., george@ccmr.cornell.edu

Mentor: Maggie Xia, Materials Science and Engineering, Cornell University

Abstract:

Organic thin film transistors (OTFTs) have great potential in electronic applications, as their compatibility with glass and plastic substrates offers benefits over silicon devices in weight, ruggedness, and cost. We report the nanofabrication and analysis of OTFTs with pentacene as the semiconductive layer. Lithography, through image reversal and metal lift-off processes, yielded devices with uniform channel lengths. In characterizing the transistors, we tested devices with 5, 10, and 20 μm channel lengths. Subsequently, we attempted to improve mobility values by inducing alignment of the pentacene through the inclusion of a polyvinyl alcohol layer.

Introduction:

Steadily approaching the performance of amorphous silicon transistors, transistors that use organic semiconductors as the active layer are presently of great interest. Such organic devices have many benefits over their silicon counterparts, including lower cost, greater durability, and compatibility with glass and plastic substrates. Additionally, a transition to such substrates might allow for implementation of continuous web manufacturing techniques, significantly lowering the cost of transistor assembly.

Organic thin film transistors (OTFTs) have great promise in electronic applications. For example, they might find use as low-density storage devices, such as for smart cards or I.D. tags. Perhaps the most enticing application for OTFTs is displays. Given their compatibility with polymeric substrates, OTFTs may enable the production of flexible computer screens.

Pentacene, an organic molecule consisting of five fused aromatic rings, has proved to be of great interest in TFTs. Though early attempts to employ organic active layers produced organic semiconductors with impractical field-effect mobilities (a measure of device speed), pentacene TFTs have recently been shown to have mobilities larger than $1 \text{ cm}^2/\text{V}\cdot\text{s}$, rivaling those of amorphous silicon TFTs [1].

Our research group is primarily interested in the physics of OTFTs. Therefore, the primary goal of this project was to create a functional device with pentacene as the active layer. We investigated the consistency of the devices by varying the channel length (the spacing between the source and drain electrodes). Finally, we looked into ways to improve device performance by including an alignment layer.

Procedure:

Heavily-doped, 3 inch silicon wafers were used as the substrates, with four 1 x 1 inch devices patterned on each substrate. A 4000 \AA

thermal oxide layer was thermally grown on the silicon surface, serving as the insulating layer. A two-layer fabrication process was utilized. For the first layer, gate electrode contacts and device frames were patterned and etched through the oxide layer and 4000 \AA into the silicon surface. The second layer incorporated an image reversal process with subsequent lift-off by which the source, gate, and drain electrodes were deposited.

Both images were patterned with Shipley S1813 photoresist and exposed through chrome masks by soft contact on Hybrid Technology Group's system 3HR contact/proximity mask aligner. The first layer image was plasma etched through the oxide layer and into the silicon layer approximately 4000 \AA via a Plasma Therm 72 Reactive Ion Etcher. Oxide etch rates were determined by a Leitz MV-SP Spectrophotometer. Gold Electrical contacts (500 \AA) were deposited by thermal evaporation on the CHA RAP-600 Thermal Evaporator, using a 50- \AA chrome layer as an adhesion layer. The wafers were diced after scribing on a Florod MEL 40 laser system. Finally, the pentacene layer was deposited via thermal evaporation, both as-received and purified.

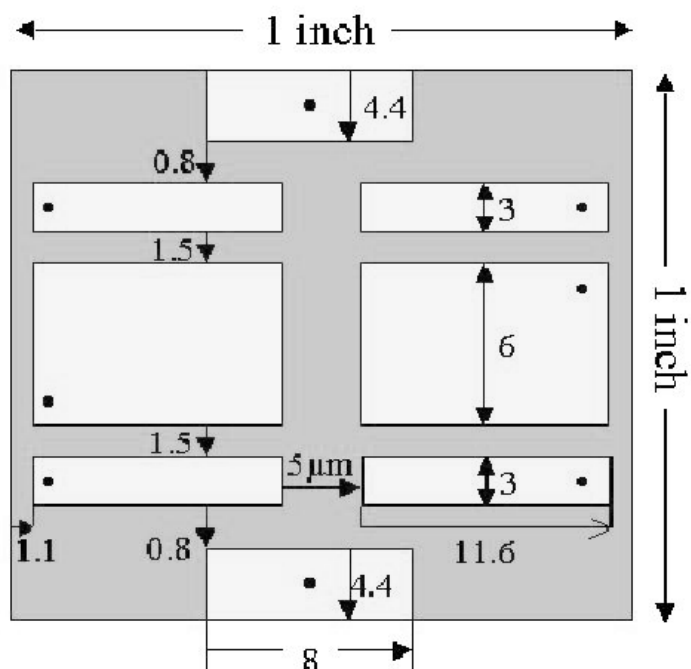


Figure 1. Top view of the OTFT before deposition of pentacene. All dimensions in mm unless otherwise noted. The two 8 x 4.4 mm rectangles represent the gate electrodes, and the other rectangles are source-drain electrode pairs in 1:2:1 ratio.

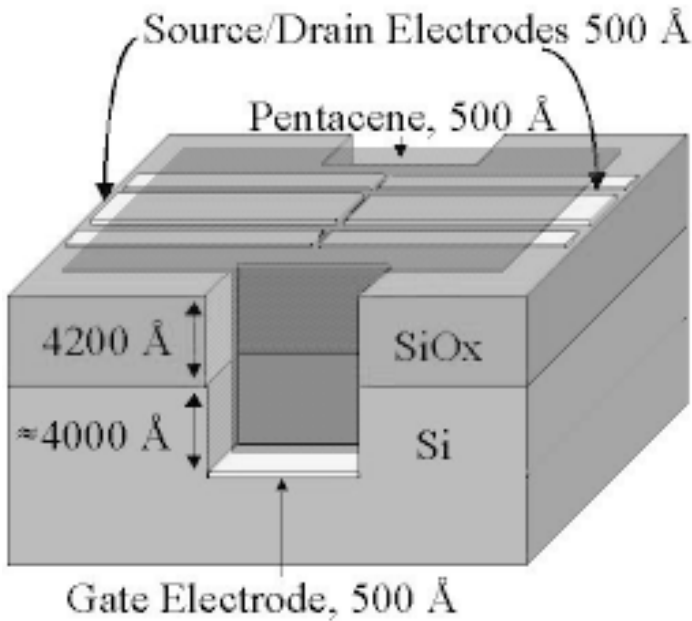


Figure 2. Side view of an OTFT with pentacene.

Additionally, we will attempt to invoke alignment of the pentacene by incorporating a layer of polymerized polyvinyl alcohol. Transistors were nanofabricated as before through the first layer, with gate electrodes being deposited before removal of the resist. These devices were sent to Navy Research Labs (NRL) for spin-coating of the polymeric layer. Rubbing this layer with a velour cloth orients charge, which in turn directs the alignment of the pentacene. Once received back from NRL, the source and drain electrodes will be deposited through a shadow mask, followed by pentacene deposition.

Results:

Channel length uniformity was confirmed via optical and scanning electron microscopy. We characterized transistors with channel lengths of 5, 10, and 20 μm with Keithley 236 Source Measurement Units, determining three fundamental parameters of the pentacene thin film transistors. Field effect mobility μ , a measure of the drift velocity of charge carriers under the unit electric field, provides a measure of the speed of the devices. Since the pentacene TFTs are adequately modeled by the standard field equations for transistors [2], we can employ the following equation from the saturation regime to extract the field effect mobility:

$$I_{d,sat} = \frac{Z\mu C_i}{2L}(V_g - V_t)^2$$

where $I_{d,sat}$ is the saturation current, Z is the channel width, μ is the field effect mobility, C_i is the capacitance of the insulating material per unit area, L is the channel length, V_g is the gate voltage, and V_t is the threshold voltage. The slope of the plot of the square root of the drain current versus gate voltage relative to the source (V_{gs}) is proportional to the square root of μ . Using as-received and purified pentacene, μ for our devices ranged from 0.024-0.047 $\text{cm}^2/\text{V}\cdot\text{s}$, an order of magnitude below amorphous silicon devices in use.

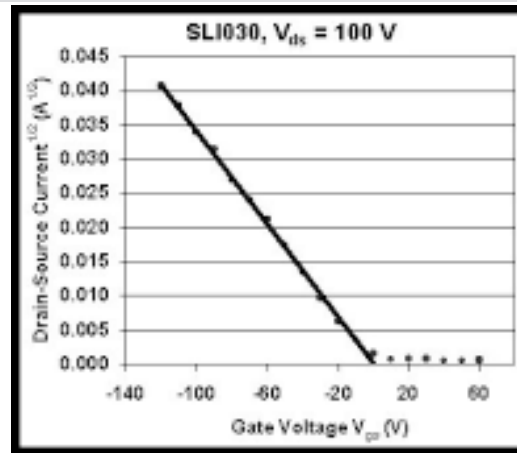


Figure 3. Plot of square root drain current vs. gate voltage. Field effect mobility is found from the slope of the linear portion of this graph.

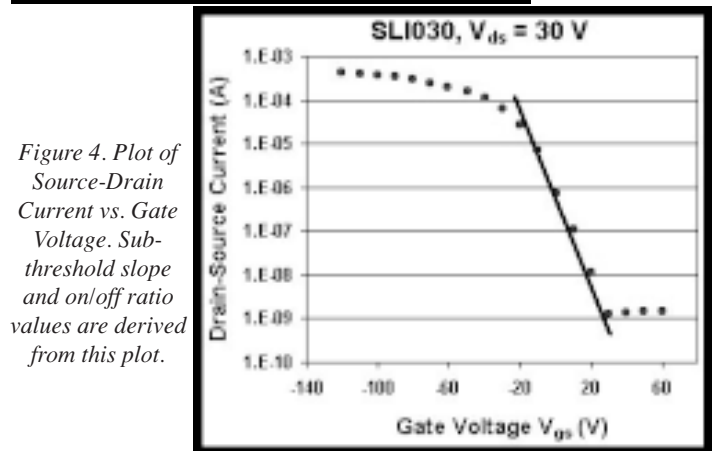


Figure 4. Plot of Source-Drain Current vs. Gate Voltage. Sub-threshold slope and on/off ratio values are derived from this plot.

Sub-threshold slope, defined as the gate voltage drop per decade change of the drain-source current, was found to be 11.5 V/decade or greater. Practical devices have subthreshold slopes an order of magnitude lower. The on/off ratio, a comparison of the drain-source current in the “on” state versus the “off” state, was approximately 10^6 .

Discussion:

Pentacene has a high tendency to form molecular crystals at room temperature. Given that it is a conjugated molecule, charge transfer is possible by “hopping” between molecular conjugation sites. Increasing the orderedness of the molecular crystals has proved to be paramount to maximizing transistor efficiency [1]. Therefore, we expect better device performance from our TFTs using the polyvinyl alcohol layer.

Acknowledgements:

I would like to thank the Cornell Nanofabrication Facility and the NNUN REU program for this opportunity. Additionally, I extend special thanks to the CNF staff and the Malliaras research group, particularly Yulong Shen, for their support of my efforts.

References:

- [1] D.J. Gundlach, H. Klauk, C.D. Sheraw, C.C. Kuo, J.R. Huang, T.N. Jackson. 1999 International Electron Devices Meeting Technical Digest, 111 (1999).
- [2] S.M. Sze. Physics of Semiconductor Devices, 2nd edition. New York, NY: Wiley Publishers (1981).

Creating a Sapphire Substrate for the Growth of Gallium Nitride

REU Intern: Sharelle Speller, Physics and Engineering, Spelman College

Principal Investigator: Jack Blakely, MatSci and Engr, Cornell University, blakely@ccmr.cornell.edu

Mentors: Kee-Chul Chang, Doohan Lee, Antonio Oliver, Cornell University

Abstract:

The growth of Gallium Nitride is the overall goal of this project. Gallium Nitride is important in that it emits blue light, a shorter wavelength (450nm). The practical use of Gallium Nitride is for lasers and light emitting diodes (LED's). The goal of this project was to create patterned sapphire(Al_2O_3) substrates that could be used to produce atomically flat surfaces of GaN. The process has recently been demonstrated at Cornell for the growth of Si on Si. It is intended that the method will also be tested for the growth of Co on sapphire.

The method of attack to pattern the sapphire substrate is by optical lithography. First, creating an optical mask with the desired features, then etching the substrate by the use of ion milling in which Argon atoms bombard the surface to create trenches. The idea is to create an atomically flat surface of a deposited film on the substrate by a 'step flow' process in which the steps move to the edges of the mesas. The square mesa features range from 1 to 20 μm in area and are surrounded by trenches about a one-micron in depth.

Introduction:

Applications of Gallium Nitride are now becoming very popular. From lasers to LED's, improvements in many devices are being made with the use of Gallium Nitride. For example, LED's are said to eventually replace traffic lights. There are energy savings of 50% to 75% and a replacement of 5-10 years as opposed to every year with the current traffic light. In comparison with non-nitride based LED's, atomic bonding in Gallium Nitride is stronger and thermal conductivity and hardness are greater. Stronger atomic

bonding means that semiconductor devices should function more reliably, at high power and frequencies even at elevated temperatures. As for Gallium Nitride based laser diodes, they now have 10,000 hours lifetime and are expected to be in the market soon.

In this project an attempt is being made to create ultra flat GaN surfaces by depositing on patterned sapphire substrate. Such surfaces are of interest in studying the mechanisms of growth of GaN and they may also have applications in making junction devices.

Procedure:

Two-inch sapphire wafers were first obtained for the experiment. The computer aided design (CAD) was then used to create the desired patterns to be converted onto the dark-field chrome based optical mask by the use of the pattern generator (PG). The desired patterns in this case were squares with edge dimension ranging from 1-20 μm , carrying a one μm spacing. The mask was then developed, etched, and stripped of the resist.

The sapphire wafer was then spun at 4000 rpm to apply a one μm thick positive resist (S1813) onto the wafer. The wafer was immediately baked at 115°C for 60 seconds, and inspected for uniform distribution of the resist. Next, the 5x Stepper exposed the patterns onto the wafer. The ideal focus and dose were 232 and 0.14 respectively, and the patterns were distributed across the wafer. Development of the wafer involved soaking the wafer in MIF 300 for 60 seconds, rinsing with deionized water, and drying with the nitrogen gun.

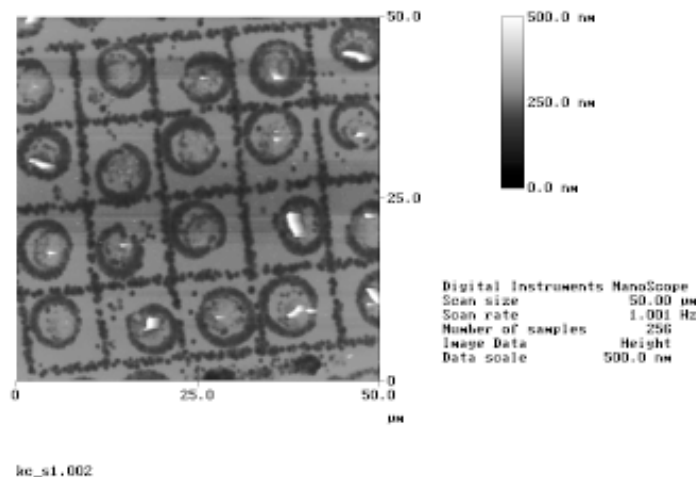


Figure 1. 10 μm squares surrounded by trenches after 40 min of Co deposition.

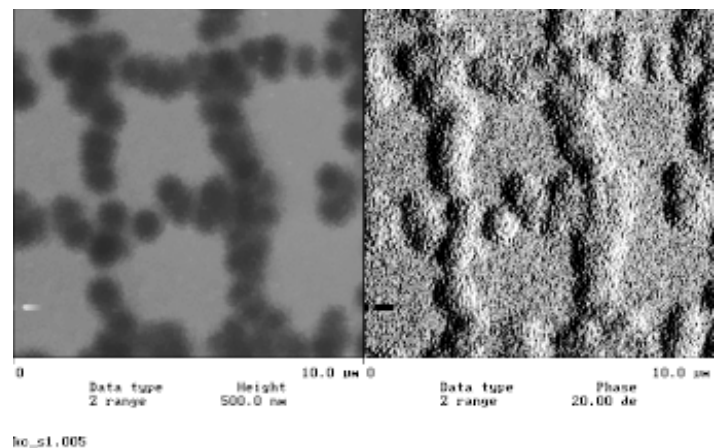


Figure 2. 3 μm squares after 90 min. of Co deposition.

In order to determine the thickness of the resist, atomic force microscopy (AFM) was used. The ion mill was then used for the etching process. To prevent the resist from burning, etching took place for one minute, cooled for another minute, and then etched again for one minute. This process was applied until 30 minutes of etching was completed. Another etching process, soaking the wafer for one hour in hydrofluoric acid, was applied to another wafer. The wafers were viewed under the AFM. Finally, the sapphire samples were taken to CHESS for the deposition of Cobalt by Molecular Beam Epitaxy (MBE).

Results and Conclusions:

During the etching process (Ion Milling and HF) the resist burned, leaving minimal features to be taken to CHESS. The features that were present for the Cobalt deposit ended up having a rough surface, contrary of the results to be expected.

In conclusion, another process would have to be developed to etch sapphire. A suggested process is to apply a coating of SiO_2 on the sapphire wafer before the resist is applied. After exposing the resist to the desired pattern and processing the resist, the SiO_2 layer would be etched with buffered HF. The remaining resist would then be removed leaving the sapphire surface with the desired patterned SiO_2 . This surface would then be ion milled to create trenches in the sapphire with the final step being the removal of the SiO_2 with HF.

Acknowledgements:

NNUN, NSF, CNF Staff, Jack Blakely, Kee-Chul Chang, Doohan Lee, Antonio Oliver, CHESS Staff.

References:

- [1] www.euro-technology.com/bluelaser/
- [2] www.itd.anl.gov/highlights/9-2/gallium.html

Damascene Tungsten and Polycrystalline Silicon in an Oxide Matrix

REU Intern: Virginia Starke, Physics & Math, New Mexico Institute of Mining and Technology

Principal Investigator: Sandip Tiwari, Electrical Engr, Cornell University, Tiwari@cnf.cornell.edu

Abstract:

Chemical-mechanical planarization (CMP) is a vital step in many processes, including wafer direct bonding. In this research, thermal oxide was grown on the silicon substrate wafers, which were subsequently patterned using photolithography techniques. Some of the wafers then underwent polycrystalline silicon deposition, while others were sputtered with tungsten. Both sets of wafers were polished so that the surface was a silicon dioxide field with either polycrystalline silicon or tungsten features. The dependence of surface roughness on features was investigated with both polycrystalline silicon and tungsten.

Introduction:

Wafer direct bonding potentially has many applications, including three-dimensional circuit integration and the fabrication of low power and low voltage CMOS devices [1]. Atomically smooth surfaces (< 0.5 nm surface roughness) on wafers are critical to achieving good bonding. Chemical-mechanical planarization is one viable method of polishing wafers, as it provides the surface smoothness of mechanical polishing without the entailing subsurface damage [2].

In order to integrate wafer bonding techniques into device fabrication, good bonding of patterned wafers must be realized. For this purpose, this research studied the use of CMP in creating damascene, or in-laid, dielectric structures, and the resulting surface roughness.

In a CMP process, the wafer is held in a rotating carrier head and is pressed against a rotating pad by a mechanical arm, as illustrated in Figure 1. The pad is covered with slurry, a colloidal dispersion of abrasive particles in an aqueous solution of reactive chemicals. The type of slurry and pad used are specific to material being polished. Process rate and uniformity is affected by a number of factors. The velocity of the wafer across the pad and the down

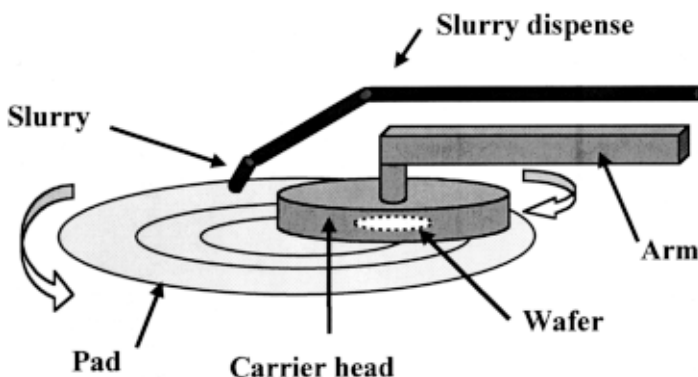


Figure 1. Schematic of Chemical-mechanical polishing.

force on the wafer change rate of material removal. The amount of slurry on the pad and the temperature are especially important with slurries where much of the polishing is preformed chemically. The back pressure on the wafer affects polishing uniformity from the center to the edges of the wafer.

Procedure:

In a LPCVD process, 300 nm of thermal oxide was grown on n-type, 4" silicon test wafers, which were then patterned using photolithography techniques. Approximately 700 nm of 620 photoresist was spun onto the wafers, and exposed using the GCA-6300 10x i-Line Stepper. The exposure mask was fabricated on a GCA PG-3600F Optical Pattern Generator. The smallest feature size was $.5 \mu\text{m}$. The wafers were etched 100 nm into the oxide using a reactive ion etching process on a PlasmaTherm 72.

Subsequently, the batch of wafers was split into two sets. One set of 8 wafers underwent 200 nm of polysilicon deposition with a LPCVD process. The other group of 10 wafers was sputtered with 160 nm of tungsten with a CVC AST-601 Sputter Deposition System.

A Strasbaugh 6EC with a Rodel IC 1400 pad was used in planarization. A Cabot Semi-Sperse P100 slurry was used for polishing the polysilicon. The manufacturers of this slurry claim that it has a 300:1 polysilicon to oxide selectivity, low defectivity on oxide and polysilicon surfaces, and results in excellent surface roughness. The tungsten slurry was composed of one part MSW2000A, an alumina oxide for abrasion, to 5.5 parts MSW2000B, a mixture of organic acid salts and oxidant complexes. This slurry had 30:1 tungsten to oxide selectivity.

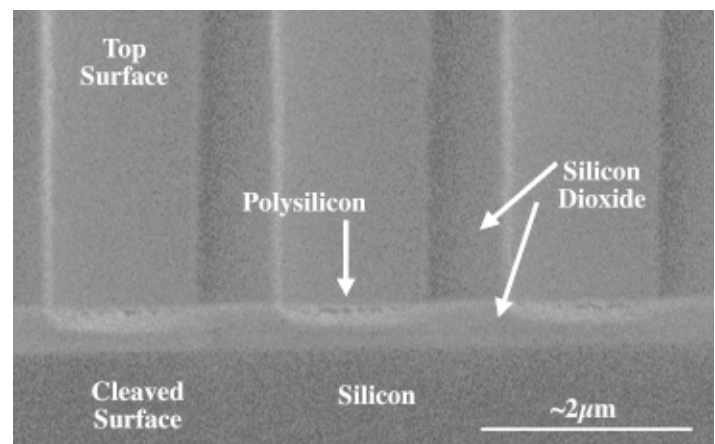


Figure 2. SEM image of damascene polysilicon.

Results:

Figure 2 shows a SEM image of the damascene polysilicon, obtained using a Leo (Zeiss) 982 Scanning Electron Microscope. Both the damascene polysilicon and tungsten were analyzed with a Digital Instrument Dimension 3100 Atomic Force Microscope. The vertical step height between the polysilicon and oxide is 21.986 nm. However, the surface roughness was excellent, 0.329 nm on the oxide and 0.487 nm on the polysilicon.

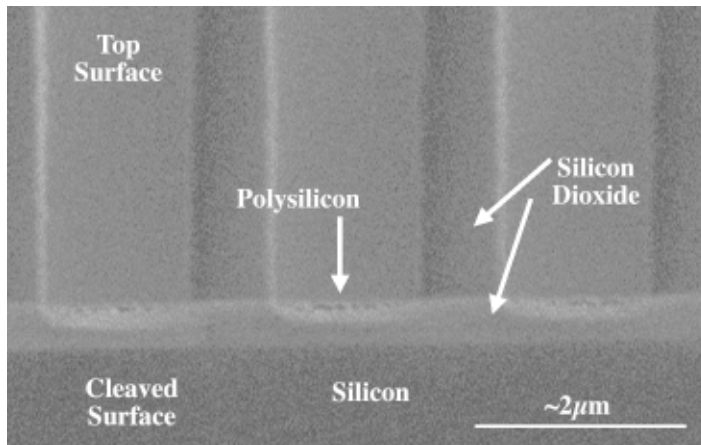


Figure 2. SEM image of damascene polysilicon.

The vertical step height between the oxide and tungsten is 13.846 nm. The surface roughness of the area of damascene tungsten shown in Figure 3 is 0.802 nm. The surface roughness over unpatterned areas of the wafer was on the order of 15 nm.

Conclusions:

The surface roughness of the damascene polysilicon is suitable for bonding; however, the step height between the polysilicon and oxide could potentially impede bonding. As seen on the AFM image of the damascene tungsten, there was insufficient slurry removal on these wafers, which resulted in high surface roughness. More characterization is required to polish damascene tungsten for bonding.

Acknowledgements:

My thanks to Helena Silva, Sandip Tiwari, Daniel Woodie, and the CNF Staff for their help and advice, and to NNUN and NSF for funding this research experience.

References:

1. J. Steigerwald, S. P. Murarka, R. J. Gutman, Chemical Mechanical Planarization of Microelectronic Materials, John Wiley & Sons: New York, 1997.
2. Q.-Y. Tong, U. Goesele, Semiconductor Wafer Bonding, John Wiley & Sons: New York, 1999.

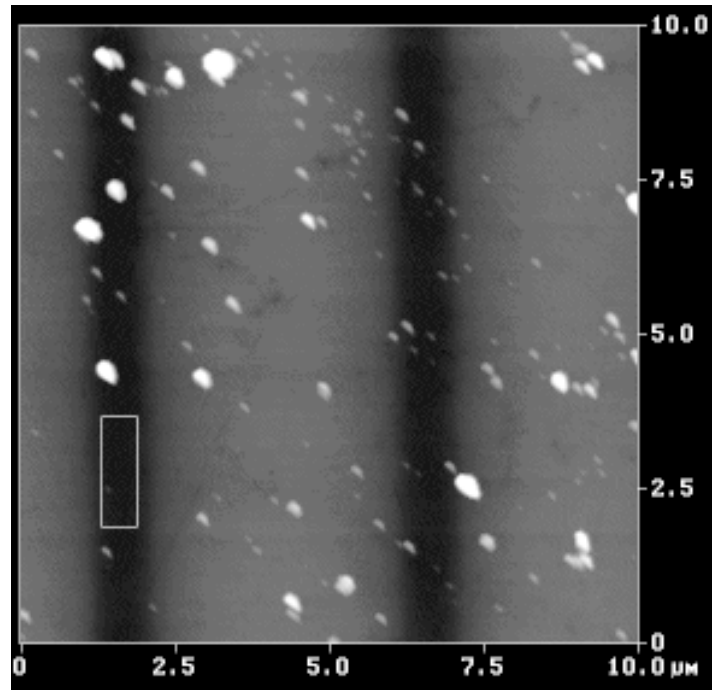


Figure 3. Surface roughness in outlined region of damascene tungsten is 0.802 nm.

Patterning Polymeric Materials

REU Intern: Jennifer Sui, Chemistry and Psychology, University of California Davis

Principal Investigator: Christopher Ober, MatSci & Engr, Cornell University, cober@ccmr.cornell.edu

Mentor: Dirk Schmaljohann, Material Science & Engineering, Cornell University

Abstract:

There is a strong interest in structuring polymer surfaces using photolithography and softlithography. Photolithography is used to create a hard master and the pattern is transferred to a polymeric substrate through softlithographic methods. To pattern different feature sizes on silicon wafers three photolithography methods are used.

My project covered two biomedical applications. Patterning of hydrogels which allows the study of cell adhesion and proliferation, was the first project. Besides the aspect of a fundamental understanding of cell behavior on structured surfaces, this investigation can lead to tissue engineering. The second project encompasses the formation of a patterned silicon rubber stamp used to structure bioactive compounds on a silicon surface. This can be a useful tool to detect and quantify biomolecules. Detection of diseases in blood is one possible application for this technique. All steps starting with designing a mask via CAD to creating a patterned hydrogel and a patterned silicon rubber stamp are accomplished.

Introduction:

With the growing technology and interest in biology emerged the new field of nanobiotechnology. Investigation of the micron and nano level allows one to study the behavior of biological molecules. Nanofabrication is a useful tool to create patterns with feature sizes that mimic that of biological molecules. Transfer of these features to polymeric surfaces allows for a more in depth study of the biochemistry because of its compatibility with biological molecules.

Two of the projects I worked on this summer were patterning poly(HEMA) and structuring a silicon surface with bioactive compounds. The former project involves the physical patterning of pHEMA hydrogels using soft-lithography in order to study the effects of surface topology on cell behavior. Biocompatibility of hydrogels is attributed to their ability to simulate living tissues due to large water content, softness, low interfacial tension with body fluids and permeability to metabolites, nutrients, and oxygen. Synthesis and characterization of polymeric hydrogels can be used as a design of polymeric scaffolds for tissue engineering application. The latter project involves the formation of a patterned rubber silicon stamp. The rubber stamp is used to structure silicon wafers using microcontact printing to create a biosensor.

To pattern the polymeric materials, we first fabricated silicon wafers with our desired pattern. There are several processes that are involved in fabricating silicon wafers. First, one must design the pattern and write the pattern on a mask. Using the mask containing the pattern, the pattern is transferred via photolithography. The sample is developed to remove the soluble areas.

The cleared areas are then dry etched using the appropriate gases. The remaining resist is stripped off using a base bath and the wafers are analyzed.

Experimental Fabrication:

CAD was used to design the mask, which consisted of 5 μm features with equal spacing and differing geometries. Leica/Cambridge EBMF 10.5/CS Electron Beam Lithography System was used to write the pattern on a LE glass mask. Many different photolithography tools were used to create the desired feature range of 1 μm to 2 μm . The 5 μm feature mask along with other masks already in the group was used to fabricate this range of features. All wafers were primed, spin coated, pre-baked, post-baked, and developed according to the manufacturer's description. In order to obtain a 1 to 1 transfer of the desired pattern, a HTG deep-UV contact aligner was used with S1813 resist. Wafers were etched using the Plasma Therm SLR-770 ICP Bosch Etcher to a depth of 2, 4, and 6 μm using the basic trench etch mode.

In order to obtain a five-fold reduction in feature size, we used a GCA-6300 5x g-line stepper using resist S1813. They were etched using Applied Materials Reactive Ion Etcher to a depth of 1 μm .

To achieve a ten-fold reduction in feature size, a GCA-6300 10x I-line stepper was used with 620-7i resist. They were etched to a depth of 0.5 μm . After the resist is stripped from the wafer, the wafer is analyzed using the Amray 1830TC Scanning Electron Microscope and Digital Instruments 3100 Atomic Force Microscopy (AFM) to insure complete pattern transfer.

Patterning Hydrogels:

HEMA was mixed with either EGDMA or TEGDA and 0.75%-wt of a water solution of 1:1 ammonium persulfate/sodium pyrosulfite mixture. The resulting solution was applied on a wafer, then heated at 37°C for 4 hours, to give clear patterned transparent films. Lift-off was achieved by swelling the hydrogel in water.

Patterning a Silicon Surface with Bioactive Molecules:

A silicon rubber stamp mixture consisting of a silicon precursor plus curing agent is mixed and poured over the patterned silicon wafer then heated in an oven at 60°C for about 2 hours. The replicated pattern silicon rubber stamp is physically peeled from the master silicon wafer. The rubber stamp is characterized using AFM to ensure complete pattern transfer. The patterned rubber stamp is then coated with $\text{CH}_3(\text{CH}_2)_{17}\text{SiCl}_3$ or OTS which acts like an ink. The stamp coated with OTS is then stamped on a silicon wafer transferring of the OTS pattern on the new silicon wafer.

Next, one backfills the wafer with bioactive molecules which forms the second self assembled monolayer. Then incubated with a biological macromolecule, i.e. antibody or protein. The specificity of the binding is characterized by fluorescent microscopy and this is the development of a model biosensor.

Results and Discussion:

We were able to create a large variety of silicon wafers, which later on were used for pattern transfer to polymeric materials. Figure 1 shows one example, the 5 μm squares. Proof of correct patterning was made in all cases by a combination of light microscopy, AFM and SEM. Pattern transfer to a polymeric material has been carried out using two different types of polymer (PDMS and polyHEMA), different feature sizes and geometries. Figure 2 shows one example, of a successful pattern transfer onto a silicon rubber stamp, which were 1 μm squares.

As also shown in other cases, a good pattern transfer from the master to rubber stamp was achieved. Currently, these stamps have

been successfully used to pattern OTS to silicon wafers with 5 μm feature sizes.

Conclusion:

We were successful in fabricating different master silicon wafers with our desired patterns. These masters have been replicated successfully to silicon rubber stamps, which will be used in further studies. Furthermore, pattern hydrogels based on polyHEMA have been used to study cell adhesion and proliferation, which have been fabricated using silicon wafers. There is much work to be done in the area of nanobiotechnology.

Acknowledgements:

Professor Christopher Ober, Dirk Schmaljohann, Wageesha Senaratne, and Federica Chiellini, and the National Science Foundation.

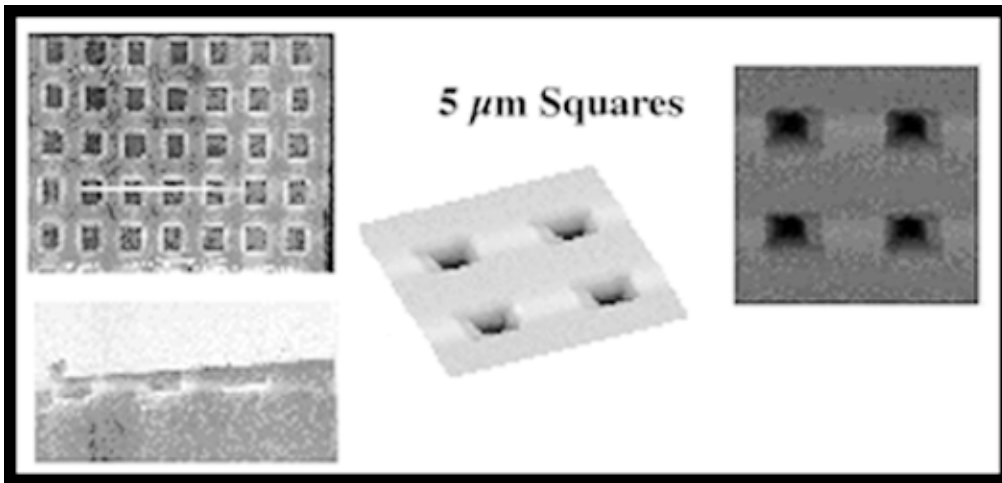


Figure 1, Left. Analysis of silicon wafers using SEM and AFM.

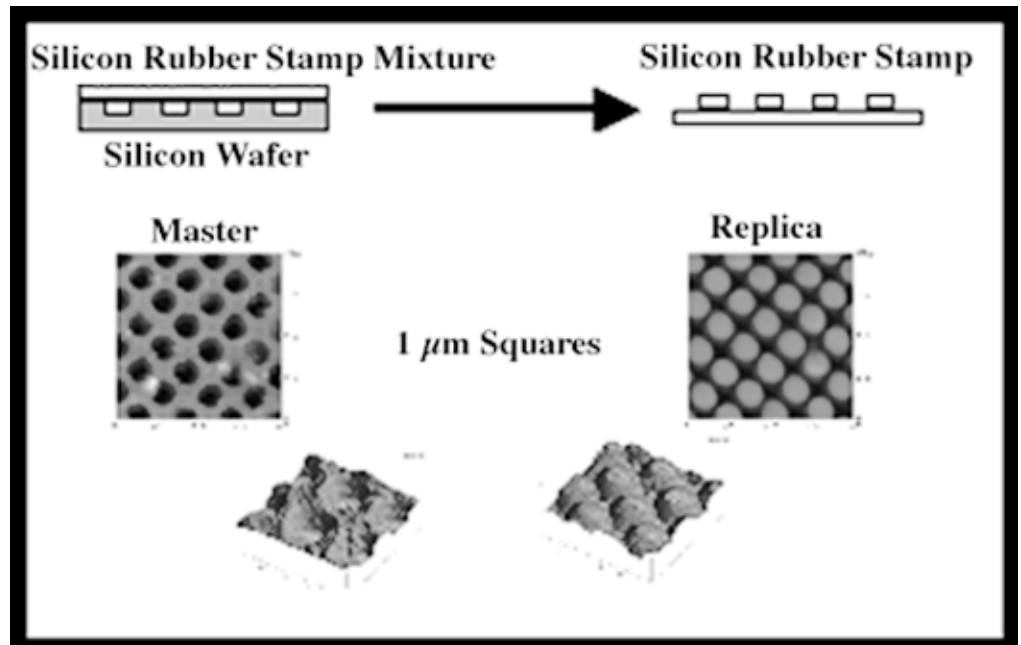


Figure 2, Right. Analysis of a rubber stamp using AFM tapping.

this page has intentionally been left blank

**Howard University
2000 REU Participants**



REU Intern

School Affiliation

Principal Investigator

From Left to Right:

| | | |
|------------------------------------|--|--------------|
| Ms. Sasha Rodriguez Gonzalez | University of Puerto Rico, Mayaguez Campus | Gary Harris |
| Ms. Tamisha Hawkins | Xavier University of Louisiana | Gary Harris |
| Ms. Jenea McLaughlin | University of Pennsylvania | Gary Harris |
| Ms. Andrea Lewis | Princeton University | Andre Palmer |

Excessive Nutrients in the Anacostia and Potomac Rivers

REU Intern: Tamisha Hawkins, Biology-premed, Xavier University in Louisiana

Principal Investigator: Gary L. Harris, Material Science Research Center of Excellence,
Howard University, gharris@msrce.howard.edu

Abstract:

Excessive nutrient enrichment from point and non-point sources is a principal cause of degradation in the Anacostia and Potomac rivers. The single largest point source of these rivers which are located in the District of Columbia, is the Blue Plains Wastewater Treatment Plant. Nitrogen and phosphorus are the two types of excessive nutrients that have a major impact on these rivers degradation. Removal of these nutrients from wastewater is becoming increasingly important to avoid problems to aquatic and human life.

This study focuses on two major areas: testing the amount of nitrogen and phosphorus concentrations in four different locations in the Chesapeake Bay area, and to use nanotechnology, such as a Scanning Tunneling Microscope and an Atomic Force Microscope to detect the particles present in the rivers.

Introduction:

In the District of Columbia, there are two major rivers that are affected by excessive nutrients (nitrogen and phosphorus). Excessive nutrient enrichment from point and non-point sources is a principal cause of the water quality's degradation (Bailey, 1998). The single largest point source is the Blue Plains Wastewater Treatment Plant. The current daily effluent discharge of total nitrogen from the Blue Plains Plant is approximately 18 metric tons (Bailey, 1998). The Chesapeake Bay Agreement of 1987, made to regulate and improve the nutrient load, called for an overall reduction in nutrient loading of forty percent of 1985 levels by the year 2000.

Nitrogen removal from wastewater is becoming increasingly important to avoid the problems of eutrophication in receiving water bodies. High concentrations of nitrates in drinking water can affect both aquatic life and humans. The primary health effect from high nitrate levels is methemoglobinemia which affects infants up to 6 months of age and can ultimately result in the infant's death (Gelberg et al., 1997). High concentrations of nitrate can also cause cancer and spontaneous abortions. Thus, some people may be more susceptible to contaminants in drinking water than the general population. People who have undergone organ transplants, people with HIV/AIDS or other immune system disorders, some older people and infants can be particularly at risk from infections.

Biological nitrification and denitrification have been employed for this purpose as they are economical and effective processes. Nitrification, which is the oxidation of NH_4 to NO_3 , is mediated by aerobic, chemoautotrophic bacteria (Henriksen & Kemp, 1988). Denitrification, the reduction of NO_3 to N_2 , is carried out by

facultatively anaerobic, heterotrophic bacteria (Koike & Sorensen, 1988). The denitrification process is directly limited by the nitrification.

This study focuses on two major areas: testing the amount of nitrogen and phosphorus concentrations in four different locations in the Chesapeake Bay area, and to use nanotechnology, such as a Scanning Tunneling Microscope and an Atomic Force Microscope to detect the particles present in the rivers.

Some sample images from AFM were included from other resources in order to study at bacteria and chemical structures.

It would be interesting to determine if the biological organisms and chemical structures found in the natural water bodies within the D.C. boundaries differ, one river from the other.

Materials and Methods:

TABLE 1.

Summary of the methods used to analyze water samples:

| <u>Indicator</u> | <u>Method Reference</u> |
|-------------------|--|
| Nitrate | Cadmium Reduction Method (Powder Pillows) HACH DR/2010 Spectrophotometer, 1996-1999 |
| Nitrite | Ferrous Sulfate Method HACH DR/2010 Spectrophotometer, 1996-1999 |
| Nitrogen, Ammonia | Nessler Method HACH DR/2010 Spectrophotometer, 1996-1999 |
| Total Phosphorus | PhosVer 3 w/Acid Persulfate Digestion Test CEN Tube HACH DR/2010 Spectrophotometer, 1996-1999 |

Sample Preparation for Atomic Force Microscopy:

Glassware is acid washed and rinsed three times with DI water.

- Step One: Filter sample through a glass fiber filter (approx. 1.5 mm).
- Step Two: Filter filtrate through a membrane filter with pore size of 1×10^{-9} .
- Step Three: Dry filter for 24 hours at 105°C .
- Step Four: Place filter in the dessicator for two hours to remove any latent humidity or until microscope is ready.
- Step Four: Place under microscope and take picture.

Results:

We charted the samplings of the chemical elements and compounds taken from the water at each location. Location 1 represented the point in the Potomac river right after the Blue Plains Waste Water Treatment Plant. Location 2 represented the point where the Potomac and Anacostia rivers meet. Location 3 represented the point in the Potomac river before the Waste Water Treatment Plant. Location 4 represented the Anacostia River.

Conclusion:

The Environmental Protection Agency requires that the nitrogen concentrations released into a body of water should be as shown:

Ammonia Nitrogen-.32mg/L

Nitrate-7.2mg/L

Nitrite-1.0mg/L

Anything higher than this can begin to cause problems.

Our results showed that the Anacostia river exceeds the normal amount of ammonia nitrogen concentration in a water body. Every other location has a normal amount of each type of nitrogen, meaning that the Blue Plains Wastewater Treatment Plant is very accurate on how much nitrogen they release into the Anacostia and Potomac Rivers. Future research activities can utilize the Atomic Force Microscope and the Scanning Tunnel Microscope to detect and analyze biological organisms and chemical structures.

Engineering Porphyrin Encapsulated Vesicles for Metal Removal from Wastewater

REU Intern: Andrea N. Lewis, Chemical Engineering, Princeton University

Principal Investigator: Andre Palmer, Chemistry, Howard University,
apalmer@electron.chem.howard.edu

Abstract:

The kinetics of Zn^{+2} metal incorporation into porphyrin encapsulated phosphatidylcholine (PC) vesicles (or liposomes) was studied using spectrophotometry. (Figure 1) Liposomes, made by controlled detergent dialysis, were characterized by multiangle static light scattering to prove that they were unilamellar and monodisperse in size. The average radius of the vesicles was engineered to be 40 to 127 nm and was varied by changing the lipid-detergent molar ratio.

Both the positively charged Tetra (N-Methyl-4-Pyridyl) Porphyrin (TMPyP[4]) and the negatively charged Tetra (4-Sulfonatophenyl) Porphyrin (TPPS) were used for zinc incorporation into the vesicles. (Figure 2) This method of making porphyrin encapsulated vesicles that are homogenous in size, may prove useful in the removal of metal ions from wastewater.

Introduction:

Liposomes, or vesicles, consist of one or more lipid bilayers enclosing an aqueous compartment. They are capable of encapsulating either hydrophilic components in their aqueous interior or hydrophobic compounds in their bilayer membrane [1, 2]. Unilamellar vesicles have been widely used as models for biological cell membranes [2-5]. They have also been employed in the delivery of drugs, and other substances, to cells [1-5].

Porphyrins were encapsulated by liposomes because they bind to metal ions in a non-reversible reaction. Consequentially, these types of vesicles may have applications in wastewater cleanup. The removal of metal ions from industrial effluent is an extensive environmental problem [6-8]. Metal ions are extremely toxic and pose a considerable threat to human and aquatic life when present in the environment. Porphyrin encapsulated vesicles may have an advantage over other cleanup processes because after metals have been incorporated into the vesicles, they can easily be filtered out. Additionally, liposomes are biodegradable and can be separated from the metalated porphyrins and recycled.

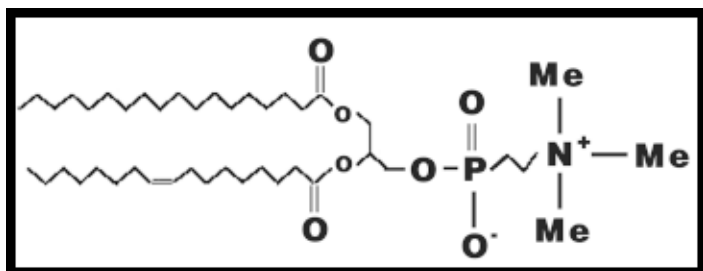


Figure 1. Chemical structure of 1,2-diacyl-*sn*-glycerol-3-phosphoryl choline (Phosphatidylcholine)

Methods:

The lipid film was prepared by evaporating the chloroform solvent using a rotary evaporator. Variable amounts of sodium cholate detergent was added to the dried lipid film obtaining a lipid-detergent ratio in the range of 0.29 - 1.24. The mixture was then dissolved in 1mL of 0.9-wt. % NaCl buffer, pH 6.8. Solid porphyrins were then dissolved in this solution. The final lipid concentration was 50 mg/ml and the final porphyrin concentration was varied from 5-50 mg/ml. Detergent removal was carried out using a Mini LipoPrep instrument (AmiKa Corp., Columbia MD). The dialysis procedure took place at room temperature. Vesicle samples were kept at room temperature in the dark until use.

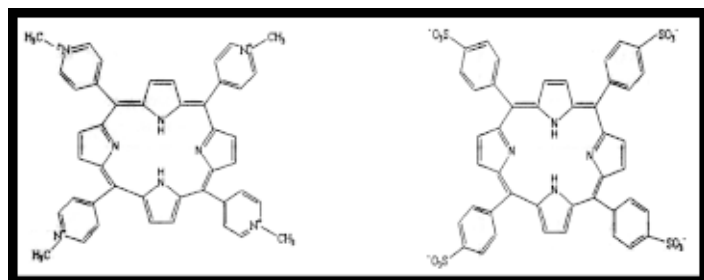


Figure 2. Structure of (a) Tetra (N-Methyl-4-Pyridyl) Porphyrin and (b) Tetra (4-Sulfonatophenyl) Porphyrin used in the experiments

A Dawn Enhanced Optical System (EOS) (Wyatt Technology, CA) light scatterer was used to determine the mean radius of the vesicles in solution. Data was analyzed using Astra (Wyatt Technology, CA) software. The values of $R(\theta)$ (scattered intensity) versus q (scattering vector) were displayed by the software. It was assumed that $R(\theta) \propto P(\theta)$ for the dilute solutions used here. The data was then fit using KaleidaGraph (Synergy software) according to the form factor for a hollow sphere $P(\theta)$ [2, 5, 9]. In this study, we assumed the bilayer thickness to be 3.7nm based upon previous measurements [5].

All absorption measurements were performed using a Beckman DU-70 Spectrophotometer. Only TMPyP[4] was used in the absorption measurements. In all of the spectroscopic studies the final lipid concentration of the vesicle solution was 6.58×10^{-2} mM, the final TMPyP[4] concentration was 8.69×10^{-5} mM and the zinc concentration was 0.114 M.

Results and Discussion:

Light scattering studies were performed on several sets of TMPyP[4] encapsulated vesicles. Changing the lipid-detergent ratio varied the vesicle radius. The data indicates that the vesicle size increased as the lipid-detergent ratio was increased. This trend was experimentally verified by other investigators [3, 4].

At a constant lipid-detergent ratio, both negative (TPPS) and positive (TMPyP[4]) porphyrins were encapsulated by vesicles. These vesicles were characterized and compared to the experimental control consisting of pure vesicles with no encapsulated material.

We found that both the negative and positive porphyrin encapsulated vesicles had larger radii than the experimental control (Figure 3). Furthermore, the TPPS encapsulated vesicles were found to be slightly larger than the TMPyP[4] vesicles. While it is not entirely clear why this phenomenon occurs, we believe that vesicle size increases after porphyrins are encapsulated simply because the large number of porphyrin molecules enclosed within the vesicles causes them to enlarge. The minor change in size between the TPPS vesicles and the TMPyP[4] vesicles can probably be attributed to the difference in structures of the two porphyrins.

In aqueous solution, ionic strength 1M, TMPyP[4] presents absorption maxima at 422.0, 518.4, 553.8, 584.0, and 640.4 nm [10]. After zinc addition the resulting spectrum displays maxima at 436, 560, and 602 nm [10]. The absorption spectrum of TMPyP[4] encapsulated vesicles before and after zinc addition (Figure 4) reflects this data indicating that zinc ions successfully crossed the lipid bilayer and were incorporated into the porphyrin molecules. In our experiments we calculated the equilibrium constant for the reaction to be $4.02 \times 10^{-3} \text{ M}^{-1}$ at ionic strength of approximately zero.

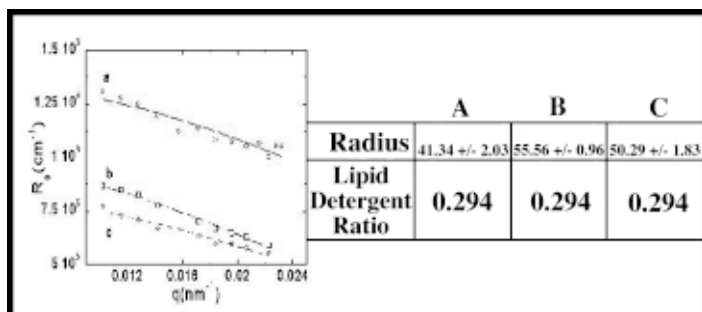


Figure 3. Vesicles with the same lipid-detergent ratio that have; (a) no porphyrins, (b) TPPS inside, (c) TMPyP[4] inside

Conclusion:

Both TPPS and TMPyP[4] encapsulated vesicles were prepared by controlled detergent dialysis and characterized by light scattering to determine size and homogeneity. Zinc was successfully incorporated by the vesicles and into TMPyP[4] porphyrins. These results were confirmed by analyzing the absorption spectrum of the TMPyP[4] vesicles prior to and following zinc addition. The size of porphyrin encapsulated vesicles makes it possible for them to be filtered out of solution. Therefore, these types of vesicle may have application in wastewater cleanup.

References:

1. K Andrieux, S Lesieur, M Ollivon, C Grabielle-Madelmont, "Methodology for Vesicle Permeability Study by High-Performance Gel Exclusion Chromatography", 1998.
2. JH Van Zanten, "Characterization of Vesicles and Vesicular Dispersions via Scattering Techniques."
3. V Rhoden, SM Goldin, "Formation of Unilamellar Lipid Vesicles of Controllable Dimensions by Detergent Dialysis", 1979.
4. O Zumbuehl, G Weder, "Liposomes of Controllable Size in the Range of 40 to 180 nm by Defined Dialysis of Lipid/Detergent Mixed Micelles", 1981.
5. B Korgel, JH van Zanten, HG Monbouquette, "Vesicle Size Distributions Measured by Flow Field-Flow Fractionation Coupled with Multiangle Light Scattering", 1998.
6. Z Ujang, GK Anderson, "Application of Low-Pressure Reverse Osmosis Membrane for Zn^{+2} and Cu^{+2} Removal from Wastewater", 1996.
7. M Bodzek, I Korus, K Loska, "Application of the Hybrid Complexation-Ultrafiltration Process for Removal of Metal Ions from Galvanic Wastewater", 1999.
8. CJ Williams, D Aderhold, RGJ Edyvean, "Comparison Between Biosorbents for the Removal of Metal Ions From Aqueous Solutions", 1998.
9. S Rossi, S Ristori, G Pozzi, G Martini, "Spectroscopic Characterization of Fluorinated/Hydrogenated Mixed Vesicles containing Fluorinated Mn(III)-Porphyrin", 1998.
10. P Hambright, "Chemistry of Water Soluble Porphyrins", 2000.

Acknowledgements:

Thanks to Dr. Andre Palmer, Dr. Peter Hambright, the Materials Science, Chemistry, and Engineering Departments of Howard University, the National Nanofabrication Users Network, and the National Science Foundation.

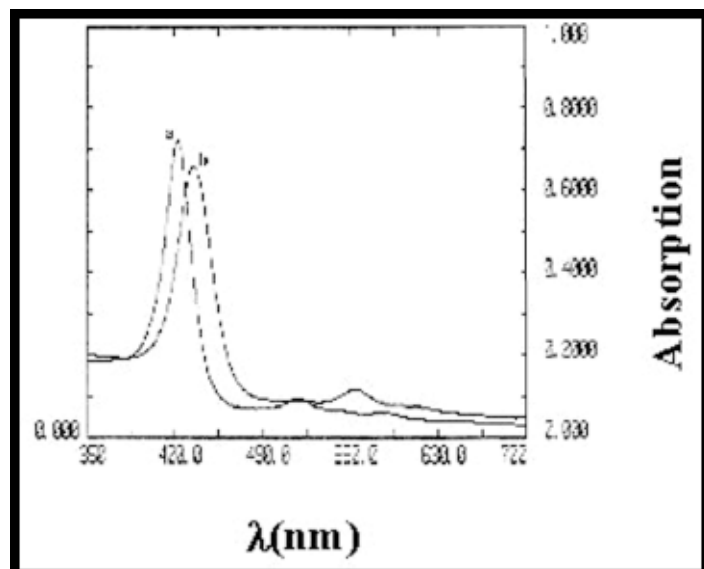


Figure 4. Absorption spectrum of positive porphyrin encapsulated vesicles (a) before Zn^{+2} incorporation and (b) after Zn^{+2} incorporation

SiC Retina for Subretinal Applications

REU Intern: Jenéa McLaughlin, Bioengineering, University of Pennsylvania

**Principal Investigator: Gary L. Harris, Materials Science Research Center of Excellence,
Howard University, gharris@msrce.howard.edu**

Abstract:

Silicon carbide is a wide band-gap semiconductor with many advantages over silicon. These two materials were compared to determine which is more suitable for a retinal replacement material. Silicon and silicon carbide solar cells were fabricated using lithography to replace the function of damaged photoreceptor cells in the human retina. Zebrafish, a tropical freshwater fish, were used in tests as animal models because their optical system is similar to that of humans. The voltage output in electroretinogram tests using white light was 5 μ volts. The efficiency of each cell was determined by calculating the fill factor value and determining the open-circuit voltage. The silicon cell generated an open-circuit voltage of 0.41V with an efficiency of 9.0%, while the silicon carbide cell generated an open-circuit voltage of 0.9V with 0.7% efficiency.

Introduction:

Retinitis Pigmentosa (RP) and Age-related Macular Degeneration (AMD) are two diseases of the human retina that cause damage to the photoreceptors of the eye. Patients with RP usually report impaired adaptation, night blindness, and loss of mid-peripheral visual field in adolescence (Nadig, 1999). As the disease progresses, all vision is eventually lost. In age-related macular degeneration, the area of the eye with the highest density of light sensing cells (the macula) degenerates, leading to slow or sudden loss of central vision.

These degenerative diseases make a retinal implant that replaces the damaged cells highly desirable. Two approaches that are currently in use are the epiretinal and subretinal approaches. The epiretinal approach is used to stimulate the ganglion cells and their axons on the surface of the retina, with stimulators that receive signals generated by an external or implanted data processing system (Zrenner, 1999). The disadvantage of this approach is that some signal processing is necessary to allow communication between the stimulators and the device. The subretinal approach is used to replace the degenerated photoreceptor cells by placing a chip in the subretinal space of the retina, located just before the ganglion cells. This approach bypasses the damaged photoreceptors and directly stimulates the ganglion cells, therefore eliminating the need for complicated signal processing. The key to each approach is that the optic nerve must remain intact. Without the optic nerve, the signals that are generated cannot be transported to the brain for processing.

In the present study, solar cells are used to create the voltage necessary to stimulate the remaining viable cells of the retina. These devices operate by converting sunlight directly into electricity using the electronic properties of semiconductors (Green, 1982). This

process is dependent on the photovoltaic effect. The energy from the sun is used to excite electrons, and move them to the conduction band of the semiconductor. The electron-hole pairs that are created cause an open-circuit voltage, which can lead to current flow.

Currently, silicon is being used to fabricate retinal replacement devices. However, silicon carbide offers more advantages for the present application. Silicon carbide is a wide band gap semiconductor, which is less sensitive to increased temperatures; therefore, the silicon carbide solar cells are able to withstand the increased temperature of the body. Silicon carbide is an inert material, and is resistant to unfavorable chemical reactions, offering excellent stability. Silicon carbide also has a higher open circuit voltage than silicon; therefore a silicon carbide solar cell can generate a higher output voltage than silicon.

Procedure:

I. Lithography Process

1. Standard cleaning of the sample with soap solution, trichlorethylene, acetone, methanol, and deionized water.
2. Hydrofluoric acid dip for 30 seconds.
3. Prebake at 95-105°C for 5 minutes to remove excess water.
4. Spin on 0.8 μ m photoresist for 30 seconds at 4000 rpm.
5. Prebake at 95-105°C for 30 minutes .
6. Expose sample to UV light using mask 1 (fig. 1) for 12 seconds.
7. Soak in toluene for 60 seconds and rinse in deionized water.
8. Develop for 60 seconds and rinse in deionized water.
9. Postbake at 120°C for 20 minutes.

II. Ohmic Contact

1. Deposit 2500 Å of nickel-gold using an electron-beam evaporator and liftoff excess metal using acetone.
2. Anneal at 650°C for 1 minute.
3. Probe sample and test I-V characteristics to ensure that the contact is Ohmic.

III. Transparent Schottky

1. Follow steps 3-8 of the lith process using mask 2 (fig. 2).
2. Deposit 100 Å of aluminum using the electron-beam evaporator and liftoff excess metal using acetone.

IV. Schottky Contact

1. Follow steps 3-8 of the lith process using mask 3 (fig. 3).
2. Deposit 2500 Å of aluminum using the electron-beam evaporator and liftoff excess metal using acetone.

V. Testing

1. Check the I-V characteristics with and without light.
2. Calculate the efficiency of each solar cell by determining the open-circuit voltage.

VI. Electroretinogram

1. Anesthetize the zebrafish using 100 mg/L of Tricaine in water.
2. Connect two boron silicate electrodes to the fish — one behind the fin and one on the eye.
3. Read the output voltage.

Results and Conclusions:

The open circuit voltage of the silicon cell was 0.41V, while the open circuit voltage of the silicon carbide cell was 0.9V. These values show that the voltage generated by a silicon carbide cell is more than twice that of a silicon cell. Silicon carbide characteristically has a low efficiency compared to other solar cells. The calculated efficiency of the silicon carbide cell in this experiment was 0.7% compared to 9.0% for the silicon cell. The area of each cell was $3.6 \times 10^{-3} \text{ cm}^2$, however the entire chip is about 2 mm.

Although silicon is much more efficient than silicon carbide, it does not produce the voltage necessary to stimulate the ganglion cells of the retina. Therefore, we concluded that silicon carbide is a better material for fabricating a retinal prosthesis to stimulate the ganglion cells of the human retina. We also concluded that silicon carbide is more biocompatible than silicon because of its inertness. However, a better metal than gold must be chosen for the contacts because of its tendency to flake. Titanium should be considered as the metal of choice for these contacts.

Zebrafish were used in tests as animal models to perform a test called an electroretinogram. These fish were used because their optical system is very similar to humans, and they have also been used in experiments studying colorblindness. The output voltage was measured at approximately 5 μ volts with white light. This value is a measure of the electrical activity of the retina, and gives us an idea of how this activity changes with white light.

Also, the mask set must be optimized to accommodate the subretinal space and maximize the number of cells that can be placed on one chip. Optimally, thousands of nanoscale solar cells should fit on one chip with each cell isolated from other by etching. Therefore, each individual solar cell will act as one photoreceptor connected to the optic nerve to provide spatial resolution. An anti-reflective coating should also be considered to increase the efficiency of the silicon carbide cell.

References:

- [1] Green, Martin A., 1982. "Solar Cells: Operating Principles, Technology, and System Applications."
- [2] Nadig, Malini N., 1999. "Development of a Silicon Retinal Implant: Cortical evoked Potentials following Focal Stimulation of the Rabbit Retina with Light and Electricity". *Clinical Neurophysiology* 110(9), pp.1545-1553.
- [3] Spalton, David J., Roger A. Hitchings, and Paul A. Hunter, 1994. "Atlas of Clinical Ophthalmology", 2nd ed.
- [4] Zrenner, E. et al., 1999. "Can Subretinal Microphotodiodes Successfully Replace Degenerated Photoreceptors?" *Vision Research* 39(15), pp. 2555-2567.

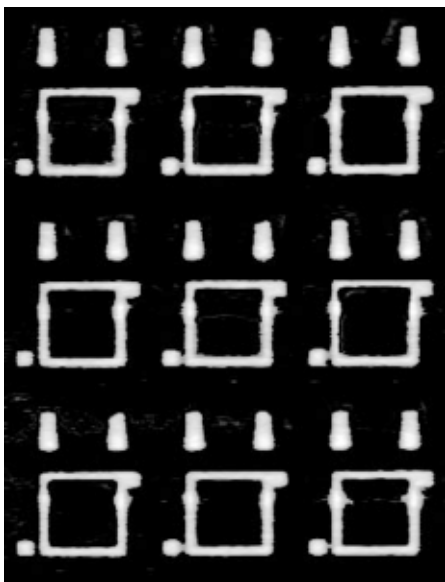


Figure 1. MASK 1

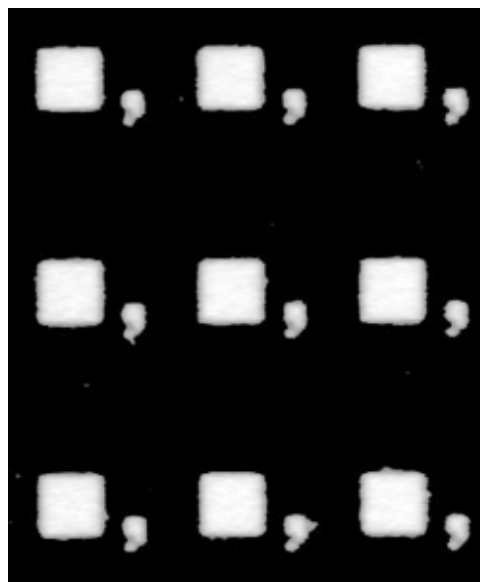


Figure 2. MASK 2

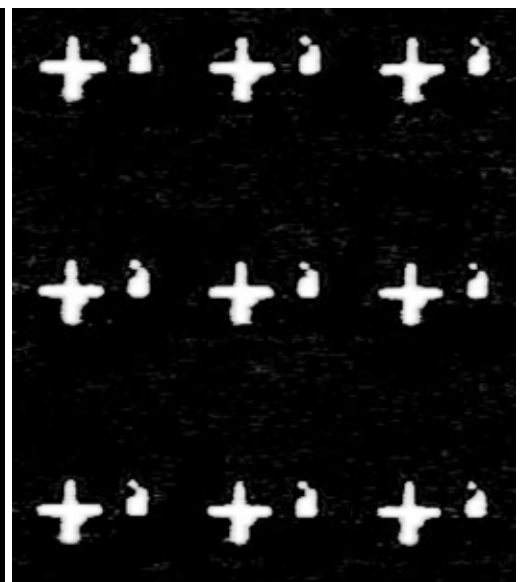


Figure 3. MASK 3

Organic Material Binding to Inorganic Material at a Nanoscale Level

REU Intern: Sasha Rodriguez, Industrial Engineering, University of Puerto Rico, Mayaguez Campus

Principal Investigators: Gary L. Harris, Electrical Engr, Mamadou Diallo, Civil Engr and Chemistry, Howard University, gharris@msrce.howard.edu, diallo@wag.caltech.edu

Mentor: James Griffin, MSRCE, Howard University

Abstract:

The selective binding of organic molecules to semiconductor surfaces has been recently studied for several new nanostructures. This binding could lead to the manufacture of nanosensors for medical applications, and the creation of ultrasmall electronic computer logic.

There are some viral molecules called peptides that bind selectively to different semiconductor surfaces. In this study, we examined the selective binding of some of these peptides to semiconductor materials such as GaAs, Si, InP, InAs and SiC. We exposed the surfaces to two different peptide solutions for different periods of time, and used Atomic Force Microscopy to search for peptide binding. After trying several procedures, we observed formations on some surfaces. However, we were unable to determine whether or not they were peptides.

Introduction:

Over the past years, researchers have been studying new alternatives for making electronic connections smaller. They've found that peptides — short amino acid sequences found in viral surfaces — bind selectively to semiconductor material. This should provide the building blocks for the manufacture of complex electronic structures.

In an experiment done at the University of Texas, Austin, five semiconductor surfaces, GaAs(100), GaAs(111)A, GaAs(111)B, InP(100), and Si(100), were exposed to a library of random peptides. After exposing for several time periods the surfaces were rinsed leaving just the peptides that bound. They found some peptides that bound to GaAs(100) and others that bound to InP(100).

In our experiment, we continued this peptide behavior study selecting two sequences from the ones found in Austin, and exposing more semiconductor surfaces to them.

Procedure:

For this experiment, first of all, we randomly selected two peptide sequences from the experiment previously done at Austin. We prepared two peptide solutions in a Tris-buffered saline (TBS), mixing 10mg of pure peptide with 20ml of Tris. These peptide solutions were named as G1-3 that contained the amino acids: R L E L A I P L Q G S G and G12-3 that contained: A Q N P S D N N T H T H. The surfaces that we used were: GaAs(100), InP(100), InAs(100), Si(100), and SiC(100).

A) Surface Cleaning:

After cutting the surfaces (1cm x 1cm), we washed them with

5 ml of acetone and 5 ml of methanol. Then we rinsed with water and introduced it to an etching solution of HCl:H₂O 1:10 to remove impurities. Then we rinsed again with water and the surfaces were ready for the exposure.

B) Surface Exposure:

Once the surfaces were cleaned, we exposed each surface to the peptide solution. We exposed for different periods of time, 15 minutes, 1 hr, 16 hrs, 22 hrs and 40 hrs.

We also tried several methods of rinsing the surfaces after they were exposed. We first rinsed with water, but then we tried preparing a Tween-20 solution of increasing concentrations from 0.1% to 0.5%. The Tween-20 was kept in the surface making it difficult to see whether there were peptides or not, so we kept rinsing with water. After cleaning, exposing and rinsing, we used Atomic Force Microscopy to search for peptides on the surface.

Results:

After searching for peptides with the Atomic Force Microscope, we found formations in some of the surfaces. Please see figure one, opposite.

Conclusion:

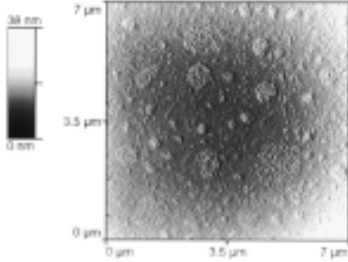
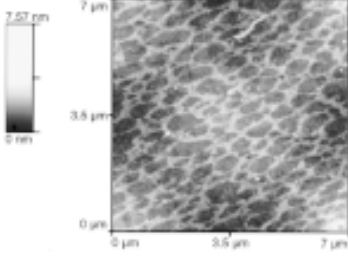
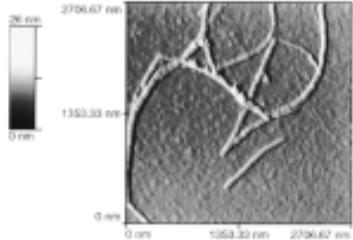
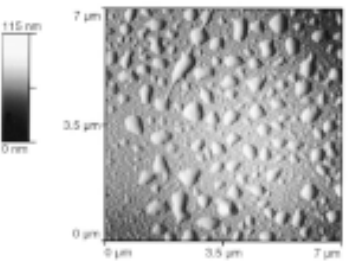
In this experiment, we exposed several surfaces to two different peptide solutions and we used Atomic Force Microscopy (AFM) to search for peptide binding. Since we didn't have a pattern to follow with AFM, we were unable to identify the formations that were found as peptides. Future investigations will involve using other techniques to identify peptides in semiconductor surfaces.

References:

- [1] Reed, Mark A. and Tour James M. "Computing with Molecules"; Scientific American, pp.86-93, June 2000.
- [2] Whaley, Sandra R., Hu, Evelyn L., Barbara, Paul F., & Belcher, Angela M. "Selection of Peptides with Semiconductor Binding Specificity for Directed Nanocrystal Assembly"; Nature, Vol 405, pp 665-668, June 2000.
- [3] Alivisatos, A.P. "Organization of Nanocrystal Molecules Using DNA"; Nature, Vol 382, pp. 609-611, 1996.

Acknowledgements:

I would like to thank Gary Harris, James Griffin and the staff of the MSRCE at Howard University for their assistance and support through the entire program.

| Surfaces: | G12-3 solution: | G1-3 solution: |
|---|---|--|
| <p>GaAs(100) Exposed to the G12-3 solution for 4hrs and rinsed with the Tween-20.</p> |  | <p>When exposed to this solution for 4hrs, no formations were found.</p> |
| <p>InAs(100) Exposed to the G12-3 solution for 40hrs and rinsed with water.</p> |  | <p>When exposed to this solution for 40hrs, no formations were found.</p> |
| <p>InP(100) Exposed to the G1-3 solution for 22 hrs and rinsed with water.</p> | <p>When exposed to this solution for 22hrs, no formations were found</p> |  |
| <p>GaAs(100) Exposed to the G12-3 solution for 16 hrs and blow dried without rinsing.</p> |  | <p>When exposed to this solution for 16hrs, no formations were found.</p> |
| <p>SiC(100) Exposed to both solutions and rinsed with water.</p> | <p>No formations found</p> | <p>No formations found</p> |
| <p>Si(100) Exposed to both solutions and rinsed with water.</p> | <p>No formations found</p> | <p>No formations found</p> |

this page has intentionally been left blank

The Penn State Nanofabrication Facility 2000 REU Participants



REU Intern

School Affiliation

Principal Investigator

From Left to Right:

| | | |
|--------------------------------|--------------------------------------|-------------------|
| Ms. Nga Nguyet Dinh | University of Nebraska Lincoln | Stephen Fonash |
| Mr. David Badillo Torres | University of PR Aguadilla | Carlo Pantano |
| Ms. Ly Xuan Thi Nguyen | Colorado State University | Jogender Singh |
| Mr. William Fadgen | University of Texas Dallas | David Allara |
| Mr. Jevon Johnson | Xavier University of Louisiana | Nicholas Winograd |
| Ms. Kwanza Nicole Brown | Eastern College | Stephen Fonash |

Coating and Etching Glass Substrates for DNA Microarray

REU Intern: David Badillo Torres, Biology, University of Puerto Rico in Aguadilla

Principal Investigator: Carlo G. Pantano, Mat Sci. Eng., Pennsylvania State University, cgp1@psu.edu

Mentor: Amy Barnes, Mat Sci. Eng., Pennsylvania State University

Abstract:

Phosphate glass is a versatile material that has been used in multiple applications such as laser glass, wave-guides and biomedical implants.

The objective of this project was to study the physical and chemical response of the lanthanum sodium-alumino-phosphate glass surface after exposure to various aqueous organic environments. The glasses were treated in both acidic and basic solutions and also with a polyamide compound. The resulting surfaces were analyzed by both atomic force microscopy (AFM) and x-ray photoelectron spectroscopy.

In addition, the adhesion of nucleic acid to the polymer-coated glass was examined using the DNA microarray facility. The analysis of nucleic acid retention was performed by the scanning of dye-labelled DNA previously printed on the glass using the DNA microarray robotic arm.

Introduction:

The quality and surface coating of the glass substrate are fundamental factors for a successful DNA microarray system. A poor quality substrate will lead to a low DNA binding efficiency and hence, to a poorly defined fluorescent image. This research was designed to better understand the interactions between a lanthanum-sodium-aluminophosphate glass surface and various organic and aqueous environments. The information will then be applied to how the surface performs as a DNA microarray substrate compared to the more popular silicate-based substrate. In addition, a photolithographic technique was used to fabricate a patterned phosphate glass surface as a potential microsystem in the study of nucleic acids.

Procedure:

Surface Cleaning and Coating:

The research was done on two glass substrates: a lanthanum sodium aluminophosphate glass and a borosilicate glass. Initially, two different cleaning procedures were used, an ethanol sonication that simply removes loosely bound debris and oils, and a combination base and acid etch which essentially strips away the outer surface, exposing a fresh glass layer.

The phosphate and borosilicate glass were coated with 3-aminopropyl- triethoxysilane following the procedure designated by the Biofacility. Alternatively, the glass surface was coated with a low molecular weight polyamide. For this task, the slides were placed in the polymer solution for 24 hours, then sonicated in RO water for 15 minutes to remove as much loosely bound (physisorbed) polymer from the surface as possible.

DNA Array:

Prior to the printing process, fluorescently labeled probes were prepared from yeast DNA, incorporating Cy3-labeled nucleotides from Amersham Pharmacia Biotech. The DNA samples were spotted onto all slides using a Robotic microarrayer and cross-linked by UV light at 1900 micro joules*100.

After the UV cross-link, the slides were washed in 0.1% SDS and then in water for 30 seconds respectively. Finally, the printed slides were immersed sequentially in boiling water for 3 minutes and ethanol for 2 minutes. Determination of the slide's success as a microarray substrate was performed by scanning the slide with a Scan Array 3000 confocal laser scanner.

Photolithography:

Fresh phosphate glass surfaces were patterned using photolithographic techniques. The glasses were first cleaned in ethanol to remove all surface debris. The samples were then coated with a thin layer of aluminum using an electron beam evaporator. Next, a layer of photo-resist was coated onto the surface. A mask was placed on the surface and the entire system was exposed to uv-radiation, removing the photo-resist in the exposed areas. The exposed aluminum layer was removed with an acid etch, exposing a pattern of bare glass. To etch the glass, a combination acid/base etch was used. The glass was soaked in 3M KOH for 2.5 minutes followed by 3M HCL for 30 seconds. The patterned surface was imaged with the atomic force microscope.

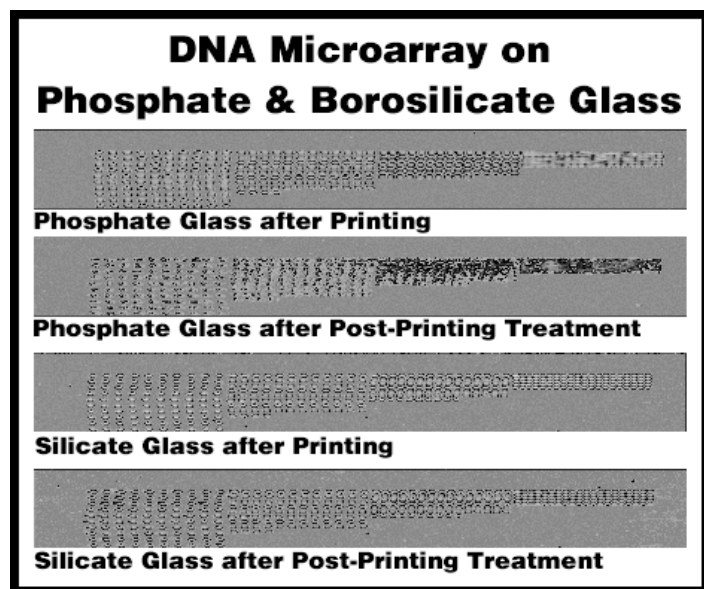
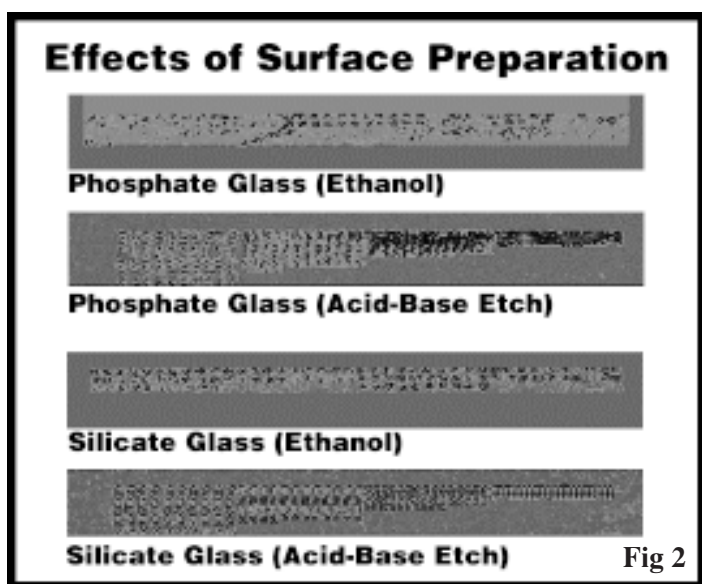


Figure 1

Results:

Figure 1 shows the DNA microarray on the phosphate and borosilicate glass. The slides were cleaned by a combination of acid and base etch and then coated with 3-aminopropyl-triethoxysilane. The silicate glass microarray features well defined and distributed spots which is indicative of a good DNA adhesion. The phosphate glass did not effectively retain the DNA, causing the spots to disperse rather than attach to the glass.

In a second experiment, we used ethanol as the cleaning agent while keeping the same 3-aminopropyl-triethoxysilane coating on the slides. For this test, the slides were sonicated in ethanol for 15 minutes followed by the coating and DNA print. Figure 2 shows

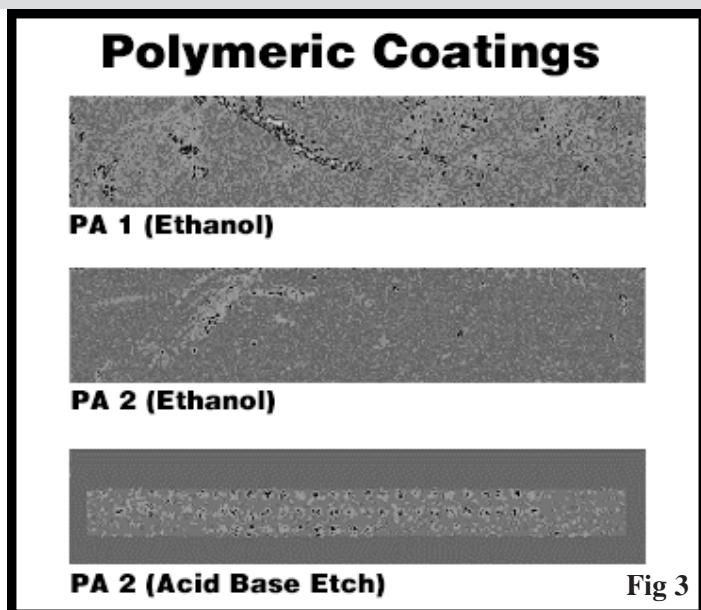


the scanned images of this experiment. The attempts at creating an adhesion between the DNA and the phosphate and borosilicate glass substrates was ineffective, as the array lacked fluorescence and the printed spots dispersed through the slides's surface.

Alternatively, the phosphate glass surface was coated with a low molecular weight polyamide (PA) at different pH levels: PA1 at pH 5.5 and PA2 at pH 10.4. Two different cleaning protocols were used on this experiment: a standard acid and base etch, and a fifteen minutes sonicating in ethanol. Figure 3 shows the resulting images of this experiment. The ethanol-cleaned slides, coated with either polymer, did not bind to the DNA. PA2 coated slides previously cleaned with an acid and base etch were also ineffective for the retention of the DNA, as the spots scarcely adhered to the slides's surface.

A photolithographic technique was used to fabricate a patterned phosphate glass surface as a potential microsystem in the study of nucleic acids. The etched pattern consisted of multiple pits of different sizes ranging from 5 to 100 μ m. The pits can be used as individual reaction chambers for the retention of nucleic acids.

Figure 4 shows images of the 5 μ m pit and the etched pattern on the phosphate glass, taken with the atomic force microscope. The borders of the pit on figure 4 are not completely square, but that can be enhanced by using different etching on the glass or by evaporating different metals.



Conclusion:

The phosphate glass was not as effective for the adherence of DNA compared to the silicate based system. The ethanol cleaning of the glass was found to be less effective than the acid and base etch for the application of the aminopropyl-triethoxysilane, resulting in less DNA retention on the microarray. Also the coating of the glasses with the polyamide based polymers caused an increase in surface roughness of the glasses thus contributing to the lack of coupling of the DNA to the glass.

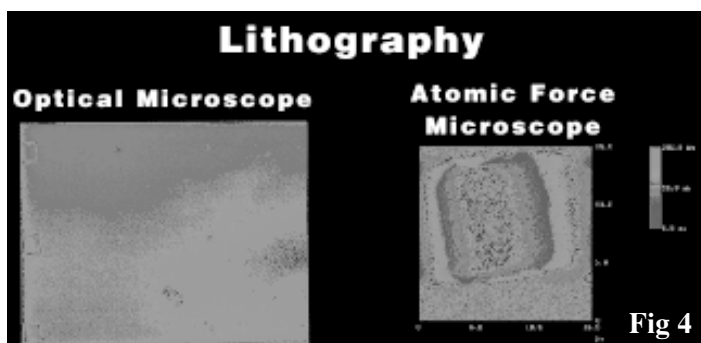
Using the lithography technique, a pattern of pits was etch successfully on the phosphate glass, but the use of these pits to enhance DNA retention has yet not been evaluated.

Acknowledgments:

The University of Puerto Rico in Aguadilla, The Pennsylvania State University, Penn State Nanofabrication Facility, The Life Sciences Consortium, Dr. Carlo G. Pantano and his research group.

References:

- [1] "Separation of Long DNA Molecules in a Microfabricated Entropic Trap Array", J. Han, H.G. Craighead, Science, vol 288, p.1026, 5/00.
- [2] "Versatile Derivatisation of Solid Support Media For Covalent Bonding on DNA Microchips", Bier, M. and Hosheisel, J.D. (1999) Nucleic Acids research 27:1970-1977.
- [3] "General Chemistry", J. H . Hill and R. H. Petrucci. Prentice Hall, Inc. ISBN 0-02-354481-3. (1996)



Mass Spectrometry Analysis of Ubiquitin on Deposited Column/Void Network Silicon Thin Films

REU Intern: Kwanza Nicole Brown, Biology/Pre-medicine, Eastern College

Principal Investigator: Stephen Fonash, Engineering Science, PSU, sfonash@psu.edu

Mentors: Daniel Hayes, Joseph Cuiffi, Engineering Science, PSU, djh195@psu.edu, jdc167@psu.edu

Abstract:

The characterization of proteins is an important application of mass spectrometry. Matrix-assisted laser desorption/ionization (MALDI) and more recently, desorption/ionization on porous silicon (DIOS) have been useful mass spectrometry approaches for protein identification. In this study, we explored the use of a novel arrayed void-column thin crystalline silicon film with nanometer-sized rodlike columns for the characterization of the protein ubiquitin.

Our examination of this new approach presented here included using multiple techniques to digest and process ubiquitin for analysis by desorption/ionization. It is clear from the results to be presented that our films can, in fact, be used for protein identification using mass spectrometry.

Introduction:

As protein characterization becomes increasingly important, it is necessary to find techniques and materials that are more efficient and less expensive. The hope was that our deposited column/void network silicon thin films would fill the need for materials. These films have several advantages over currently employed methods of protein identification by mass spectrometry. The matrix that is required to perform MALDI inhibits the identification of peptides below 500 m/z (mass to charge ratio). Our film has the advantage of not involving the use of any matrix material. Current DIOS techniques involve the wet etching of silicon films which is messy and not practical for mass production [1].

Our films are deposited and etched in one step using electron cyclotron resonance plasma enhanced chemical vapor deposition (ECR-PECVD). Due to the use of the ECR-PECVD, our film can be deposited at much lower temperatures than current DIOS films and therefore can be deposited on a variety of substrates including glass and plastic. Because of these advantages, the possibility of using deposited column/void network silicon thin films was explored.

Procedure:

A PlasmaTherm SLR-770 was used to deposit $\sim 400\text{\AA}$ of Si_3N_4 on 1x3-cm fractions of quartz. This was followed the deposition and etching of $\sim 1500\text{\AA}$ of Si:H. This was performed at 100°C under a process pressure of 8 mTorr. This pressure was used because it seems to produce average film porosity for the pressure range available (5-20 mTorr) [2]. See Figure 1.

Ubiquitin samples were digested using trypsin, endoproteinase Glu-C, and trypsin with sodium dodecylsulfate (SDS). Multiple desalting techniques were applied including the following: evaporation desalting on plate, removal desalting on plate, and column desalting with ziptip. In addition, the effect of time on the results was tested by comparing a 19-day-old digest to a 1-day-old digest. Lastly, end product manipulations were utilized such as: maintaining 100% acetonitrile, transferring end product to deionized water, and adding ammonium citrate. Ammonium citrate was explored because of its apparent benefit to protein analysis with MALDI [3, 4]. Mass spectrometry was performed on each sample to verify the procedure. The following table is a list of expected peptides from a tryptic digest of ubiquitin, a 76-residue protein.

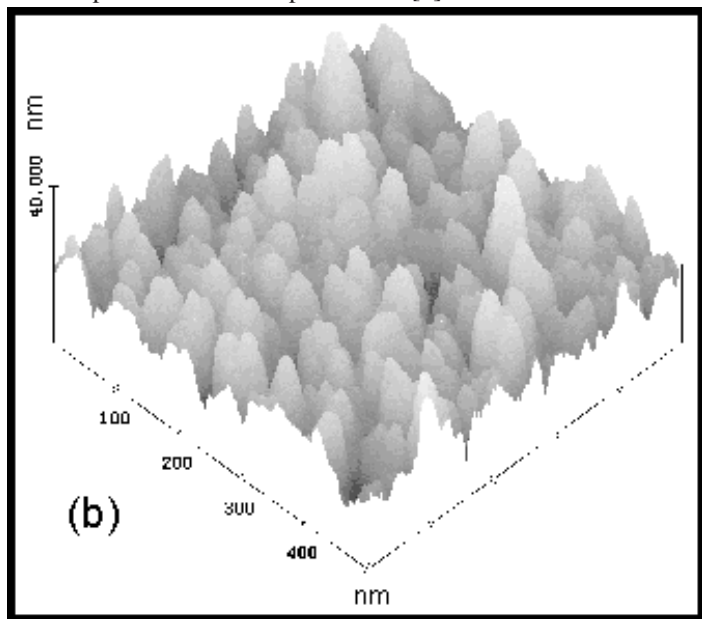


Figure 1: Atomic Force Microscopy image of void-columnar silicon films deposited at 100°C at 8 mTorr.

Table 1.

Expected Results for a Tryptic Digest of Ubiquitin [5]

| Mass | Position | Peptide Sequence |
|----------|----------|------------------|
| 1787.927 | 12-27 | TITLEVEPSDTIENVK |
| 1081.552 | 55-63 | TLSDYNIQK |
| 1067.621 | 64-72 | ESTLHLVLR |
| 1039.517 | 34-42 | EGIPDQQR |
| 765.433 | 1-6 | MQIFVK |
| 717.353 | 49-54 | QLEDGR |
| 648.408 | 43-48 | LIFAGK |
| 519.314 | 7-11 | TLTGK |
| 503.282 | 30-33 | IQDK |
| 288.203 | 73-74 | LR |
| 218.150 | 28-29 | AK |
| 133.061 | 75-76 | GG |

Results and Conclusions:

Many of the mass spectrums only revealed that some part of the procedure was not working. However, as the procedure was fine-tuned, the quantity and quality of the desired peptide peaks increased. To date, ubiquitin digested by trypsin with SDS one day prior to column desalting and transferred to deionized water with a 1:3 ratio of ammonium citrate to end product produces the best results. See Figure 2.

The following peptides were identified: 1787, 1081, 1067, 1039, 765, 717, 648, 503, and 288. It has been proposed that the peptide at positions 12-27 had undergone hydroxylation of the lysine resulting in a peak at 1806 instead of 1787 [6]. It was also proposed that the peak at 1527 was due to an incomplete cleavage between positions 33 and 34.

From the results, it is clear that the characterization of proteins using deposited column/void network silicon thin films is possible. Using our deposited column/void network silicon thin films as a substrate for desorption/ionization mass spectrometry offers a very promising approach to high throughput proteomic analysis.

References:

- [1] Thomas, John J., et. al. Desorption/Ionization on Porous Silicon (DIOS) for Proteomics.
- [2] Kalkan, A. Kaan, et. al. "Nanocrystalline Silicon Thin Films with Arrayed Void-Column Network Deposited by High Density Plasma." Journal of Applied Physics: Volume 88, Number 1. 1 July 2000, p 555-561.
- [3] Asara, John M., and John Allison. Use of Nitrogen-Containing Matrix-Additives in MALDI for Enhanced Detection of Phosphopeptides. Michigan State University. 4 August 2000. http://www.msu.edu/user/massspec/asms98/asara/asara_abs.htm
- [4] Mass Analysis. Protein/Peptide Micro Analytical Laboratory, California Institute of Technology. 4 August 2000. http://www.cco.caltech.edu/~ppmal/sample_prep/mass_spec.html
- [5] Peptide Mass. <http://www.expasy.ch/tools/peptide-mass.html>
- [6] Delta Mass: A Database of Protein Post Translational Modifications. www.abrf.org/ABRF/ResearchCommittees/deltamass/deltamass.html

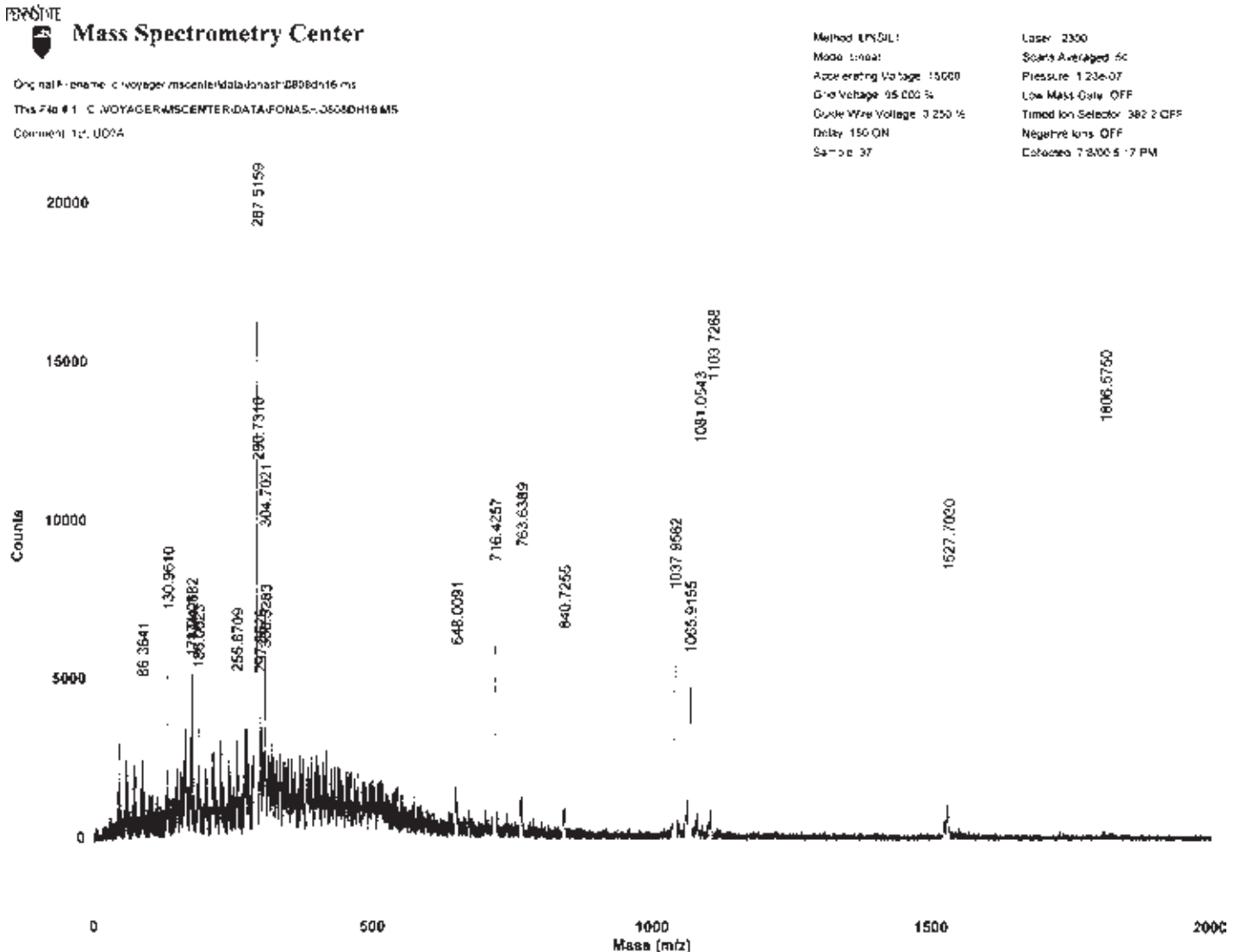


Figure 2: Mass Spectrum of ubiquitin digested with trypsin in SDS, column desalted, with ammonium citrate.

The Absorption Kinetics of des-Pro3,[Ala2,6]-Bradykinin on Deposited Column/Void Network Silicon Thin Films

REU Intern: Nga N. Dinh, Biochemistry, University of Nebraska-Lincoln

Principal Investigator: Stephen J. Fonash, Engineering Science, PSU, sfonash@psu.edu

Mentors: Joseph D. Cuiffi, Daniel J. Hayes, Engineering Science, PSU

Abstract:

The detection and characterization of proteins and molecules is increasingly important with the rapidly developing proteomics field. Several mass spectrometry techniques for biological analysis are commonly used including: secondary ion mass spectrometry (SIMS), electrospray ionization mass spectrometry (ESI-MS), matrix-assisted laser desorption/ionization (MALDI), and more recently, the desorption/ionization on porous silicon (DIOS).

In this study we examined column/void network silicon thin films deposited on glass substrates as DIOS targets, the emphasis of the project included studying the absorption kinetics of a single protein system—des-Pro3,[Ala2,6]-Bradykinin and developing techniques to produce more quantitative results using DIOS.



(No final report was submitted for this project.)



Electrical Properties of TEOS in MIM Structures

REU Intern: William Fadgen, Physics, University of Texas at Dallas

Principal Investigator: David Allara, Chemistry, PSU, dla3@psu.edu

Abstract:

Tetraethoxysilane (TEOS) is a complex molecule with silicon dioxide at its center. When TEOS is hydrolyzed in solution, it forms a precursor of SiO₂. When the solution is spin coated onto a smooth surface, it forms a film which when dry is essentially pure SiO₂. It is possible to prepare films as thin as 1-2 nm in this fashion. The focus of this project has been to fabricate gold-based metal-insulator-metal (MIM) structures to test the electrical properties of nm-thickness SiO₂ films made in this way, and to ascertain whether it is a gate-quality oxide material. Our results show that films with rms roughnesses approaching that of the native oxide on Si can be made on smooth Au surfaces but that these films fail show electrical properties that fall within the accepted range of breakdown voltage and capacitance for a gate-quality oxide.

Introduction:

As interest in increasingly thin gate oxides for use in microelectronics has grown, there has been a corresponding increase in research for ultra-thin gate quality oxide materials. One such material, TEOS, was the focus for this project. TEOS can undergo acid or base-induced hydrolysis to form “sol-gel” SiO₂, so long as the thickness of the oxide does not exceed 100 Å. At a pH of 2-3, the TEOS hydrolyzes and becomes silicon hydroxide. Then as the pH increases beyond that, siloxane bonds become more favorable and as the end result, the “sol-gel” SiO₂ is formed.

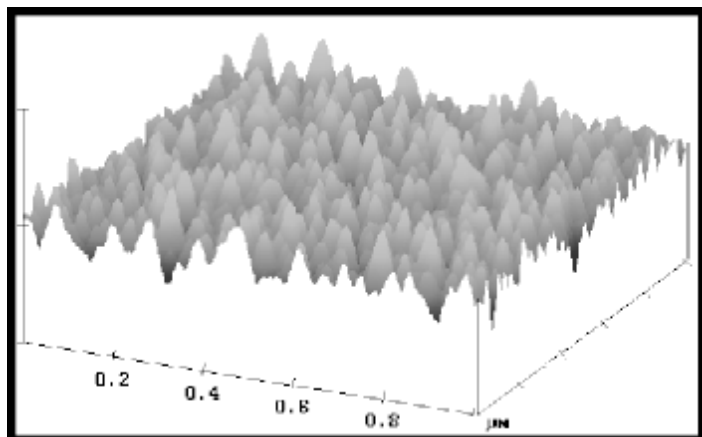
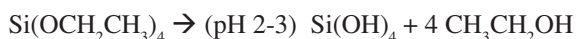


Figure 1

Since the chemical reaction yields an ultra-thin layer of silicon dioxide, it was hoped that the layer would have properties similar to that of normal SiO₂ oxide layers, enabling its application in microelectronics.

Theoretically, TEOS has three major benefits over the standard thermally grown oxide. Since TEOS has a planarizing effect, it reduces the roughness of the surface as can be seen in figures 1 and 2. The average time to deposit a layer of film on to a substrate is 25 minutes and can be prepared at room temperature, thus making the process more efficient than thermally grown oxides which must be prepared over several hours at temperatures upwards of 600°C.

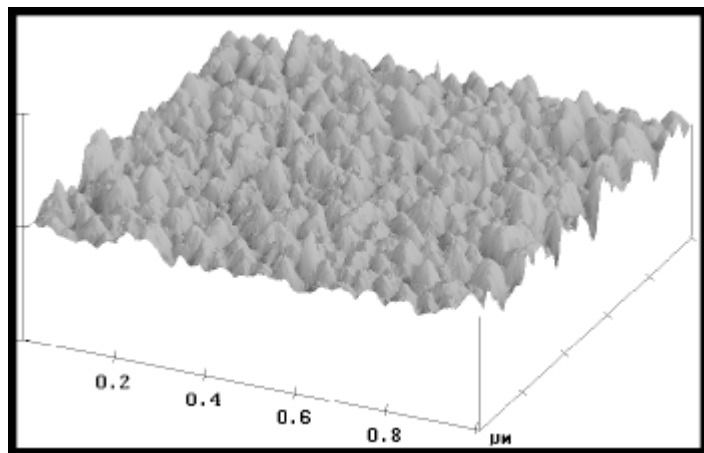


Figure 2

Experimental Procedure:

An undoped Si wafer was scribed and cleaved by hand into several squares approximately 2.5 cm by 2.5 cm. These squares were cleaned using Piranha etch (1 part H₂O₂ 30%, 3 parts H₂SO₄) and ellipsometry was performed to ensure substrate quality. Then 2000 Å of Au was thermally deposited on the samples, with ellipsometry performed again to verify the thickness. Next, it was necessary to create a gold oxide (AuOx) on the surface of the samples via a combination of a UV-ozone machine and H₂O₂. The gold oxide was necessary because as the oxide attracts water to the surface, raising the pH, which in turn makes the siloxane bonds more favorable, generating the ultra-thin layer of “sol-gel” SiO₂.

The TEOS film was deposited with the aid of a spinner spinning at 3600 rpm. This particular speed was chosen because it generated the smoothest films on average. The results of the ellipsometry for the five samples indicated a thickness between 20-50 Å, while AFM images showed a RMS roughness of approximately 7 Å.

A pattern of 80 by 125 μm rectangles on a mask was used. The pattern was deposited on the TEOS film by photolithography. Then 400 \AA of Au was thermally deposited on the pattern. Finally, a lift-off procedure using acetone was performed, leaving the metal-insulator-metal structures.

Results and Conclusion:

There were two measurements performed on the structures, a capacitance measurement and a breakdown voltage test. Both tests failed to measure up to the theoretical values. The capacitance of a gate-quality oxide is typically 92.7 +/- 13.2 pF, while the measured capacitance was approximately 1 pF, as can be seen in figure 3. The breakdown voltage was below the gate oxide value as well.

The acceptable breakdown voltage for a thermally grown oxide is a minimum of 9 MV, while a method such as this is expected to yield a slightly lower value. The measured breakdown voltage was 2.02 +/- .47 MV (figure 4), well below the acceptable value. However, since the voltage was in the mega volt range, the reason for the low value was not due to pin holes but rather due to the properties of the TEOS SiO_2 film itself. Therefore, the fabrication of the MIM structures was successful, but TEOS is not currently an acceptable gate-quality oxide material. It is proposed that the density of the oxide is too low and that further efforts be made to investigate this using spectroscopic ellipsometry.

Acknowledgements:

- Dr. David Allara, PSU, and NNUN for giving me this opportunity.
- Dr. Mark Horn and Dr. Michael Lanagan for all their help.
- Matt Garrett, Tim Tighe, and Sanjay Rangan for their assistance.

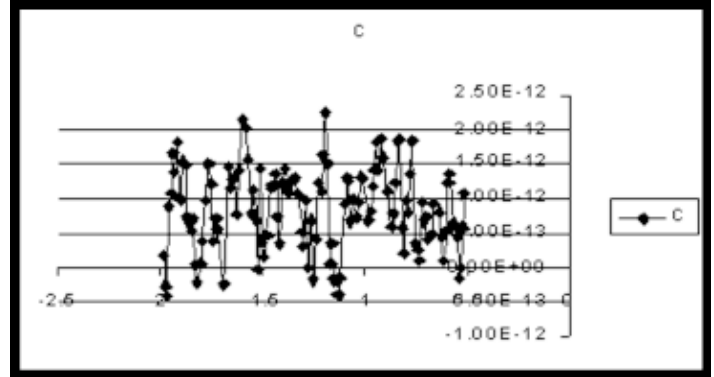


Figure 3. Capacitance as a function of Voltage

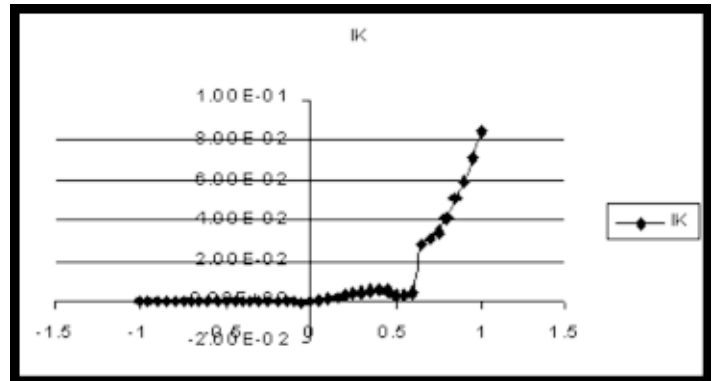


Figure 4. Current as a function of Voltage

Fabrication of Silicon Masters for Micro-Contact Printing

REU Intern: Jevon J. Johnson, Biology, Xavier University of Louisiana

Principal Investigator: Nicholas Winograd, Chemistry, Pennsylvania State University, nxw@psu.edu

Mentors: Amy Walker, Brendan Haynie, Chemistry, Pennsylvania State University

Introduction:

Micro-Contact Printing is a rapidly developing technique for transferring a pattern of molecules onto a substrate, e.g. gold [1]. This technique has a variety of real life applications including the fabrication of molecular-scale electronic devices. In this technique, a polydimethylsiloxane[PDMS] stamp is used which is made from a silicon master to transfer the pattern. The goal of this project was to fabricate a master that is unreactive towards PDMS. To achieve this, we used photolithographic and reactive ion etching techniques to produce masters that had well-defined features and were also inert towards PDMS.

Micro-Contact Printing:

The micro-contact printing process begins with the preparation of silicon masters, which is the focus of this work. Once the master has been created its pattern can then be transferred to the PDMS. After an imprint of the desired pattern, the “stamp,” has been made, we can ink different molecules onto it and deposit them on a substrate. Thus patterns of molecules can be made on a substrate. This is analogous to a child’s toy rubber stamp and ink set with the PDMS being the stamp, the molecules being the ink, and the substrate being the paper.

Experimental Procedure:

The first step in the preparation of the master is photolithography. Photolithography is used to pattern the silicon wafer. We prepared a variety of test patterns including lines, squares, and the words “Penn State” and “PSU”.

We then cleaned the silicon wafer. To do this, the silicon wafer was dried with nitrogen gas and heated at 388K for 120-180 seconds to remove any dust or other particles. Afterwards, we placed the wafer on a spinner and poured 1813 photoresist onto it. The wafer was then spun for 40 seconds at 3000 rpm to produce an even coat of photoresist on the wafer surface. The wafer was heated for a further 90 seconds at 388K and transferred to the photolithography machine.

A mask containing a negative of the desired features was placed on top of the wafer and a UV light was then shone through the mask onto the wafer for approximately 5.5 seconds. The wafer was then removed from the machine and dipped into a 1:1 mixture of 150 ml of MF312 and 150 ml of water for 55 seconds. If the photolithography process had been done correctly, the pattern was visible on the wafer.

The excess photoresist was washed with water and dried with nitrogen gas. To make the pattern more permanent, the wafer was heated for another 90 seconds at 388K.

Once the pattern had been fixed, Reactive Ion Etching (or dry etching) was employed to remove the photoresist layer and to further define the features. The wafer was placed in the Reactive Ion Etching machine via a vacuum lock and the system was pumped down. To etch the wafer, we employed a procedure using CF_4 and O_2 gases because these were determined to be optimal for silicon etching. After the etching process was completed, the system was vented and the wafer removed.

We then used a profilometer to examine the features produced on the wafer. This machine uses a stylus similar to one that you might find on a record player. To measure the surface profile, the stylus was moved across the surface, tracing over the features of the silicon wafer. A computer was used to record the trace data for further analysis.

Results and Conclusions:

In a previous study, it was found that masters made from photoresist-covered silicon wafers did not produce PDMS stamps with well-defined features. This was because the PDMS reacted with the photoresist. Thus we employed Reactive Ion Etching to remove the photoresist.

Using this preparation process, we observed that there was no reaction between the PDMS and the silicon wafer. We also could have also used wet etching to remove the photoresist layer. However, wet etching produces rounded features which are undesirable. This leads to unwell-defined features on the PDMS stamps. Such masters do not produce well-defined features on PDMS stamps at the micron level. On the other hand, dry etching produces square, angular features which give better stamp characteristics.

We also decided to make a master mask using silicon dioxide to determine whether the quality of the features could be improved. We employed the same procedure to make these masters from the silicon dioxide wafer.

From the profilometer data, we observed that the features on the silicon dioxide wafer were not as even or well-defined compared to those on the silicon wafer. We therefore chose to use silicon wafers for the micro-contact printing masters.

Conclusion:

We were able to produce silicon masters with well-defined features. These masters were also inert towards PDMS and thus PDMS stamps could reliably be produced with well-defined features.

Acknowledgments:

The authors wish to acknowledge support and funding from the ONR and NSF. J.J.J. would like to thank the Winograd research team for their help and support.

References:

1. Y.N. Xia, J.A. Rogers, K.E. Paul, G.M. Whitesides, *Chemical Reviews*, 99 1999(1823).

Silver Writing by Laser-Liquid Interaction Technique

REU Intern: Ly Nguyen, Biochemistry, Colorado State University

Principal Investigator: Jogender Singh, MRI, Penn State Nanofabrication Facility, jxs46@psu.edu

Introduction:

Many researches of laser patterning on conducting surfaces such as Al and Cu have done successfully. They are widely used in designation of microelectronic materials. However, laser patterning of Ag on conducting surfaces has not been as successful.

The lower the resistivity of a metal, the better it is in making an electronic device. Silver is a metal that has a low resistivity of $1.6 \mu\text{-ohm-cm}$ [1]. In fact it is the most electrically conductive metal which makes it attractive for use in microelectronic circuits. In this paper, silver deposition on a silicon wafer coated with and without oxide is discussed. Two methods of depositing silver patterns were used to approach the object of this experiment. One was by laser-liquid interaction, and the other was by a conventional method involving silver evaporation, photolithography and etching.

Based on how metal particles are formed, a laser-liquid interaction technique may produce higher conducting silver patterns than the conventional method. According to Dr. Jogender Singh, in the laser-liquid interaction technique, one layer of silver particles goes on top of the previous deposited layer. The particles are well connected which should make current flow through very well. Silver is deposited differently in the evaporator, which is the first step of a conventional method.

First, nucleation of Ag particles forms, then grow out in all directions as well as fill in the channels, and the thickness increases as evaporation keeps going (figure1). The gaps in between the grains increase the resistance of the silver lines.

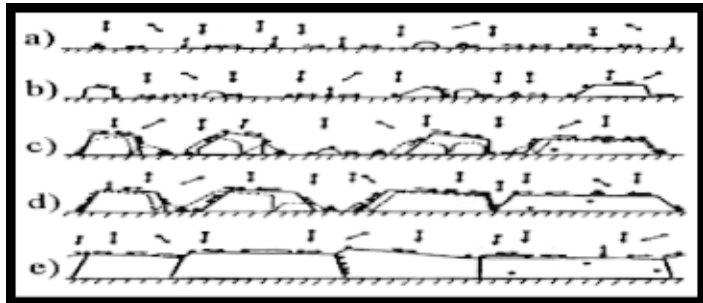


Figure 1. Grain Formation

Materials and Methods:

To deposit Ag by laser, the Si substrate was immersed in a precursor solution with the height of 8mm above the substrate surface (figure 2). The precursor solution contained 40g AgNO_3 , 200ml H_2O , 200ml ethylene glycol, and 40ml diethylene glycol. The solution was irradiated by continuous wave CO_2 with the power of 200 watts. The CO_2 laser beam went back and forth 30 times for each line. The rate was 12 inches per minute. The laser beam shines through the precursor liquid onto the substrate surface,

providing a source of thermal energy to activate localized chemical reaction in solution.

The continuity of the patterns was analyzed using a high resolution SEM. The conventional method required three steps: evaporation of Ag onto SiO_2 wafers at the rate of 6 \AA per second; photolithography; and a wet etch with 50 % of HNO_3 .

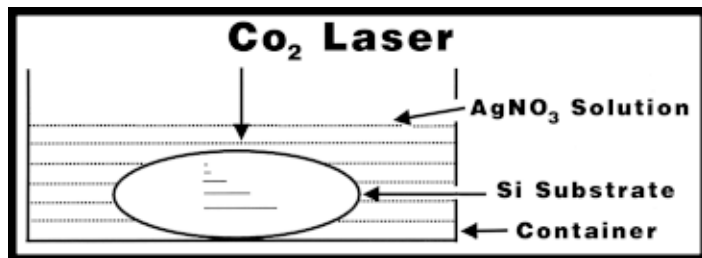


Figure 2. Silver writing by gas CO_2 laser.

Results and Discussion:

The SEM micrographs of Ag on Si and SiO_2 using CO_2 laser at $\lambda = 10 \mu\text{m}$ are shown in figure 3 and 4 respectively. There is good continuity of Ag on the Si substrate, but many gaps are in between the Ag grains on SiO_2 . Resistance of Ag on Si is directly proportional with the length. The resistivity as measured from the graph is nearly $1 \mu\text{-ohm-cm}$ (figure 5), which is lower than the expected value. The discrepancy can be the dimension of the Ag bars. No resistance of Ag on SiO_2 can be obtained. The resistivity of evaporated Ag on SiO_2 turns out to be too low (figure 6).

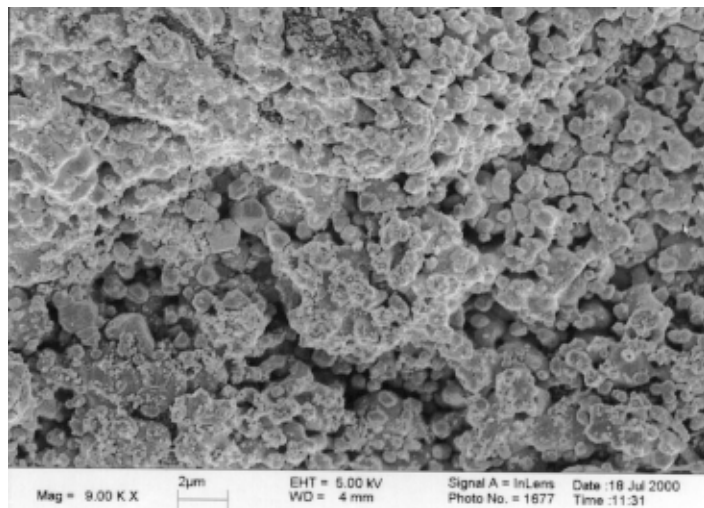


Figure 3. Ag on Si Wafer by Laser

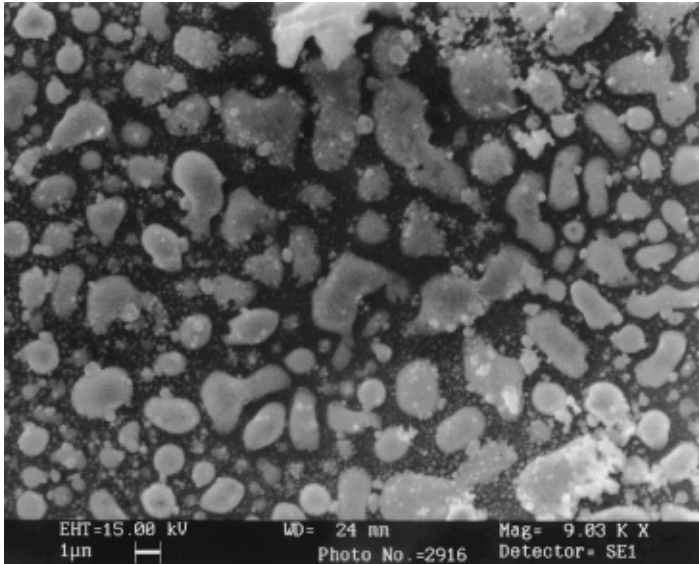


Figure 4. Ag on SiO₂ Wafer by Laser

It is difficult to deposit Ag on SiO₂. Ag molecules do not bond well with O₂. About 40% of the Ag felt away from the SiO₂ surface after a week of deposition. Ag stays on an SiO₂ substrate better when deposited by an evaporator. However, as time goes on, more Ag cracks and peels off the SiO₂ surface. SiO₂ is an insulator that allows electrons from the emission gun of the SEM to block the view of the wafer surface. SiO₂ was exposed where Ag peeled. Therefore, an SEM micrograph could not be taken from this sample.

Due to the limited use of materials, evaporation of Ag on Si could not be prepared in order to measure the resistance and to exam the morphology under SEM. Adhesion of Ag on Si was better than on SiO₂. The rate of Diffusion Coefficient (D₀) onto Si for Ag is 2x10³, which is close to the D₀ of Au. Au was seen to diffuse slowly into the Si surface. This suggests that Ag was partially diffused to Si. The experiment results support this suggestion.

In summary, resistance of Ag deposited on SiO₂ by laser could not be measured, so it was not compared with the sample prepared by conventional method; and there was no sample of deposited Ag on Si by conventional method to compare with the sample made by laser technique.

Based on the collected data, what could be compared was the morphology of Ag on Si and SiO₂. Both were deposited by gas CO₂ laser beam. Furthermore, in a perfect world, it would take only 3.1 minutes to write the five Ag patterns by laser while the conventional method would take approximately 3 hours.

Conclusion:

Data collected was not enough to compare the resistance of Ag deposited on Si and SiO₂ by the conventional method and by laser-liquid interaction. However, no doubt that Ag writing by laser-liquid interaction technique is cost effective and time-saving compare to the conventional printing.

Acknowledgements:

I would like to express my gratitude to Dr. Jogender Singh, Penn State Nanofabrication Staff, and the NNUN REU program.

Reference:

- Johnson, Zack. Resistivity at 20o C. <http://bvsvd.k12.co.us/schools/BHS/scienc...sics/reference/measured/resistivity.html>

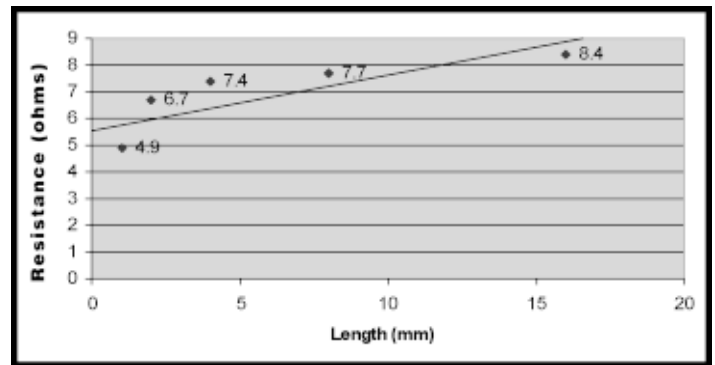


Figure 6. Resistance of Ag on SO₂ Wafer Using Conventional Method.

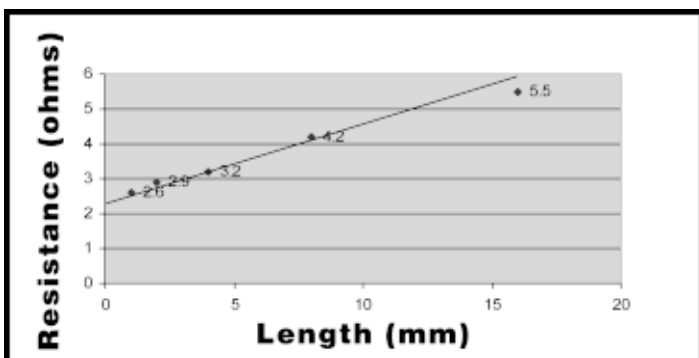


Figure 5. Resistance of Ag on Si Wafer by Laser. Resistivity measured from the graph is 1 µ-ohm-cm

this page has intentionally been left blank

Stanford Nanofabrication Facility 2000 REU Participants



REU Intern

School Affiliation

Principal Investigator

Front Row:

| | | |
|---------------------------------|-----------------------------------|-----------------------------|
| Mr. Van Ortega Cayetano | New York University | Kathryn Moler |
| Mr. Erik Douglas | Purdue University | Mary Tang |
| Mr. Luis Jose Cruz-Rivera | Prairie View A&M University | Fabian Pease |
| Ms. Andrea Tao | Harvard University | James Harris, Glenn Solomon |
| Ms. Karen Ahle | Harvey Mudd College | James Harris |
| Mr. Eric Taketatsu | University of Hawaii Manoa | Kathryn Moler |

Back Row:

| | | |
|-------------------------------|--|--------------------------------|
| Mr. Michael Deal | SNF | SNF REU Coordinator |
| Mr. Aghapi Mordovanaki | University of MI Dearborn | James McVittie |
| Mr. James Ryan Williams | Santa Clara University | James McVittie |
| Mr. Corey Harris | Washington University (St Louis) | Yayoi Takamura |
| Ms. Anna Asanbaeva | UCLA | Mary Tang |
| Mr. Scott Harrison | Rice University | Peter Griffin |
| Mr. Jesse Hwang | Yale University | Bruce Clemens, Christine Esber |

Molecular Beam Epitaxy of Nanostructures

REU Intern: Karen Ahle, General Engineering, Harvey Mudd College

Principal Investigator: James Harris, Electrical Engr, Stanford University, harris@snow.stanford.edu

Mentor: Thierry Pinguet, Applied Physics, Stanford University, pinguet@snow.stanford.edu

Fabrication and Loss Measurements of Optical Waveguides in AlGaAs:

All-optical wavelength conversion using nonlinear optics is very desirable to increase speed in optical communication networks. This project aims to fabricate very low loss AlGaAs waveguides to convert signals from one wavelength channel to the next in the 1.55 μm region. 3 μm wide rib waveguides were created using molecular beam epitaxy, photolithography, and wet etching processes. Losses in the resulting waveguides were measured using Fabry-Perot interferometry and throughput measurements, which yielded results of 10-20 dB/cm. Future work will attempt to reduce these losses through improvements in the lithography and etching processes.

Introduction:

One of the most pressing needs in the telecommunications industry is increasing the bandwidth over a fiber optics connection. The primary way of doing this is to send signals over many different wavelengths (channels) at once, in the 1.55 μm band used for telecommunications. This procedure is called Wavelength Division Multiplexing, or WDM. A major problem with using WDM is the need to convert data from one channel to another. Currently this is done using electronic switching — the optical signal is converted to an electrical signal, and then converted back to an optical signal in the desired wavelength. This process slows communication (since electrical signals travel much more slowly than optical ones), and requires large amounts of power. The goal of this project is to create an all-optical solution, which will convert one channel to another without the need for an electronic intermediary. This is done using a nonlinear optical waveguide, which converts the signal using difference frequency generation (DFG) [Figure 1].

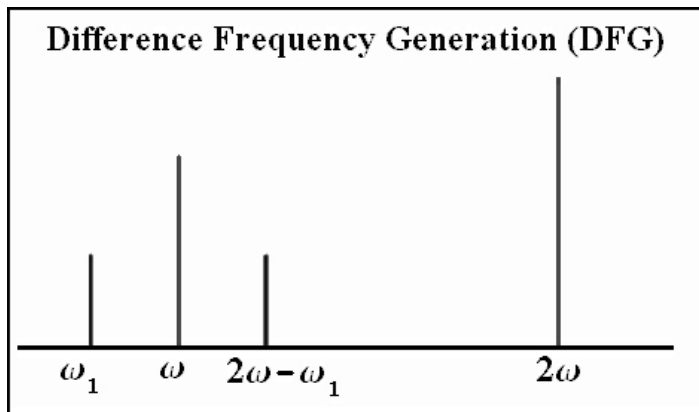


Figure 1. Difference Frequency Generation.

Background:

Difference frequency generation is a process that works by generating an output signal with a frequency equal to the difference of the two input frequencies. This can be used to switch data from one channel to another, as shown above.

To move a signal at frequency ω_1 from a channel with a longer wavelength than the 1.55 μm band (with frequency ω) to a channel with a shorter wavelength than 1.55 μm , DFG is used. The input signal is combined in the waveguide with a beam with precisely double the frequency of the 1.55 μm band (with a wavelength of 0.775 μm .)

This interaction results in an output beam with a frequency equal to the difference between the two incident beams: $\omega_{\text{out}} = 2\omega - \omega_1$. This has the effect of converting the input signal to a shorter wavelength channel.

The low power of telecommunications signals requires a very high efficiency, which is only possible in a waveguide configuration. DFG waveguides have already been fabricated in lithium niobate [1]; unfortunately lithium niobate has a low second-order nonlinearity, which limits the efficiency of these devices. AlGaAs is an excellent candidate for DFG, as it has a high second-order nonlinearity, is a developed technology with existing fabrication processes, and is also transparent in both the 1.55 μm and 0.775 μm bands [2].

Procedure:

We followed Reference 3 for the fabrication of our waveguides. An $\text{Al}_{0.5}\text{Ga}_{0.5}\text{As}$ core was grown with $\text{Al}_{0.6}\text{Ga}_{0.4}\text{As}$ cladding on a GaAs wafer using MBE [Figure 2]. Figure 3 is a model of the electric field in the waveguide; it shows that the majority of the light is in fact confined.

The sample was then patterned with stripes using photolithography, then underwent oxide removal in a

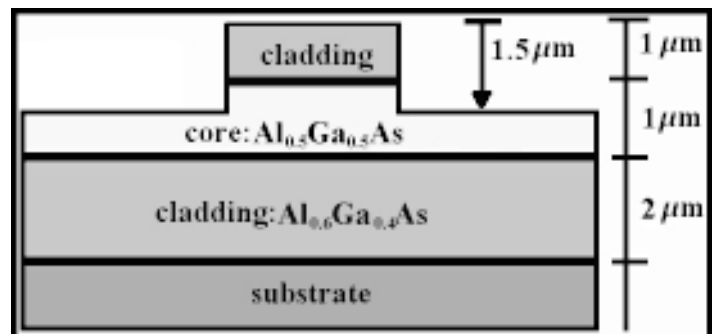


Figure 2. Schematic of the AlGaAs waveguide.

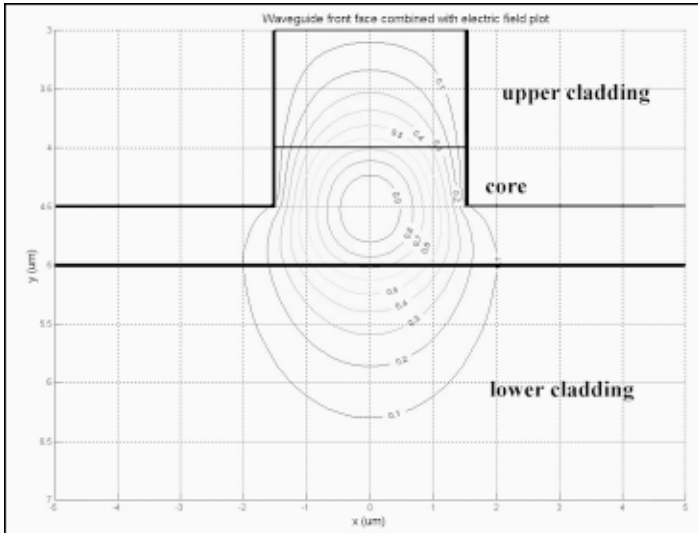
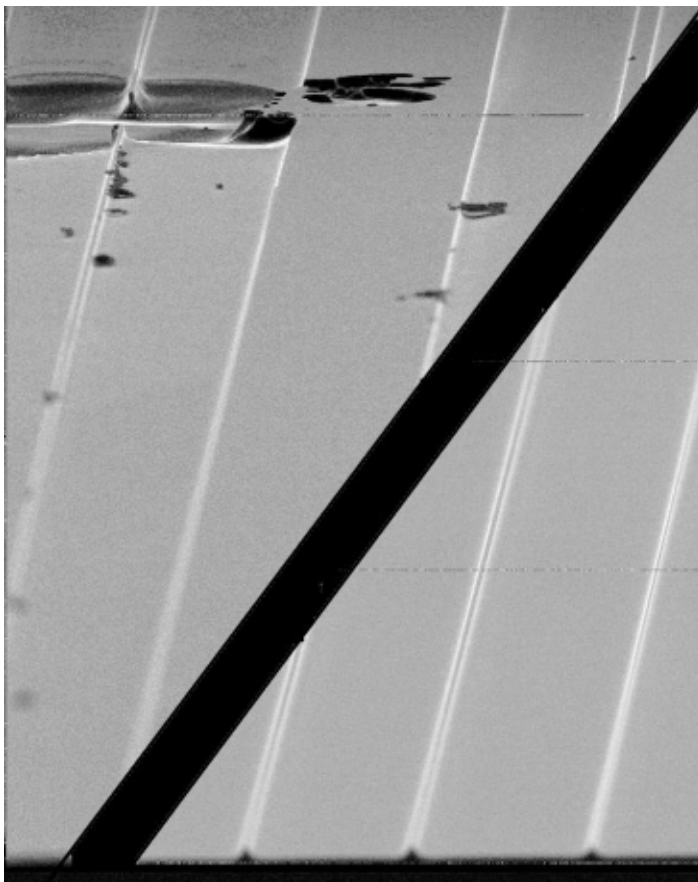


Figure 3. Model of the TE mode for $\lambda = 1.55 \mu\text{m}$.

6:1 $\text{H}_2\text{O}:\text{NH}_4\text{OH}$ solution for 30 seconds, followed by diffusion-limited etching in an 80:4:1 $\text{HCl}:\text{H}_2\text{O}_2:\text{H}_2\text{O}$ solution for 9 minutes.

This process resulted in poor waveguides — bubbling in the etchant resulted in numerous small pits across the surface of the sample. This was corrected using a dummy wafer; a 2" plain GaAs wafer was placed under the sample in the etchant solution. This caused the majority of the bubbles to form on the dummy wafer, and left the sample relatively pit-free.

The contrast between the sample etched without the dummy wafer and with the dummy can be seen in Figure 4.



However, this method will need changing for larger-scale production of waveguides (particularly fabrication of entire 2" wafers of waveguides), possibly by using larger dummy wafers.

Results and Conclusions:

Loss was measured in the waveguides using both throughput measurements and Fabry-Perot interferometry [Figure 5]. The sample was cleaved into a piece 5mm long by 1cm wide. Throughput measurements were performed on the sample, however for confirmation, more accurate measurements were then done with Fabry-Perot interferometry, with results of losses of 10-20 dB/cm.

These are only preliminary results, as Fabry-Perot interferometry has only been performed on two samples due to time constraints. However, the results we obtained are within the expected range, as the lithography and etching processes have not yet been refined. Future work would involve fabrication of 2" wafers of waveguides, and reduction of losses to the 1-4 dB/cm range.

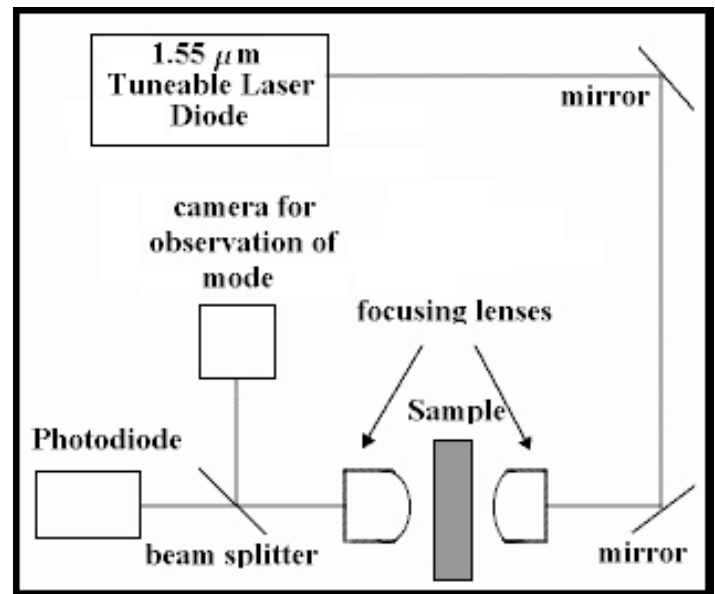


Figure 5. Setup for loss measurements.

References:

1. M. H. Chou, K. R. Parameswaran, and M. M. Fejer, *Opt. Lett.* 24, 1157 (1999).
2. C. B. Ebert, "Quasi-phases-matched waveguides for infrared nonlinear optics using GaAs/Ge/GaAs heteroepitaxy," Ph.D. dissertation (Stanford University, Stanford, Calif., 1998).
3. S. J. B. Yoo, R. Bhat, C. Caneau, and M. A. Koza, *Appl. Phys. Lett.* 66, 3410 (1995).

Figure 4, left. SEM pictures of samples etched both with and without dummy wafers.

Electrical Conductivity in Oriented DNA

REU Intern: Anna Asanbaeva, Chemical Engineering, University of California at Los Angeles

Principal Investigator: Mary Tang, Electrical Engineering, Stanford University, mtang@snf.stanford.edu

Abstract:

DNA molecules were attached, extended and aligned between gold electrodes in a process of “dynamic molecular combing.” This approach uses the hydrodynamic force of a receding meniscus of a drying film to deposit immobilized strands of DNA on silanized glass. Aligned DNA molecules demonstrated ohmic relationship between current and applied voltage (up to 0.1V), however recent experiments have made it unclear whether DNA was the medium for charge transfer.

Introduction:

DNA has a long rod-like duplex structure with stacked base pairs rich in π -electron clouds. This arrangement appears to be a good candidate for one-dimensional conduction. Charge mobility in DNA has enormous implications on a wide variety of areas—ranging from biological control mechanisms such as understanding mechanisms of mutagenesis, carcinogenesis, and DNA repair to the development of novel nanoelectronic materials where DNA can act as a wire in molecular electric circuits. Other DNA conductivity studies have shown conductivity in DNA using intercalators to act as electron donor and acceptor, or tested DNA conductivity in a matrix or film. Our experiment was targeted at testing conductive properties of bulk DNA by making direct measurements of electrical current transport as a function of applied voltage, in the form of an IV curve. This is a unique experiment because direct measurements of bulk DNA, rather than DNA in a matrix, have not been done before.

Procedure:

Fabrication and Design of Electrodes:

Au electrodes were lithographically fabricated on glass and consisted of interlocked electrode combs where voltage will be applied in the pad area. (Fig 1)

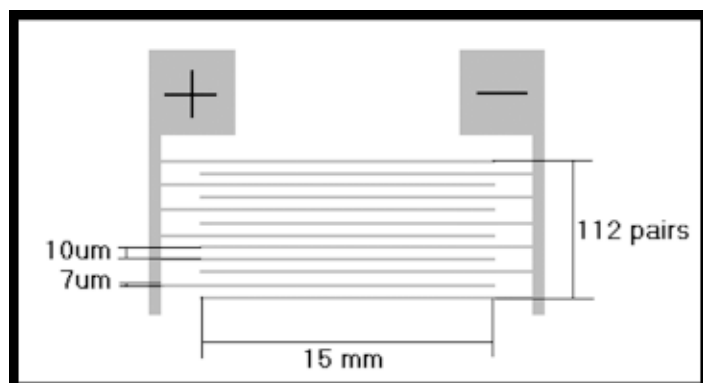


Figure 1. A schematic representation of electrode design. Spacing of $7\mu\text{m}$ between the $10\mu\text{m}$ wide electrodes is shown.

DNA would be dynamically combed perpendicular to the electrode combs to provide contact between oppositely biased electrodes.

Preparation of Octadecyltrichlorosilane Covered Surface:

Electrodes on glass surfaces are cleaned in one-third hydrogen peroxide (30%), two-thirds sulfuric acid (96%), rinsed with water, and dried by heating. When clean, the surface is immersed in 2% solution of octadecyltrichlorosilane ($\text{CH}_3 - (\text{CH}_2)_7 - \text{SiCl}_3$) in toluene for 30 min., then removed, rinsed with toluene, blow dried, and stored at room temperature until used.

Preparation and Staining of DNA Solution:

To visualize DNA with a fluorescent microscope $1.43\mu\text{g}/\text{ml}$ λ DNA (Life Technologies) in 50mM MES (pH 5.5) was stained with YO-PRO1 in a 1:15 ratio [base pairs per dye (YO-PRO1) molecule (Molecular Probes, Eugene, OR)].

Dynamic Molecular Combing:

This approach is a modified phenomenon of molecular combing [1, 2]. In dynamic molecular combing process [3], silanized glass surface is dipped into a buffered DNA solution and, after 5 min of incubation, is pulled out slowly with a mechanical device at a constant vertical speed of $100\mu\text{m}/\text{s}$ (Figure 2). Combed molecules are observed by video enhanced fluorescence microscopy.

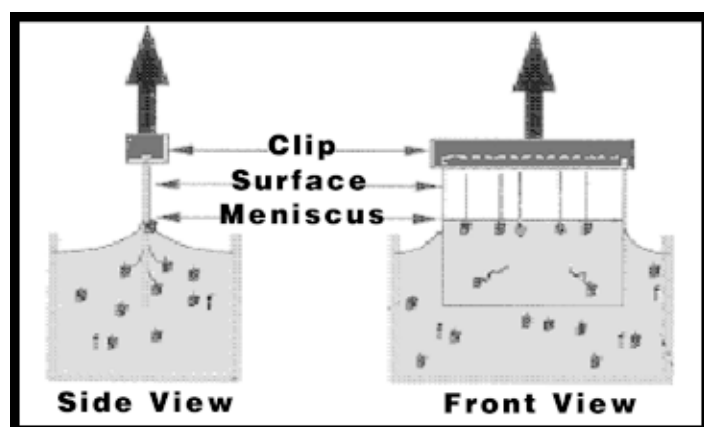


Figure 2: Adapted from [3]. Freely floating molecules bind to the surface by their extremities [1-3], while the rest of the molecule remains unattached in a random coil conformation. When the glass is pulled out of the solution at a constant vertical speed, the meniscus exerts a constant and downward vertical force on the coil of the immersed molecules, which is progressively unwound. The unwound part is stretched and irreversibly fixed on the dry part of the surface, being aligned in a single direction perpendicular to the horizontal meniscus.

Electrical Measurements of Combed DNA:

Electrical current transport through DNA film was characterized as a function of applied voltage using a Hewlett Packard 4156A Precision Semiconductor Parameter Analyzer.

Results and Conclusions:

λ DNA has single-stranded regions that expose the bases on both of its extremities, also referred to as “sticky” ends. Aromaticity of DNA bases causes these single-stranded regions to be very hydrophobic and to adhere to hydrophobic surfaces such as octadecyltrichlorosilane coated glass. The hydrophobic interactions between the “sticky” ends of λ DNA and octadecyltrichlorosilane coating are responsible for attachment of DNA to the surface during the incubation period in dynamic molecular combing. To verify the alignment of DNA molecules in the glass surface after combing, fluorescence microscopy was used. A fluorescence microscope image of combed λ DNA molecules on silanized glass surface is shown below in Figure 3.

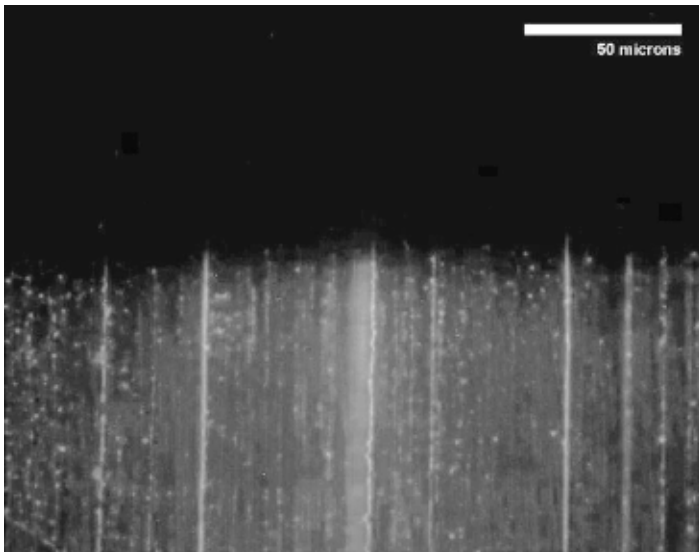


Figure 3. One field of view ($210\ \mu\text{m}$ by $175\ \mu\text{m}$) of combed λ DNA observed with Nikon Eclipse E800 (40x objective) fluorescence microscope. The black area of the image is a part of the glass surface that remained above the meniscus during the incubation. The bottom half of the image is the combed area. The interface between the two areas represents the position of the meniscus during incubation. The DNA is shown to be aligned in the direction of the receding meniscus. The difference in fluorescence intensity is due to local binding of a few DNA molecules. Images were contrast enhanced with Adobe Photoshop.

Linearized DNA demonstrated ohmic current (10-60 pA) that increased linearly with increased applied voltage, up to 0.1V (Figure 4). On the contrary, when measurements were taken before combing, electric current was hardly observed even at a voltage of 0.1V (less than -10pA). These results suggest that electric currents may pass through stacked base pairs of the aligned DNA.

Recent experiments, however, introduced some uncertainty into what was the medium for charge transfer in our setup.

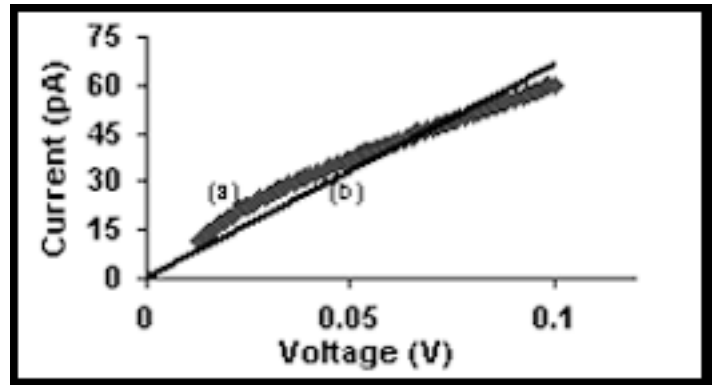


Figure 4. (a) Current in aligned DNA as a function of applied voltage. (b) Ideal Ohmic relationship between current and voltage. No data was collected below 10pA, due to insensitivity of the equipment.

After DNA had been stripped off the surface with a high concentration of salt, the current was measured again. The result demonstrated a perfect ohmic relationship with a maximum of 80pA at 0.1V, which is a larger current than measured right after combing. To clean the surface of all possible contaminants, it was treated with the hydrogen peroxide-sulfuric acid mixture described above. This completely destroyed the electrode combs making it impossible to get another measurement. More work will need to be done before it can be concluded that electric currents pass through stacked base pairs of the aligned DNA. More functional devices will have to be generated to repeat the first result and to prove its consistency.

Dynamic molecular combing demonstrates that DNA can be aligned, allowing us to take DNA conductivity measurements. This is a simple and easy procedure that can be used to answer the question of whether charge is able to migrate across the DNA helix.

Acknowledgements:

I would like to thank Mary Tang and Thorsten Nasjedal for their advice and guidance throughout the summer; Lance Kam for assistance with the fluorescence microscope; Mahnaz Mansourpour and the rest of SNF staff for providing excellent training; NNUN and NSF for providing funding. Also, thanks to Mike Deal, Jane Edwards and my fellow SNF REUers who made this a great experience.

References:

- (1) J.-F. Allemand, D. Bensimon, L. Jullien, A. Bensimon, and V. Croquette, *Biophys. J.* Vol. 73: 2064-2070, 1997.
- (2) A. Bensimon, A. Simon, A. Chiffaudel, V. Croquette, F. Heslot, and D. Bensimon, *Science*, Vol. 265, pp. 2096-2098, 1994.
- (3) X. Michalet, R. Ekong, F. Fougereousse, S. Rousseaux, C. Schurra, N. Hornigold, M. von Slegtenhorst, J. Wolfe, S. Povey, J. Beckmann, and A. Bensimon *Science*, Vol. 277, pp. 1518-1523, 1997.
- (4) Y. Okahata, T. Kobayashi, H. Nakayama, and K. Takanaka, *Supramol. Sci.*, Vol. 5, pp. 317-320, 1998.

Novel Carbon Nanotube Tips: En Route to High Resolution and Ultra Sensitive Force Detection in Magnetic Force Microscopy

REU Intern: Van Ortega Cayetano, Chem & Chem Engr, New York Univ. and Stevens Inst of Tech

Principal Investigator: Kathryn A. Moler, Applied Physics, Stanford University, kmoler@stanford.edu

Mentor: Eric W. J. Straver, Dept. of Applied Physics, Stanford University, estraver@stanford.edu

Abstract:

Magnetic Force Microscopy (MFM) is limited by the resolution and sensitivity of the scanning probe tips. By equipping cantilevers with ultra small magnetic tips, resolution and sensitivity may improve for MFM. We have positioned MWNTs onto silicon cantilevers and have oxidized MWNTs for the purpose of attaching ferromagnetic cobalt nanoparticles ($d = 6$ to 9nm) to their ends. By utilizing this cobalt-MWNT assembly as a high definition tip for a scanning probe, the development of magnetic force microscopy with definitive precision, resolution, and sensitivity is foreseen, and practical analysis of magnetic vortices is conceivable.

Introduction:

Magnetic Force Microscopy is a variation of Atomic Force Microscopy. The components of a deflection sensor, cantilever, and tip are similar. However, in the case of MFM, the cantilever tip is magnetized. As the probe is scanned across a magnetic sample, the variations in force gradients due to the probe-sample interactions produces an image. Curvature radii of MFM tips range from 50 to 60nm , limiting resolution to this standard. Recently, however, lateral resolution of AFM has been improved greatly by attaching MWNTs onto probe tips [1]. Thus, an assembly such as that used for AFM, may be adapted to improve MFM resolution.

The scheme to achieve this assembly consists of first, attaching a MWNT strand to the tip of a single-crystal silicon cantilever; and second, attaching magnetically characterized cobalt nanoparticles to the MWNT end — satisfying the magnetic property of MFM. Initially, though, each step of the process must be experimented with and analyzed in order to accomplish the final assembly.

Experimental Procedure:

Attaching Multi-Walled Nanotubes onto Cantilevers:

The procedure for attaching nanotubes to commercial cantilever tips was developed by the Center for Nanoscale Science and Technology at Rice University [2].

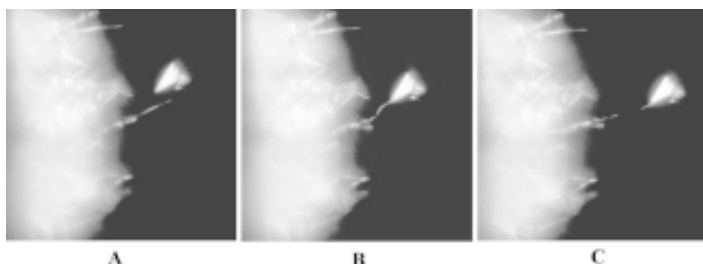


Figure 1. Optical images of the cantilever tip (a) tagging a strand from a bundle of nanotubes, (b) loosening the strand from the bundle, and (c) pulling away the nanotube strand.

Initially, cantilever tips are coated with adhesive. Using two X-Y-Z micrometer translation stages (one containing a cantilever and one containing a bundle of nanotubes), nanotubes are manually mounted onto cantilever tips.

Once the MWNT is attached to the cantilever tip, imaging under a Scanning Electron Microscope (SEM) is necessary to characterize the orientation and position of the nanotube on the tip.

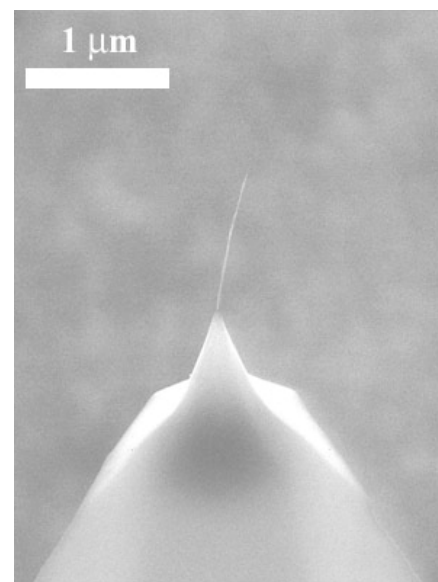
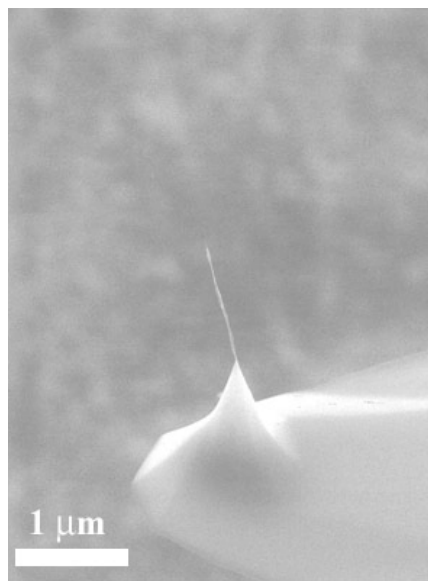


Figure 2. SEM images of one of the samples produced from the mounting procedure.

Preparing Multi-Walled Nanotubes:

The cobalt nanoparticles have a stearic acid coating and are suspended in a hexane solution to inhibit clustering. To utilize the particles, either reduction or substitution of the acid coating is necessary. Therefore, by functionalizing MWNT ends through oxidation, carboxylic acid end groups would substitute the stearic acid coating and lead to the attachment of cobalt nanoparticles to MWNTs. Preparation of oxidized nanotubes was fulfilled by a 3-hour reflux of MWNT material in a 3:1 (by volume) mixture of concentrated $H_2SO_4:HNO_3$ [3]. The MWNT material was repeatedly rinsed with distilled water, centrifuged, and decanted until the rinse water maintained a pH~7.

Attaching Cobalt Nanoparticles to Multi-Walled Nanotube Ends:

Once isolated, the oxidized nanotubes are re-suspended in hexane. A supernatant solution of cobalt nanoparticles in hexane is diluted and added drop-wise to a solution of oxidized nanotubes in hexane. To establish the attachment between the particles and the nanotubes, a sample of the resulting solution is deposited on an amorphous carbon coated copper grid for Transmission Electron Microscope (TEM) analysis.

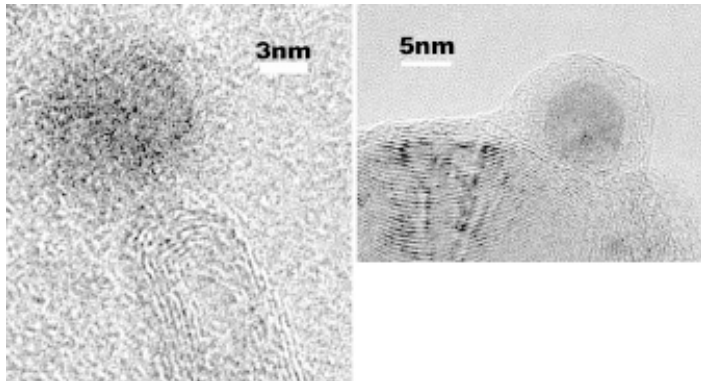


Figure 3. TEM images of two different samples of cobalt nanoparticles attached to functionalized nanotube ends.

Results and Conclusions:

The SEM images in Figure 2 show views of a MWNT-cantilever sample prepared under the micromanipulation procedure. Evidently, a relatively long MWNT strand was attached to the cantilever tip. The length of the MWNT leaves it prone to buckling under Scanning Force Microscope (SFM) application. Close analysis under the SEM, however, shows that the nanotube strand extends along the base, providing a strong support for the tip — a combination of van der Waals forces and adhesion forces may be responsible for this.

Figure 3 presents TEM images of two MWNT-cobalt samples. The “ball” object is the cobalt nanoparticle and the coating surrounding it is the stearic acid. The image on the right demonstrates that wherever the “concentric shelled” nanotube touches the cobalt nanoparticle the stearic acid is displaced. Presumably, the cobalt is attached to the oxidized nanotube in such a manner.

Each step of this process is manageable. However, final construction of the intended assembly did not occur due to time limitations. Further work will be done in order to optimize the Cobalt-MWNT-cantilever assembly and achieve a nano-magnetic mechanical system with high resolution. Ultimately, by attaching such an assembly to an ultra thin cantilever, high resolution may be combined with attonewton force detection to fabricate the paramount probe assembly for Magnetic Force Microscopy.

References:

- [1] H. Dai, Nature 384, 147-151 (1996).
- [2] For a more detailed description of this procedure, go to <http://cnst.rice.edu/mount.html>
- [3] R. E. Smalley, Science 280, 1253-1256 (1998).

Acknowledgements:

The authors wish to thank H. Dai and T. Tomblor of Stanford University for cantilever and MWNT samples, A. Marshall of Stanford University for TEM imaging, M. G. Bawendi of M.I.T. for Co nanoparticle samples, and the NSF, the NNUN, and the Air Force Office of Scientific Research for financial support.

High Resolution Imaging with a Uniform Axial Magnetic Field

REU Intern: Luis J. Cruz-Rivera, Electrical Engineering, Prairie View A&M University

Principal Investigator: R. Fabian Pease, Electrical Engr, Stanford University, pease@ee.stanford.edu

Abstract:

Automated wafer inspection systems are widely used in semiconductor manufacturing. Fast, high resolution inspection tools are needed as device features reach sub-micron dimensions. Electron beam inspection systems have become a critical component in process development of these small devices, but have yet to penetrate the inline inspection market. This is because of their relatively slow throughput. The throughput could be greatly enhanced if multiple beams were used.

Our approach is to use a highly parallel multi-axis system of distributed electron beamlets. The imaging is performed with a uniform magnetic field. However, high resolution imaging with a uniform field has yet to be demonstrated.

As a first step toward the multi-beam system, we have designed and constructed an apparatus to examine the imaging properties of a single beam. The knowledge gathered from the single beam experiment will greatly facilitate future work on the multi-beam system. The apparatus is still being constructed, and results are forthcoming — the first images being expected by late fall.

Introduction:

While electron tools, both lithographic and inspection, have become invaluable in developing smaller novel devices given their superior resolution, they have not been integrated into inline semiconductor processes for several reasons. The primary problem with this technology is its poor throughput [1]. Many schemes have been proposed to solve this problem [2, 3, 4].

Pickard *et al* and Groves *et al* have proposed a system that can increase throughput dramatically by having a massively parallel e-beam system. Such a system will have an array of beamlets focused by a common highly uniform magnetic field (figure 1).

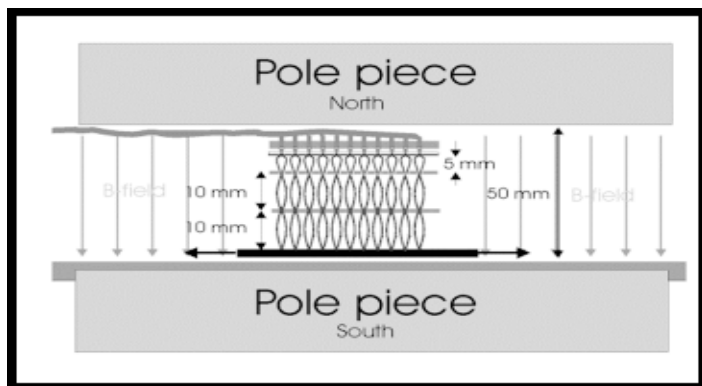


Figure 1. Diagram of distributed axis system as proposed by Pickard *et al* and Groves *et al*. Here a photocathode is the primary source illuminated by fiber-optical array.

Coulombic interactions are minimized by the separation of the beams, so high resolution is possible by scaling the source into the nanometer range. This proposed system will have an array of apertures that will define the size and spacing of the beams produced from a photo cathode used as a primary source. Even though this system was conceptualized to be a lithography tool, by large scale parallel data acquisition, this system could be used for inspection and the images could be utilized as beam diagnostics to minimize aberrations due to tilt and misalignment in the system.

The focus of this work was to design an experimental apparatus to prove the experimental principles behind high resolution unity magnification imaging in a highly uniform magnetic field with one beamlet.

Experimental Setup:

The experimental apparatus uses a large H-frame magnet with 250 mm pole pieces. A magnetic field of 0.3 Tesla with a field homogeneity of better than 10 parts per million over a cylindrical area of 3 cm was utilized to propagate a very stable field within a pole gap of 120 mm. A custom design UHV stainless steel vacuum vessel, as seen in figure 2, is positioned between the pole pieces and contains all of the electron optical components (figure 3).

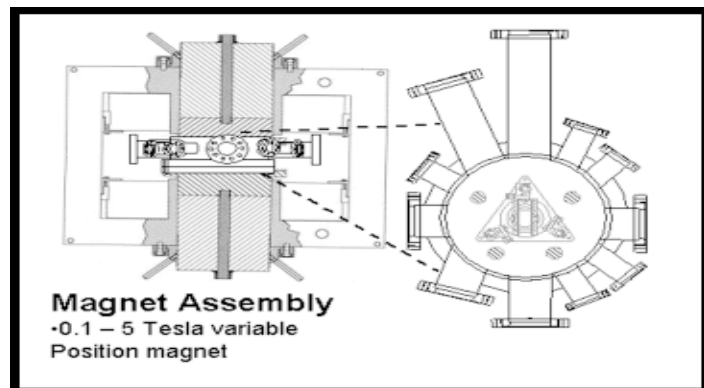


Figure 2. A stainless steel chamber is placed within the magnet assembly. Connected to the chamber ports are the stage controllers, electrical interconnections, and a parallel vacuum scheme.

Within the volume of high magnetic field uniformity, the chamber houses a LaB6 cathode gun which is used as the primary electron source, a secondary electron source is formed with a 50 nm aperture (manufactured with a Focused Ion Beam). The aperture plate is located on a stage assembly that is controllable in horizontal plane. On this base plate, which houses the workpiece holder, three linear inchworm motors control the z direction and tilt of the second

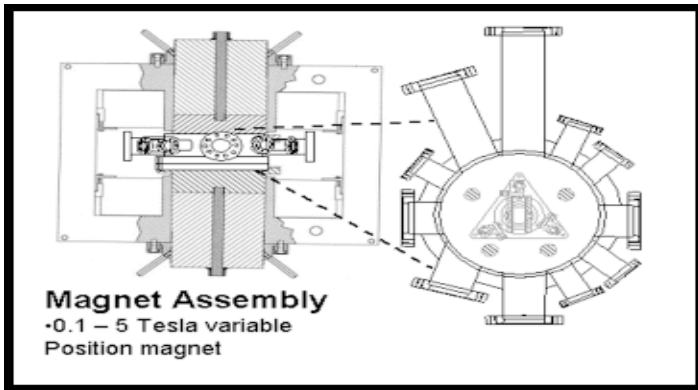


Figure 3. Here are SEM images of the apertures used as secondary sources. In the bottom center is a cross-section of the aperture plate, which is etched to 150 nm of bottom surface of wafer (as seen on far right image). A cross-section of the aperture is seen in middle top and a aerial view on the far left.

stage of this apparatus. This stage has 3 pivot points providing all degrees of freedom to this stage so the aperture plate and an octopole assembly, which is used to deflect and form the beam can be precisely controlled (Figure 4). It is important to note that the size of the aperture determines the ultimate resolution of the system.

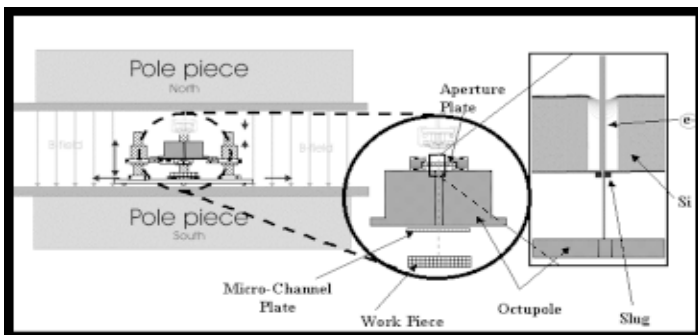


Figure 4. Experimental apparatus, as placed in magnetic field (left side). As e-beam passes through aperture (right side) it can be deflected by the octopole onto the workpiece.

Once secondary electrons are propagated from the surface of the workpiece, they are detected with a Hamamatsu microchannel plate, similar to existing SEM devices. The MCP accelerates the secondary electrons to be detected outside the chamber electrically.

Conclusions and Future Work:

Once alignment of aperture plate and source is completed, imaging can be performed in this single beam apparatus, verifying the secondary source concept and functionality while providing the hardware and software configuration validation. Given functional verification of principles, there is great confidence that the primary system proposed can be constructed. Further development in primary source and source excitation needs to be addressed and the verification of theoretical negligibility of multiple beam interactions at various current densities has to be studied amongst other things. Initial imaging results from proposed system are expected before the end of this fall.

References:

- 1) J. Jau, H. Dohse, A. Brodie, and D. Meisburger, Proc. SPIE 2439, 174 (1995).
- 2) D.O. Smith, K. J.Harte, JVST B 19,4 953 (1981).
- 3) N. Heynick, E. R. Westerberg, C. C. Hartelius, R. E. Lee, IEEE Transactions on electron Devices, ED-22, No.7, p399. (Jul-1975).
- 4) T.R Groves and R. A. Kendall, JVST, B16, 3168 (1998).

Electrical Conductivity in Oriented DNA

REU Intern: Erik Douglas, Electrical Engineering, Purdue University

Principal Investigator: Mary Tang, Electrical Engineering, Stanford University,
mtang@snf.stanford.edu

Abstract:

With its rod-like structure and base-pair stacking, DNA appears to be a strong candidate for one-dimensional electrical conduction. In these experiments, several interlocked electrode-comb devices were fabricated on a glass wafer, varying the electrode width and spacing.

A procedure known as “dynamic molecular combing” was employed to orient the DNA across the electrodes. The coverage and orientation were measured via fluorescence microscopy. Preliminary electrical data have strongly suggested conductivity. Should DNA prove to be conductive, it could have applications as a molecular wire in nanoscale electronics and in controlling certain biological mechanisms.

Introduction:

Molecular biologists have long studied the properties of deoxyribonucleic acid (DNA) as they pertain to the encoding of genetic information; only recently has DNA begun to be examined as a structural and electrical material. The rod-like structure of DNA has caused some to theorize that it may act as a conductor, with the stacked base-pairs serving as a one-dimensional electron conduit. DNA conductivity and the potential transport mechanisms are hotly contested issues, with many contradictory results having been produced [1, 2]. Should DNA prove to be conductive, the applications would be numerous.

In the emerging field of molecular electronics, DNA could be an attractive molecular wire. The unique property of self-assembly would enable the wires to be precisely targeted, as well as allow for the necessarily wide communication band-width required by such a system [3]. Molecular computers could be massively powerful, yet inexpensive, and DNA wires would facilitate their development.

Conductivity could also be important in understanding, and potentially treating, certain medical conditions. In skin cancer, for example, solar ultraviolet radiation causes cross-linking between adjacent DNA bases, leading to cancerous cells. It is thought that controlled electron transfer may be instrumental in repairing the damage to the helix in such a situation [4], which could prevent the formation of cancerous cells.

Experimental Procedure:

Interlocked electrode-comb devices (Fig. 1) with varied electrode width (2-10 μm) and spacing (2-15 μm) were fabricated from gold on glass. The wafer was then cleaned and treated with octadecyl-trichlorosilane (OTS) to create a silane monolayer to

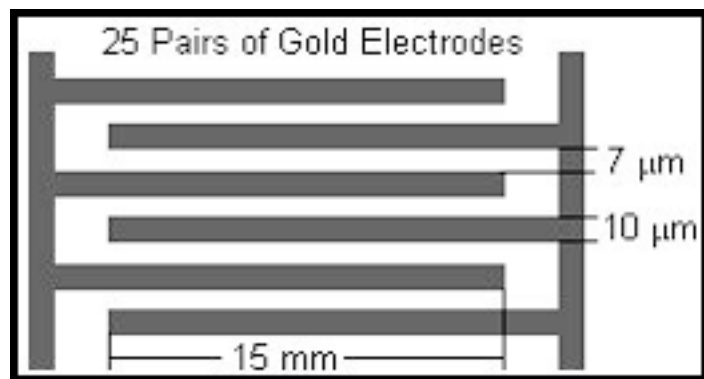


Figure 1. Interlocked electrode-comb device.

which the DNA could bind, as well as to provide a hydrophobic surface.

After being silanized, the wafer was incubated for 5 min. in a lambda-phage DNA solution which had been stained with fluorescent dye (YO-Pro-1), allowing for the DNA to bind at its extremities. The wafer was pulled vertically out of the solution at a constant speed of 100 $\mu\text{m}/\text{sec.}$, in an adaptation of a procedure known as “dynamic molecular combing” [5]. The shear force provided by pulling the wafer from the solution caused the DNA to be oriented across the electrode pairs, enabling the electrical analysis. The DNA alignment and surface coverage were verified using fluorescence microscopy.

The electrical analysis was conducted using a semiconductor parameter analyzer (4156A, Hewlett-Packard). A dc voltage varying from 0 V to 0.1 V was applied across the electrode devices, and the current was measured as a function of this applied voltage. Data were taken before and after the DNA combing procedure to ensure that conductance observed was due to the DNA.

Results and Discussion:

Fluorescence images, such as Fig. 2, displayed the oriented DNA on the electrode wafer. These observations established the utility of the dynamic molecular combing method which was employed.

Control experiments performed before DNA application on a comb device with 10 μm wide electrodes spaced 7 μm apart yielded currents below the threshold of the semiconductor analyzer (10 pA). After DNA combing, the electrical analysis produced the data seen in Fig. 3. As the figure shows, there was a nearly ohmic relationship between the applied voltage and the current observed. This linear relationship strongly suggests that conductance took place in the DNA sample.

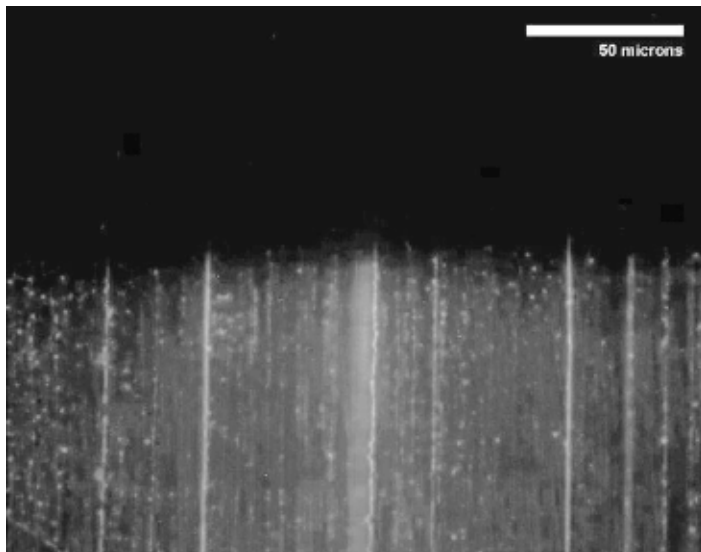


Figure 2. Aligned DNA at coverage interface.

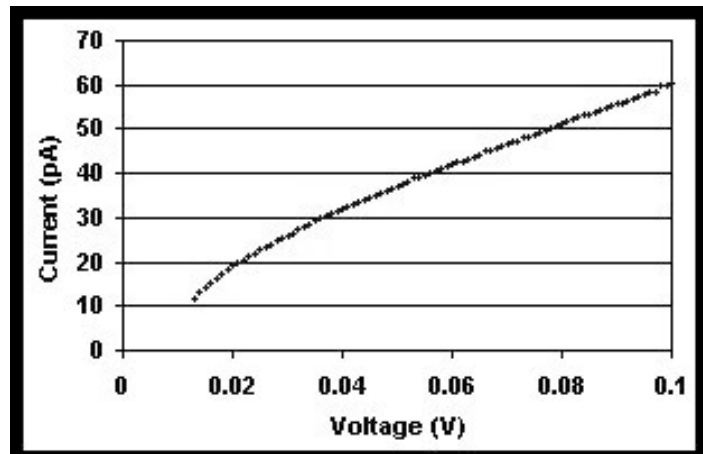


Figure 3. Current through DNA across electrode combs as a function of applied voltage.

Conclusions:

The dynamic molecular combing method employed was seen to be a simple and effective means of orienting DNA. The data produced in this manner strongly suggest that conductivity can take place through bulk DNA. This is encouraging further work on the topic, such as the possibility of modulating conductivity through the introduction of various intercalators.

Acknowledgements:

I would like to thank Mary Tang, and Thorsten Hesjedal for their aid and guidance, Mike Deal and Jane Edwards for their administrative work, and Lance Kam for many helpful discussions.

References:

- [1] Okahata et al., J. Am. Chem. Soc 120, 6165-6166 (1998).
- [2] Priyadarshy, Risser, Beratan, J. Phys. Chem. 100, 17678-17682 (1996).
- [3] Heath et al., Science 280, 1716-1721 (1998).
- [4] Dandliker, Holmlin, Barton, Science 275, 1465-1468 (1997).
- [5] Michalet et al., Science 277, 1518-1523 (1997).

Note added in proof: Recent experiments suggest this particular result may be an artifact; however, these observations do not yet disqualify this experimental method as a tool for electronic characterization of DNA.

Deactivation Kinetics of Supersaturated, Laser Annealed Dopants in Si

REU Intern: Corey Harris, Chemical Engineering, Washington University (STL)

Principal Investigator: James Plummer, Electrical Engr, Stanford University, plummer@ee.stanford.edu

Mentor: Yayoi Takamura, Materials Science and Engineering, Stanford University

Abstract:

The manufacturing process for silicon devices continues to improve in several ways. In order to make smaller, faster semiconductor devices, shallow, highly doped junction regions must be fabricated. Techniques and methods for annealing the implant damage and electrically activating the dopant species in these junction regions is very important. Here, laser annealing is used instead of conventional rapid thermal annealing. The samples underwent ion implantation of the dopant species, followed by laser annealing, and then furnace annealing to investigate the deactivation of the supersaturated dopant species (Sb, P, and B). The Sb and B doped samples do not deactivate until higher temperatures while the P doped samples deactivated quickly at lower temperatures followed by a slow reactivation at higher temperatures.

Introduction:

Several fundamental issues need to be addressed in order to scale down future metal-oxide-semiconductor (MOS) devices. The major issue in junction formation is creating shallower junctions while increasing dopant concentration and maintaining low sheet resistance. The key limitations of conventional rapid thermal annealing (RTA) processes —low electrical activation limited by solid solubility and undesired dopant diffusion — makes creating these shallow, highly doped regions difficult. Therefore, laser annealing is used to create abrupt, ultra-shallow, supersaturated, and highly activated junctions. Currently, junctions as shallow as 35 nm with sheet resistances on the order of $100 \Omega/\text{sq}^1$ are achieved. However, the supersaturated dopants exist in a metastable state and deactivation occurs during subsequent thermal backend processing. Furnace anneals for temperatures between 500-900°C for 40 minutes were used to investigate how subsequent thermal processing affects the highly doped layers. This indepth look at the deactivation kinetics of common dopant species (Sb, P, and B) allows us to quantify this behavior.

Laser Annealing:

Laser annealing is a non-equilibrium process that makes it possible to surpass the thermodynamic solid solubility limits encountered using conventional equilibrium processes like rapid thermal annealing. For this project, laser annealing processes were performed at Verdant Technologies. In the processes, a pulsed laser beam is used to melt a thin layer of the silicon. Dopant diffusivities are approximately eight orders of magnitude higher in the molten silicon than in the solid silicon. As such, dopant distribution in the molten region is uniform, and a more abrupt, box-shaped profile

results since the diffusion stops at the liquid/solid interface. Dopant concentrations exceed equilibrium solid solubility limits because the melt and recrystallization occurs quickly, on the order of 50nsec, trapping dopant atoms on substitutional sites and activating them.

Sample Preparation:

(100) Silicon wafers were preamorphized to a depth of 100 nm with a 55keV, $1 \times 10^{15} \text{ cm}^2$ silicon implant. P, B, and Sb were then implanted at doses to target at least an order of magnitude above solid solubility limits, as detailed in Table 1. Then the samples were laser annealed with ten pulses at an energy density sufficient to melt the silicon to a depth of 140nm (high dose) and 180nm (low dose). Low temperature oxide (LTO) was deposited at 300°C (high dose) and 350°C (low dose) to prevent the outdiffusion of the dopant during the subsequent annealing steps. The wafers were cut into 5mm x 5mm samples and then furnace annealed for 40 minutes at temperatures ranging from 500-900°C.

Table 1

| Dopant | Implant Energy | Dose (cm^{-2}) |
|--------------|----------------------|---------------------------|
| B | 15 | 1×10^{16} |
| B | 15 | 2×10^{16} |
| P | 35 | 3.2×10^{16} |
| P | 35 | 6.4×10^{16} |
| Sb | 60 | 3.2×10^{15} |
| Sb | 60 | 6.4×10^{15} |

Results and Discussion:

Four point probe and Hall measurements were used to measure carrier mobility, carrier concentration, and sheet resistance. The carrier concentration measurements (Fig. 1) show that Sb and B doped samples remain relatively stable until about 700-750°C where the dopant starts to deactivate. The P doped samples, on the other hand, experience a rapid deactivation at low temperatures followed by a slow reactivation at temperatures above ~500°C. Like the carrier concentration trend, the Sb and B doped samples display stable sheet resistance values until 700-750°C (Fig. 2) at which point the Sb sample displays a marked rise in sheet resistance while the B shows only a slight upward turn. The P sample again exhibits dissimilar behavior. There is a rapid rise in sheet resistance and then a more gradual decrease in sheet resistance. The mobility of all three dopants increases monotonically with increasing temperature.

For all three dopants, an increase in dose caused a downward shift in the mobility (Fig. 3). This behavior is expected since at a higher dose there is increased ionized dopant scattering. Figure 4 compares the carrier concentration for the Sb doped samples at the two different doses. At low temperatures, the high dose has a higher carrier concentration and then at 700-750°C decreases to concentrations below the low dose sample. The B doped samples show a similar behavior to the Sb doped samples. For the P, the higher dose sample maintains a higher active carrier concentration until ~500°C. It is believed that this sharper decrease in activation for each of the high dose samples occurs due to a greater driving force for deactivation.

At lower temperatures, the higher dose Sb and B samples have lower sheet resistances (Fig. 5). However, at 700-750°C, the sheet resistance of the high dose samples sharply increases and surpasses the resistance of the lower dose sample. This critical temperature range is the point at which deactivation for both dopant species occurs. The higher dose P sample maintains a higher resistance throughout the entire temperature range (Fig. 6). The deactivation occurs from the beginning of the measured temperature range therefore the curves never intersect as they do for the Sb and B.

Conclusion:

Sb and B doped samples exhibit similar deactivation behavior. The active dose is stable against deactivation up to about 700°C. However, the P samples deactivate at temperatures as low as 350°C and at higher temperatures, a slow reactivation is seen. By increasing the implant dose, mobility decreases and the rate of deactivation increases.

Future Work:

More experimentation will be done on the samples using rapid thermal annealing (RTA) to study the bulk deactivation kinetics for shorter anneals (0-5 minutes). Secondary ion mass spectroscopy (SIMS) analysis will be done to investigate the diffusion profiles of the samples after they have been laser and furnace annealed. Also, TEM images will be taken to study the defects and the precipitates that may exist in the samples.

Further reaching work involves introducing a second impurity into the doped regions to alter the kinetic behavior of the dopant and studying the effect of the surface on the deactivation kinetics.

References:

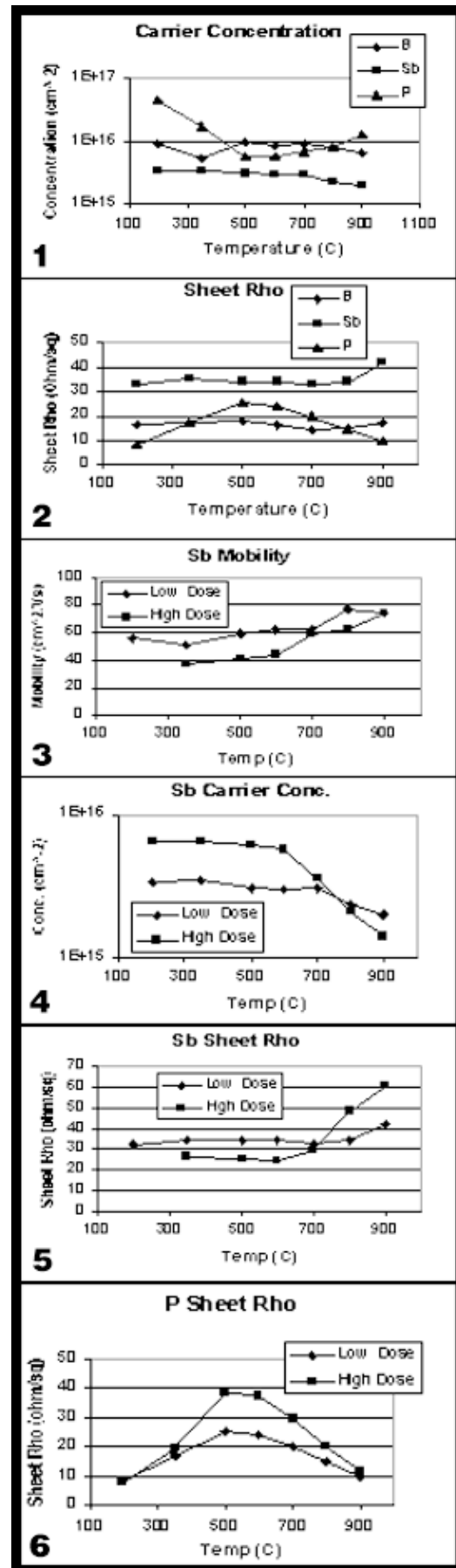
- [1] S. Talwar, G. Verma, K. Weiner, Int'l Conf. on Ion Implantation Tech. Proceedings, vol. 2, 1171-1174 (1998).

Acknowledgements:

NSF, NNUN, SNF
 Dean James Plummer [Dean of the School of Engineering, PI]
 Mike Deal, Jane Edwards [NSF SNF Program Coordinators]

Special Thanks:

Yayoi Takamura [Graduate Student, Mentor]
 Peter Griffin [Senior Research Scientist]



A Microfluidic Device for DNA Analysis by Pyrosequencing

REU Intern: Scott Harrison, Chemical Engineering, Rice University

Principal Investigator: Peter B. Griffin, Dept. of Electrical Engineering, Stanford University,
griffin@stanford.edu

Abstract:

The great demand for genetic information for the purposes of medical research and medical diagnostics is motivating the development of faster, inexpensive DNA sequencing devices.

In this study, we fabricated a microfluidic device that is attempting to sequence DNA using pyrosequencing, a sequence-by-synthesis method. The microfluidic device consists of a microchannel in a glass wafer coated with amorphous silicon that has been anodically bonded to another glass wafer. DNA is immobilized in the main microchannel and nucleotides are moved through the microchannels by electro-osmosis.

Introduction:

In recent years, a great need for high-throughput, low-cost DNA sequencing has emerged as research efforts have focused on deciphering the human genome. The need for fast, low-cost DNA sequencing devices has prompted the consideration of microscale devices that can be fabricated inexpensively using existing microfabrication technologies and operated at low cost using small amounts of chemicals.

In this study, we fabricated a microfluidic device that will use pyrosequencing, a DNA sequencing method that utilizes an enzyme system to detect the incorporation of a nucleotide into a DNA sequence. The nucleotide incorporated into the elongating DNA primer strand must be complementary to the nucleotide existing in the DNA template strand, according to the Watson-Crick base pairing rules. With the pyrosequencing method, nucleotides, each containing one of the four possible bases, are iteratively introduced to the growing DNA primer strand. Light is generated only when a complementary nucleotide is incorporated into the DNA molecule. The product of incorporation, pyrophosphate, is used in a subsequent enzymatic reaction to generate light [1].

The microfluidic device fabricated in this study is comprised of a microchannel in a glass wafer with an amorphous silicon coating that is anodically bonded to another glass wafer. The channel system is comprised of a main channel and four cross channels with DNA immobilized in the main channel as shown in figure 1. Washing buffer will be introduced to the system in the main channel and each of the four nucleotides will be introduced into the system from its own cross channel. Electro-osmosis will be used to move fluids through the microchannels by applying an electric field along the channels [2].

Procedure:

A photolithographic mask was designed for the channel pattern. Borofloat glass wafers were cleaned and each was coated with a

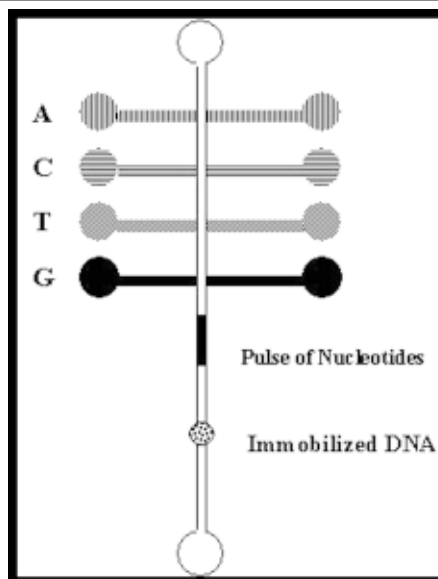


Figure 1:
The channel system design is shown at left. Electro-osmosis is used to move a pulse of nucleotides into the main channel and downward toward the immobilized DNA. Nucleotides with:
Adenosine(A),
Cytosine(C),
Thymine(T), and
Guanine(G)
are in the four cross-channels.

1000 Å thick layer of amorphous silicon. The wafers were then coated with a 1 µm thick layer of Shipley 3612 photoresist, exposed with the channel pattern, and developed. Three channel systems of varying main channel lengths were patterned on each wafer. A plasma etcher using SF₆ and Freon 115 was used to etch through the amorphous silicon layer on the glass. Wet etches using 49% HF were performed to create the microchannels in the glass. After etching, the photoresist was stripped. Using a drill press, holes of 0.75 mm diameter were drilled at the end of each microchannel. The overhangs created from wet etching were brushed off and the wafer was cleaned. In the final step of device fabrication, a cleaned glass wafer was anodically bonded at 350°C to the etched wafer to enclose the microchannels.

The device was tested at the Stanford DNA sequencing center. Filling several wells with water — allowing for capillary action — filled most channels in about ten to fifteen minutes. Water was added until the channels were completely filled. The device was then tested to see if electro-osmosis could be observed. Magnetic beads were added to help in visualizing water flow.

Results and Discussion:

The glass wafers were etched with a HF wet etch to form microchannels. The channel width on the mask was 30 µm. The wet etches produced microchannels that were approximately 80 µm in width and 50 µm in depth. An image of the etched channels is shown in figure 2. Five glass wafers were etched and two of these were anodically bonded to blank glass wafers to form microfluidic devices.

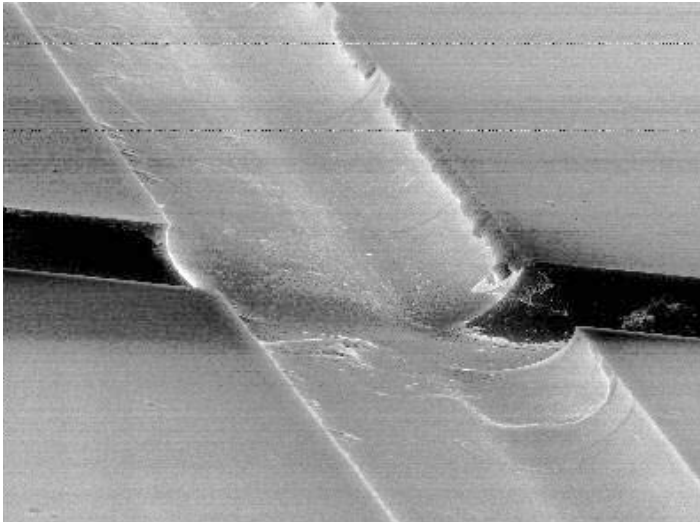


Figure 2: An intersection of two etched microchannels taken at a magnification of 700 is shown in the Scanning Electron Micrograph.

Magnetic beads were placed in a cross channel and 130 volts, the maximum available voltage, was placed across the channel. The beads moved on the order of a mm per sec toward the negative terminal, indicating water was moving in this direction. The power supply was then turned off and the beads stopped flowing, indicating the flow of water had ceased. When the polarity of the voltage was reversed, the beads moved in the opposite direction toward the negative terminal.

The next step toward DNA sequencing is to immobilize DNA in the main channel. A gold stripe will be deposited within the main microchannel of the channel system before the bonding step. DNA immobilization will be accomplished by passing thiolated DNA over the gold stripe where it will attach since thiol groups bind easily to gold [3]. Other areas of future development are controlling electro-osmosis at high voltages, adding electrodes to glass for applying voltages and mixing liquids in the channels, and optimizing the pyrosequencing enzyme system for use in the device.

Summary:

Two microfluidic devices were fabricated and electro-osmosis was observed in the microchannels. The next step is to immobilize DNA in the main microchannel using gold-thiol linkage. It should then be possible to sequence a short DNA sequence with the fabricated microfluidic device. This accomplishment would provide additional motivation for further development of the device.

References:

- [1] "Real-Time DNA Sequencing Using Detection of Pyrophosphate Release", M. Ronaghi, S. Karamohamed, B. Pettersson, M. Uhlen, and P. Nyren, *Analytical Biochemistry*, vol. 242, pp. 84-89, 1996.
- [2] "Electroosmotic Pumping and Electrophoretic Separations for Miniaturized Chemical Analysis Systems", A. Manz, C.S. Effenhauser, N. Buggraf, D.J. Harrison, K. Seiler, and K. Fluri, *J. Micromech. Microeng.*, vol. 4, pp. 257-265, 1994.
- [3] "Characterization of DNA Probes Immobilized on Gold Surfaces", T.M. Herne and M.J. Herne, *J. Am. Chem. Soc.*, vol. 119, pp. 8916-8920, 1997.

Acknowledgements:

I would like to thank Peter Griffin for working with me this summer. I would also like to thank Reza Kasnavi and Jason Rau for their assistance in my project and Mary Tang for her advice. I want to acknowledge Mike Deal, Jane Edwards, and Melanie-Claire Mallison for their terrific coordination efforts. I would like to express my gratitude to my fellow REU students for their inspiration and support. Lastly, I would like to thank the NSF and NNUN organization for their support.

Releasing Metal Cantilever Beams for Use as Switches in MicroElectroMechanical Systems (MEMS)

REU Intern: Jesse Hwang, Mechanical Engineering, Yale University

Principal Investigator: Bruce Clemens, MatSci and Engr, Stanford, clemens@sierra.stanford.edu

Mentors: Mark Phillips, Christine Esber, MatSci and Engr, Stanford

Abstract:

In this work, we aim to release thin metal films from a silicon wafer, producing free-standing metallic beams. We explore two methods to accomplish this. In the first, the backside wet etch, we use both dry and wet etch techniques to produce a hole that begins at the backside of the wafer and ends at a patterned, front side, aluminum layer. For the second method, a hydrofluoric acid (HF) vapor chemical etch is employed to undercut the sacrificial oxide layer beneath a patterned, front side, molybdenum and tungsten metal multilayer.

Introduction:

In one scheme for a MEMS switch, a free-standing, cantilever, metal beam is deflected by an applied voltage or mechanical input to an electrical contact, completing a circuit (Figure 1).

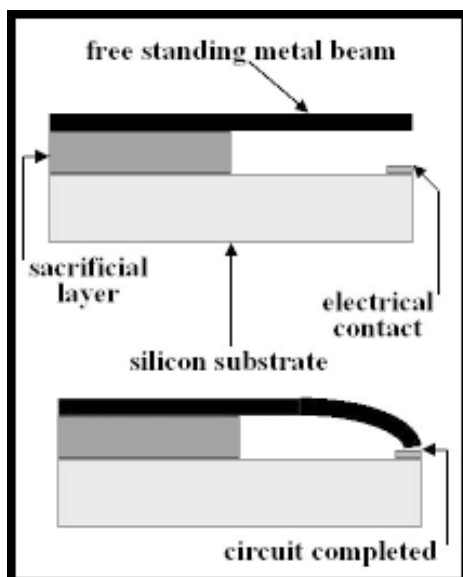


Figure 1: General scheme for a MEMS electromechanical switch

Bending moments within the metal films that compose the beams contribute to warping, making beams unsuitable candidates for MEMS switches (Figure 2a). Depositing metallic multilayers via magnetron sputtering addresses the problem of bending moments by alternating tensile and compressive layers of two or more different materials, controlling the deposition stress gradient and tuning the bending moment to zero. A consistent, non-deformed, free-standing beam has not been developed using these thin film multilayers, however, due to difficulties associated with releasing the beams from underlying layers.

This project's goals are to 1) ascertain whether or not these multilayer beams will be straight once released and 2) generate fabrication schemes that yield straight, free-standing beams that

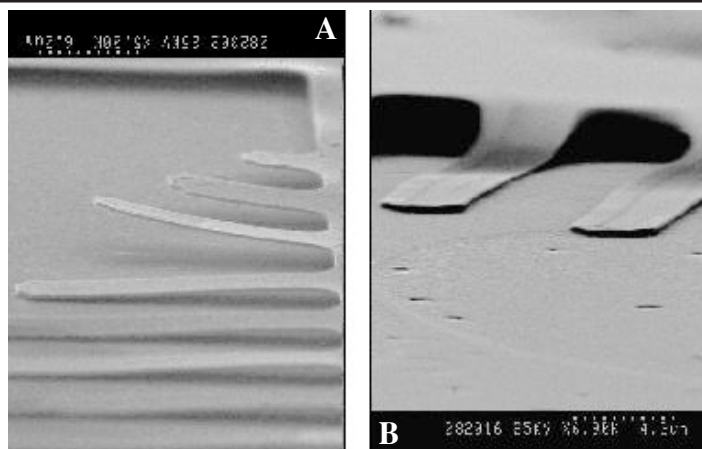


Figure 2: A. Warping. B. "Sticking."

also address the "sticking" problem. In prior work, a liquid etch was used to undercut a sacrificial layer beneath patterned metal multilayer beams. This scheme resulted in sticking: adhesion between the substrate and the beam, presumably attributed to liquid surface tension effects (Figure 2b).

To overcome the sticking problem, we attempt the backside wet etch and HF vapor etch. In the backside wet etch, the final product will consist of free-standing, metal beams positioned above an open window, thus preventing any surface where sticking may occur (Figure 3a). In the HF vapor etch, we undercut with a vapor instead of a liquid to avoid surface tension effects (Figure 3b) and to reduce mechanical abuse of the beams during fabrication.

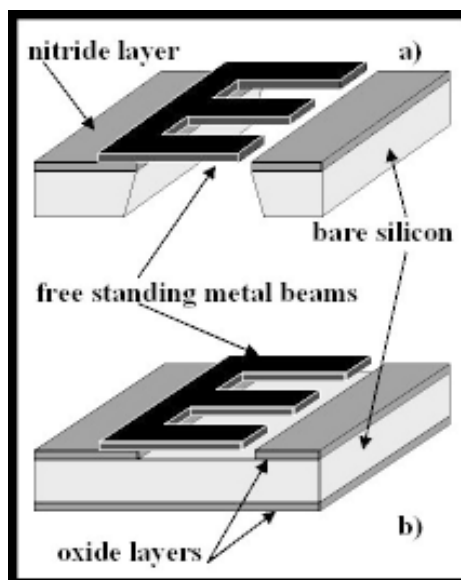


Figure 3: Final products from, a) the backside wet etch, and b) the HF vapor etch.

Procedure:

For the backside wet etch, we first grew 3000 Å of silicon nitride (Si_3N_4) onto 4-inch silicon wafers in a Tylan furnace. On the polished front side, trenched patterns of windows containing beams of varied heights, widths, and shapes were created using photolithography (Figure 4a). Next, a single aluminum layer 2000 Å in thickness was sputtered (Figure 4b). Liftoff was performed in an ultrasonic acetone bath, leaving unreleased aluminum beams (Figure 4c). For backside processing, we used photolithography to pattern a series of open windows, their size determined by the directional etching nature of Tetramethylammonium Hydroxide (TMAH). A Freon-23 (CHF_3) and oxygen (O_2) plasma etch at 25 mTorr and RF power of 50 Watts was then used to remove the first nitride layer on the backside (Figure 4d). TMAH (25% w/w aqueous solution) etched through the back of the wafer, isolated by rubber gaskets sealed with vacuum grease (Figure 4e). The same plasma etch removed the final nitride layer, releasing the aluminum beams (Figure 4f). Finally, the beams were analyzed qualitatively with a Scanning Electron Microscope (SEM).

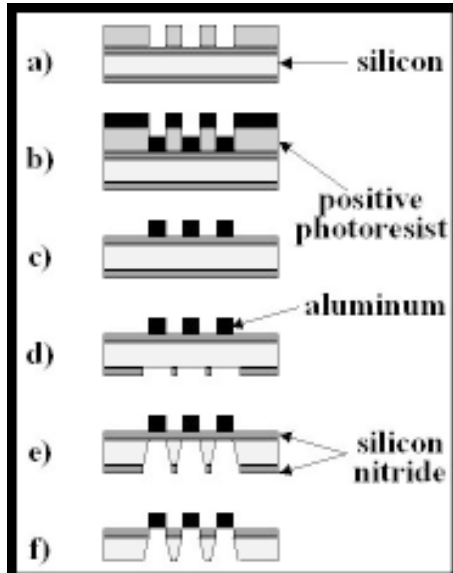


Figure 4: a-f, the backside wet etch.

The HF vapor etch began with a 1 μm coat of silicon oxide (SiO_2) on silicon wafers and the same front side processing. Instead of an aluminum film, however, we used Mo/W metal multilayers. The wafer was placed front side down above a beaker of concentrated 49% HF acid. A light bulb heated the wafer 15°C above room temperature to prevent acid condensation on the wafer. The vapor then undercut the oxide and released the beams, making any backside processing unnecessary.

Results and Conclusions:

Figure 5a shows one window obtained by the SEM after the final nitride etch in the backside wet etch; warped beams can be observed. Since we were dealing with a layer of aluminum rather than a multilayer, downward warping was expected from the onset. In addition, the longer beams are snapped. Furthermore, although not shown, the TMAH wet etch attacked several windows on the front side, stripping off aluminum. The SEM image also indicates that the wet etch was not aligned correctly with the mask windows, since the etch stopped behind the base of the beams.

There are several disadvantages to the backside wet etch. First, TMAH is extremely toxic and etches too slowly, requiring approximately 24 hours for a 4-inch silicon wafer. The process removes all material beneath the beams, which precludes surfaces for electrical contact and makes the transition to application less obvious. The absence of sacrificial layers also makes the windows extremely delicate; repeated front side/backside handling inevitably contributes to beam damage. As a result of the directional etch, the variable thickness of wafers prevents a precise etch around the mask windows.

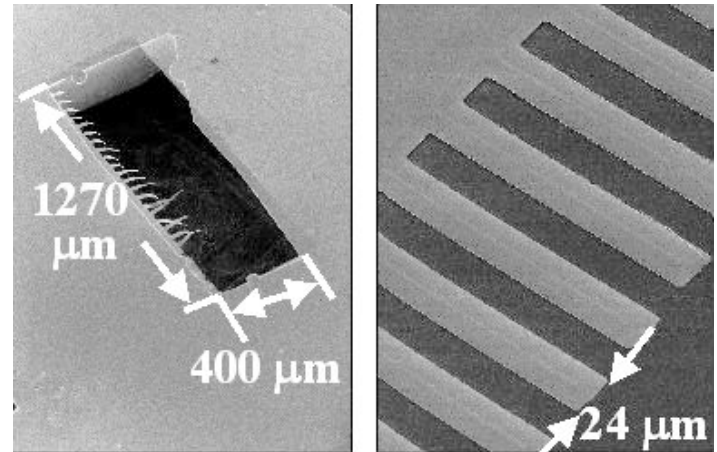


Figure 5: Results for: a) backside etch, and b) HF vapor etch.

Figure 5b is an SEM image of the HF vapor etch. While the testing of the process has been minimal to date, we can conclude that the vapor does indeed undercut the oxide layer. The dark regions along the edges of the beams indicate undercutting, while the lighter region down the middle of the beams are presumed to be unreleased regions. Although this image shows straight beams, other windows were observed to have many warped ones. It is still to be determined how well the process releases beams and under what conditions the vapor attacks the metal multilayer. This process, however, does seem more promising to pursue than the backside wet etch, since it has fewer steps and requires less mechanical abuse on the beams. The only drawback to the HF vapor etch seems to be the danger of corrosion and injury associated with concentrated HF.

References:

- [1] Doerner, M.F., Nix, W.D., "Stresses and Deformation Processes in Thin Films on Substrates," CRC Critical Reviews in Solid State and Materials Sciences, Volume 14, Issue 3, (1988) p. 225-267.
- [2] Friedberg, P., "Multilayer Conducting Layers for MEMS," The 1999 NNUN REU Research Accomplishments, p. 58-59.
- [3] Spearing, S.M., "Materials Issues in Microelectromechanical Systems," Acta Materialia, 48 (2000), p. 179-196.

Acknowledgements:

I would like to thank the following people and organizations for their invaluable aid and sponsorship: Mark Phillips, Christine Esber, Dr. Bruce Clemens, Dr. Michael Deal, Jane Edwards, The Nix and Clemens groups of the MatSci and Engr Department at Stanford, the SNF Staff, NNUN, the National Science Foundation (NSF), and my fellow SNF REU 2000 Student Participants.

Aspect Ratio Dependant Microtrenching In High-Density Plasma Etched Microstructures

REU Intern: Aghapi G. Mordovanaki, Electrical Engineering, University of Michigan-Dearborn.

Principal Investigator: James P. McVittie, Integrated Systems, Stanford, mcvittie@cis.stanford.edu

Abstract:

Microtrenching (a non-uniform deformation at the bottom of a microstructure), as well as sidewall bowing can occur when etching silicon with a High-Density ICP plasma (HDP). This deformation of the expected profile is thought to be caused by the effect of ion reflection off the structure sidewalls. We have studied the geometry of the etch profile using the SEM (Scanning Electron Microscopy) as a function of the aspect ratio (depth/width of a trench), the chemistry of the plasma (Cl_2 or HBr as etchant gas), the thickness of the mask, the plasma source power, and the substrate bias power. A model is to be proposed to relate the amount of microtrenching to the different etch parameters (chemistry, thickness, bias, and plasma density).

Introduction:

The increasing demands of Ultra Large-Scale Integrated Circuits (ULSI) technology are pushing toward the development of new etching techniques that result in high definition micro-scale features, with high aspect ratio, and straight and regular sidewalls. High Density Plasma (HDP) etching systems have proven, in the second half of the past decade, to be very dependable in meeting the requirements of the ULSI. Nevertheless, deformations in the etch profile have been observed while using this generation of etchers, like bowing of the sidewalls and “dovetailing” at the bottoms (induced by enhanced etching near the sidewalls), known as microtrenching.

Microtrenching has been observed for most anisotropic plasma etch processes with the worst cases occurring during the silicon

etch with a Cl_2 plasma [1]. This constituted a direct motivation for the research and experiments discussed in this paper, since, at the Stanford Nanofabrication Facility, microtrenching was occurring with both HBr and Cl_2 plasma.

System:

The system we used was an ICP High density plasma etcher (Lam 9600). In ICP systems, an RF power source is applied at the substrate where the wafer is clamped that causes a voltage drop to build up between the wafer and the plasma [2]. The positive ions from the plasma get accelerated by the field following a straight trajectory perpendicular to the surface of the wafer and knock atoms off from the silicon lattice producing a highly directional etching.

ICP systems operate at a very low pressure (order of 10 mT) which increases significantly the directionality of the bombarding ions, and consequently, the quality of the etch. Another important advantage is that ICP systems have an independent control of the plasma source power and the substrate power. This way a high-density plasma (10^{12} cm^{-3}) can be created without increasing the ion energy which would induce damage to the wafer surface.

Experimental Procedure:

In the first set of experiments, we wanted to study the dependence of the microtrenching as a function of the aspect ratio of the etched structure. Aspect Ratio (AR) is the ratio of the structure height over its width. We chose to quantify microtrenching by the ratio of the average height of the microtrench over the depth of the

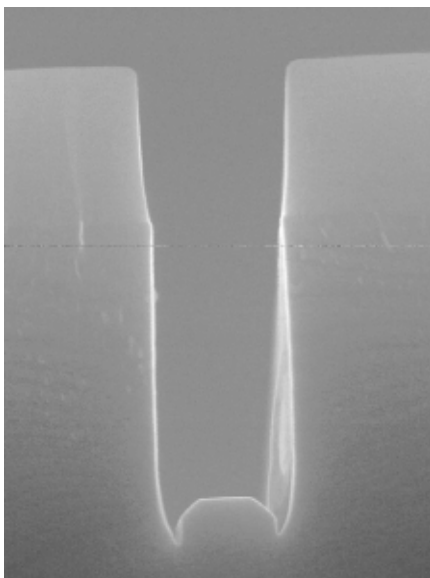


Figure 1: SEM picture of a $3.5 \mu\text{m}$ deep trench with microtrenching at the bottom.

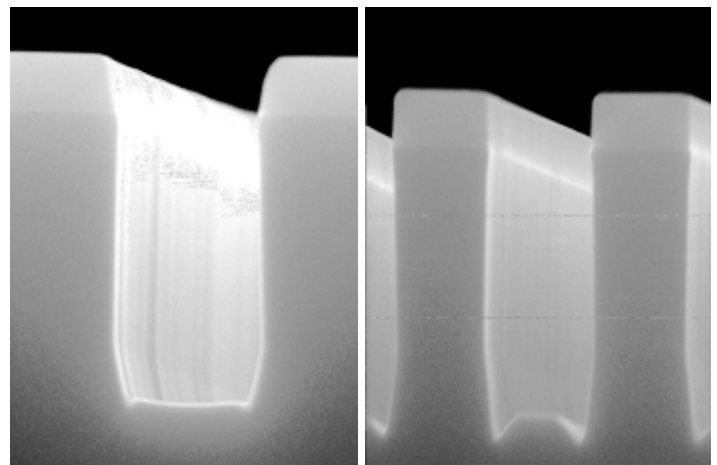


Figure 2: SEM picture of low aspect ratio trench with little microtrenching (left), And large aspect ratio with more massive microtrenching (right).

structure itself. We started by thermally growing a layer of oxide on a bare silicon wafer. After lithography, the wafers were etched using the ICP system (Lam 9600). (See chart 2 for the etch parameters). Finally we used the SEM to look at the samples and make measurements.

Results:

All samples etched showed microtrenching effects with HBr as main etchant gas. Moreover, microtrenching seemed dependant on the aspect ratio of the trench. In fact, for structures with a low aspect ratio (very wide opening) almost no microtrenching has been observed, while on the same wafer, with a larger aspect ratio (narrow opening) microtrenching was noticeable (Fig. 2).

Also a correlation has been observed between the thickness of the mask and the amount of microtrenching. Microtrenching tends to increase with thicker mask.

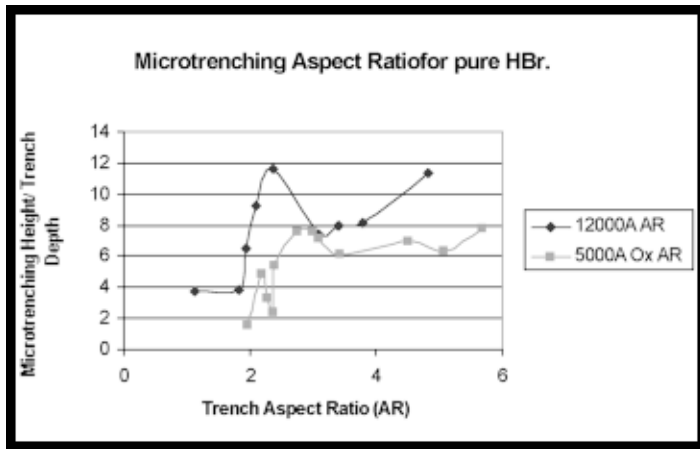


Chart 1: Plot of microtrenching versus aspect ratio.

Experiment II:

In the second set of experiments, we increased the plasma source power, and the substrate bias power.

We obtained perfectly flat bottoms (see Fig. 3). But we noticed that the bowing in the sidewalls has increased significantly. Also the selectivity with respect to the oxide decreased dramatically.

Chart 2: ICP etch parameters:

| | Plasma Source Power | Bias Power | Bias Voltage | Etch Time |
|---------------|---------------------|------------|--------------|-----------|
| Experiment I | 250 W | 60 W | 104 V | 540s |
| Experiment II | 500 W | 150 W | 93 V | 540s |

Discussion and Theory:

Even though we hadn't enough time to finish the second set of experiments as planned, some conclusions could be drawn from the results already obtained. The positions of the bowing in the sidewalls and corresponding microtrenching suggest that microtrenching may be caused by ion specular reflection off the sidewalls of the silicon.

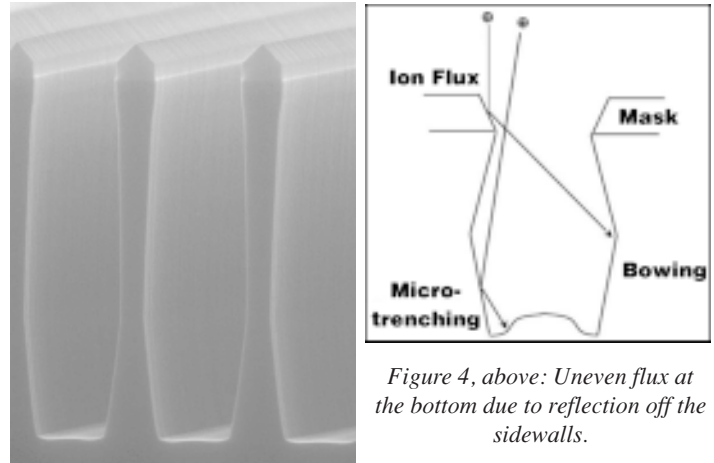


Figure 3: SEM picture of etches done with high power settings. No microtrenching is occurring.

In fact the impinging ions obey a certain angular distribution function that allow a fraction to fall with an angle slightly deviated from the ideal vertical. Therefore, some ions might hit the sidewalls before arriving at the bottom of the trench and reflect specularly toward the bottom edges. This constitutes an additional ion flux near the sidewalls that increases the etch and causes the microtrenching (Fig. 4).

At a higher bias power, the voltage across the sheath is higher, and so is the directionality of the bombarding ions. Therefore, fewer ions are arriving with an angle, and the component of the ion flux at the bottom due to ion reflection becomes less important, which yields a homogenous flux all over the bottom, eliminating the microtrenching.

Conclusion:

Although the above-mentioned theory succeeds in explaining some of the microtrenching behaviors, it still fails to offer a satisfactory and complete explanation to all observed characteristics. More experiments need to be done in order to complete and test the theory suggested.

References:

[1] M. A. Vyvoda et al., J. Vac. Technol. B 18, 820. "Role of Sidewall Scattering in Feature Profile Evolution during Cl₂ and HBr Plasma Etching of Silicon" (1999).
 [2] J.B. Carter et al., J. Vac. Technol. A 11, 1301. "Transformer Coupled Plasma Etch Technology for the Fabrication of Subhalf Micron Structures" (1993).

Etch Characterization of Nb Disks for Superconductor Penetration Depth Measurements

REU Intern: Eric Taketatsu, Electrical Engineering, University of Hawaii at Manoa

Principal Investigator: Kathryn A. Moler, Applied Physics, Stanford University, kmoler@stanford.edu

Mentor: Per Björnsson, Stanford University, perbj@stanford.edu

Abstract:

A traditional characteristic of superconductors is perfect diamagnetism — no magnetic field inside the superconductor. Magnetic fields in real superconductors exponentially decay to zero on a length scale known as the penetration depth. We plan to measure penetration depths using a novel method, scanning Superconducting QUantum Interference Device (SQUID) susceptometry of superconducting disks.

To fabricate 1.5 and 3- μm niobium disks on a silicon substrate, we optimized the etching and photolithography processes. Using an MRC reactive ion etcher, with SF_6 as the process gas, we tested various etch parameters such as pressure, time, and power. Using the optimized parameters, we characterized the etch anisotropy. Optimization of such processes on Nb disks will allow for better penetration depth measurement.

Introduction:

Niobium (Nb) is of interest to us when it is cooled below 9K (boiling point of liquid helium is at 4K) in that it becomes superconductive and has the highest critical temperature of all elemental superconductors. Two traditional properties that define superconductivity are perfect DC conductivity, and perfect diamagnetism or that its net magnetic flux within is zero. These properties are exhibited when niobium is cooled to or below its critical temperature of 9K.

When an external magnetic field is applied to a superconductor, the magnetic flux within doesn't step toward zero, instead it decays exponentially in a surface layer and this length scale of the decay is the penetration depth. Many techniques have been used to measure penetration depth. A novel approach to measuring penetration depth of superconductors using Superconductor QUantum Interference Device or SQUID is of interest to us.

Initially, tin disks were used to analyze the effectiveness of this new penetration depth measurement technique. However a problem with using tin disks is that there were irregular grains. This effect made measuring penetration depth of a uniform structure to be impossible with tin. The goal is to use niobium, which is thought to be of better quality, thereby allowing us to compare this new measurement technique to previous ones. So process fabrication characterization of disks was needed to be able to use these niobium disks.

Procedures:

Etch Rate Characterization:

Before we could fabricate the Nb disk samples we needed to establish base etching parameters. The pieces were immersed in

buffered oxide etch for approximately 12 minutes to strip off a SiO_2 layer. Then each piece was dried and hand swabbed with photoresist. Next we baked the samples and then placed them in the MRC reactive ion etcher where power, pressure, and time were varied to determine the optimum conditions to etch the pieces using SF_6 as the processing gas.

Power was varied from 35W to a 100W while pressure was kept near 30 mTorr and the etch time was set at 2 minutes. A second test involved a variation of pressure from 10 mTorr to 60mTorr. The power was kept at 50W and the etching time was sustained for 2 minutes. Finally time was varied with pressure kept at 30mTorr and power set to 50W.

After processing with the etcher, the pieces were stripped of photoresist and a surface profilometer was used to measure the etch depth.

Photolithography and Sidewall Profiling:

To determine an optimal set of etching parameters, we needed to observe the sidewall profiles of a set of photolithographed disks on Nb pieces. Since our mask was a negative mask, we used negative resist as the primary resist coating. We spun our samples using a Laurell manual spinner and aligned them using the Karl Suss mask aligner. We used compiled data from our profilometer measurements to determine a base set of parameters. This was chosen to be at 50W, 30mTorr and about four minutes. We varied

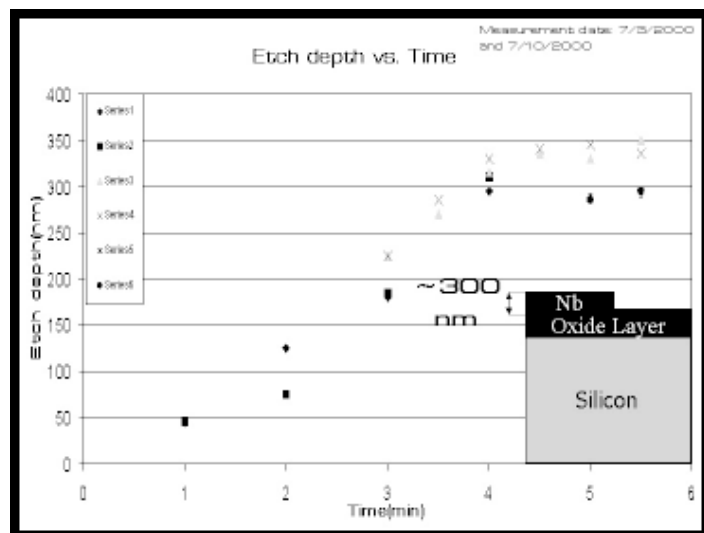


Figure 1. Etch depth vs. Time. This graph shows an increase of etch depth with time which begins to level off near 4 mins. This is attributed to the penetration of SF_6 through the Nb layer down into the oxide layer.

the time and kept the other parameters constant. The samples were then stripped of photoresist and were viewed under SEM.

Results and Conclusion:

Profilometer measurements showed that increasing power, pressure, or time increased the depth etched. In figure 1, we see that there is a increase in etch depth with time, however nearing 4 minutes of etching, we notice that the etch depth starts to level off. This occurred after we penetrate through the Nb layer and started to etch away the oxide layer.

After compiling data from profilometer measurements, we got a set of base parameters that was at 50W, 30mTorr and 4 minutes. This data was then used in conjunction with SEM pictures of the sidewalls of niobium disks. We found that when etching below or after 4.5 minutes, we did not get optimal results. For times under 4.5 minutes, there were remnants of underetching, and for times above, there was overetching and undercutting of the disks. Using SEM data, we determined the optimum etching for the MRC Reactive Ion Etcher to be 30 mTorr, 50W, and 4.5 minutes.

After successfully fabricating the Nb disk, we hope to be able to utilize SQUID susceptometry technique to determine penetration depth of Nb and compare this technique to others.

Acknowledgements:

Thanks to:

National Science Foundation for funding
National Nanofabrication Users Network
Stanford Nanofabrication Facility
HYPRES for supplying Niobium film

Special Thanks to:

Dr. Kathryn Moler
Per Björnsson
Mahnaz Mansourpour
Mike Deal and Jane Edwards

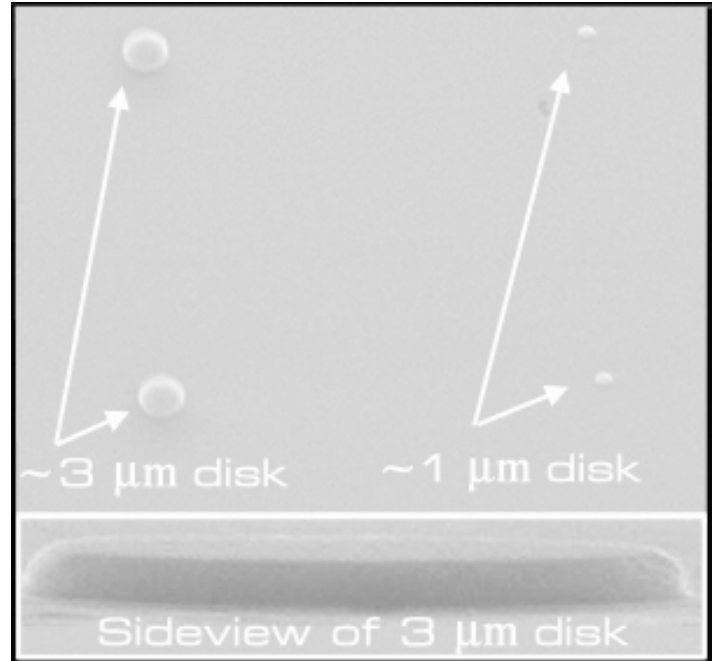


Figure 2. Top: Top view SEM pictures of 1.5 & 3 μm Nb disks.
Bottom: Sideview of a 3 μm disk, used for sidewall profiling.

Wet-Oxidation of Digitally Alloyed AlGaAs

REU Intern: Andrea Tao, Chemistry and Physics, Harvard University

Principal Investigators: James S. Harris, Jr. and Glenn Solomon, Department of Electrical Engineering, Stanford University, Harris@snowmass.stanford.edu, Solomon@snowmass.stanford.edu

Mentor: Chien-chung Lin, Dept. of Electrical Engineering, Stanford University

Abstract:

Vertical-cavity surface emitting lasers (VCSEL) have been a topic of interest in engineering research due to the requirement of 2-D laser arrays in applications such as fiber-optic communication networks, spectroscopic sensors, and interferometers. Studies have concentrated on increasing the efficiency of VCSELs by employing oxide microstructures within the device, such as current apertures and buried refractive microlenses. This study concerns itself with the investigation of tailoring Al content within AlAs layers to produce defined microstructures upon oxidation.

Introduction:

When it was found that the wet-oxidation of aluminum-containing semiconductors, including AlGaAs, produces a robust oxide with a low refractive index, it led to a variety of advances in laser structures [1]. Specifically, oxidized AlGaAs has been employed in VCSELs [2], devices which have become attractive in applications including optical fiber communications and optical interconnects due to their tunable resonant cavities.

In such applications, it has been shown that the presence of oxide microstructures increases device efficiency both optically and electronically. Lower threshold currents as well as increased modal stability and selectivity in VCSELs confined by oxidized AlGaAs apertures have been observed [3]. Similarly, AlGaAs layers can be oxidized within VCSELs that have been modified to emit from their GaAs substrates, creating buried refractive microlenses which collimate emitted light into a uniform beam [2]. It was determined that tapered oxidation fronts and curved microstructures could be achieved by tailoring $\text{Al}_x\text{Ga}_{1-x}\text{As}$ content and thickness to obtain a controlled oxidation of the layers [4].

The goal of this study was to characterize the wet-oxidation of these tailored layers by observing the movement of the AlGaAs oxide fronts through SEM images.

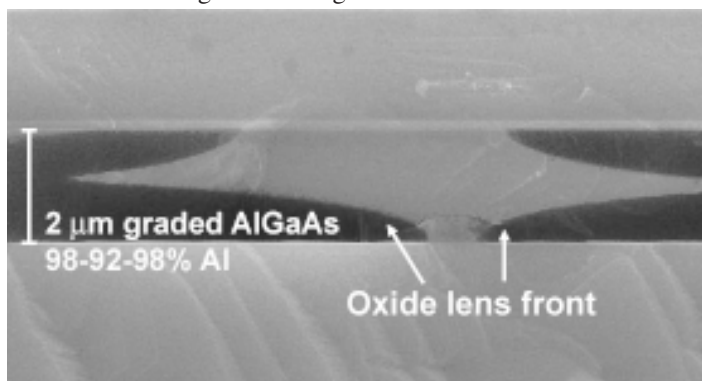


Figure 1. SEM image of a partially oxidized trench where the darker regions represent the formed oxide.

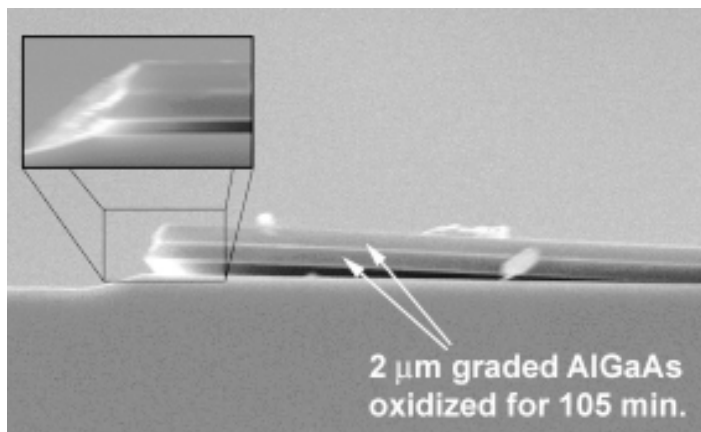


Figure 2. SEM image showing AlGaAs delamination which occurred in those samples whose periods exceeded one hour.

Experimental Procedure:

A microlens wafer was fabricated by growing two digitally-graded layers of AlGaAs — in varying steps of 92% and 98% Al-containing AlGaAs — on a GaAs $\langle 100 \rangle$ substrate and buffer layer using molecular beam epitaxy. The layers were capped with a protective GaAs layer. The $\text{Al}_x\text{Ga}_{1-x}\text{As}$ layer bordering the buffer layer was graded over a $2\ \mu\text{m}$ thickness from $x=0.98$ to $x=0.92$ top to bottom. A $1500\ \text{\AA}$ GaAs barrier was then grown, followed by another $2\ \mu\text{m}$ $\text{Al}_x\text{Ga}_{1-x}\text{As}$ layer graded from $x=0.90$ to $x=0.98$ top to bottom.

Processing consisted of patterning with a $5\ \mu\text{m}$ trench pattern and etching in sulfuric acid solution to expose AlGaAs sidewalls for lateral oxidation. Samples were immediately subjected to wet-oxidation at temperatures of approximately 425°C while bubbling N_2 through a 95°C de-ionized water bath at a 100% gas-flow rate. Under these conditions, it was assumed that the normal lateral oxidation rate of the AlGaAs layers was linear — in other words, reaction rate-limited rather than diffusion-limited.

Results and Discussion:

Figure 1 shows an SEM image of partially oxidized mesa, where dark regions correspond to the formed $(\text{Al}_x\text{Ga}_{1-x})_2\text{O}_3$ oxide and lighter regions to the unoxidized AlGaAs and GaAs. Wet-oxidation resulted in a well-defined alumina/AlGaAs front with a convex profile characterized by the continuous Al grading. Samples showed a smooth lattice interface with no voids.

Although no post-oxidation fabrication or thermal cycling processes were conducted, after longer periods of wet-oxidation,

the oxidized layers began to delaminate by peeling entirely off the GaAs buffer layer, as shown in Figure 2. This mechanical instability is evidence of the poor interface semiconductor/oxide interface most likely resulting from physical strain, supporting previous reports that the formed oxide consists of a porous structure [5, 6]. This “peeling” effect poses a problem for the incorporation of AlGaAs microstructures in VCSEL devices, but other groups have reported that the problem can be mitigated by employing thin AlAs layers around 20nm or increasing Ga content [9].

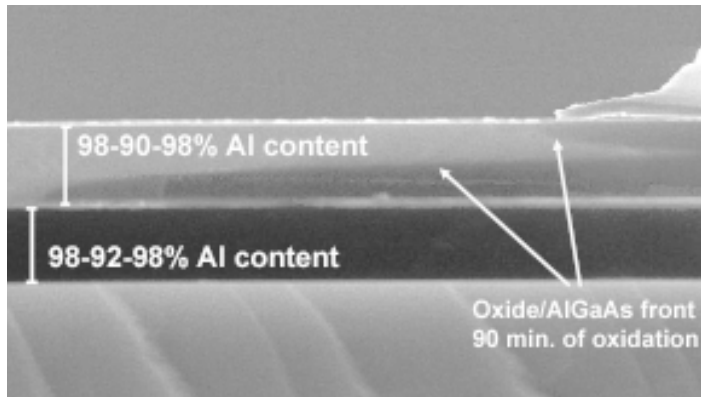


Figure 3. SEM image of the asymmetric oxidation front of the slowly-oxidized AlGaAs layer, attributed to reactant diffusion.

Another difficulty presented in fully characterizing the wet-oxidation of these microstructure samples is reactant diffusion, where oxidants diffuse through a “feeder channel” in the porous alumina layer. In Fig. 3, the results of reactant diffusion can be seen in the asymmetric oxidation of the AlGaAs layer bordering the GaAs cap. Other groups have modeled oxidation depth in the presence of thin GaAs barriers as a linear sum of normal lateral oxidation and oxidation resulting from reactant diffusion [6]. This model predicts that a 130 GaAs barrier will be sufficient to counteract diffusion of reactants for $\text{Al}_x\text{Ga}_{1-x}\text{As}$ where $x=0.94$. However, the results obtained from this study employing a 1500Å barrier suggests that model does not apply to higher-content Al layers.

Conclusion and Future Work:

In summary, the fabrication of oxide microstructures can be prompted by carefully tailoring GaAs barriers and Al content grading in AlGaAs layers for suitable oxidation conditions. More comprehensive studies should include discussion of oxidation rate dependence on reactant diffusion for higher Al content AlGaAs. It is anticipated that future work involving experimentation with these AlGaAs layers will permit the integration of these optical and electrical structures into working devices.

References:

- [1] J.M. Dallesasse, N. Holonyak, Jr., A.R. Sugg, T.A. Richard, and N. Elzein. Appl. Phys. Lett., vol. 57, pp.2844-2846, 1990.
- [2] O. Blum, K.L. Lear, H.Q. Hou, and M.E. Warren. Electronics Letters, 32 (15), 1406-1408, 1996.
- [3] M.C. Larson and J.S. Harris, Jr. IEEE Photon. Technol. Lett., 7, 1267-1269, 1995.
- [4] O. Blum, C.I.H. Ashby, and H.Q. Hou. Appl. Phys. Lett., 70 (21), 2870-2872, 1997.
- [5] K.D. Choquette, K.M. Geib, C.I.H. Ashby, R.D. Twisten, O. Blum, H.Q. Hou, D.M. Follstaedt, B. Eugene Hammons, D. Mathes, and R. Hull. IEEE J. of Selected Topics in Quantum Electronics, 3 (3), 916-926, 1997.
- [6] T. Takamori, K. Takemasa, T. Kamijoh. Appl. Phys. Lett., 69 (5), 1996.

Acknowledgements:

The author is grateful to C.C. Lin, G. Solomon, and J.S. Harris for assistance and supervision in research as well as the Harris Group at Stanford University. Special thanks should also be given to SNF program coordinators Michael Deal and Jane Edwards. This work has been supported by the National Science Foundation and the National Nanofabrication Users Network.

Characterization of the Aspect Ratio Dependent Etch for Micro-Electromechanical Systems

REU Intern: James Williams, Engineering Physics, Santa Clara University

Principal Investigator: James McVittie, Department of Electrical Engineering, Stanford University, mcvittie@cis.stanford.edu

Abstract:

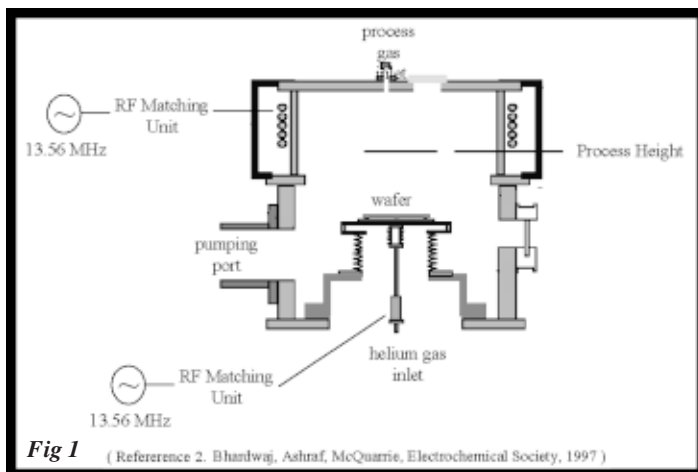
Measurements of the aspect ratio dependent etch associated with the STS Multiplex Inductively Coupled Plasma (ICP) Deep Reactive Ion Etching (DRIE) is critical to the fabrication of micro-electromechanical systems (MEMS). Calibration for three recipes, different geometric patterns and various die wafer densities will provide an etched chart with characterization of the etching by the STS Multiplex ICP Deep RIE. The etch profile's cross-sections were viewed on a scanning electron microscope (SEM). Results will provide characterization information to assist in the fabrication of MEMS.

Introduction:

A key technology for the fabrication of electrical through-wafer interconnects is deep silicon plasma etching. The characterization of a new commercial etching process (Inductively Coupled Plasma with Time-Multiplexing) capable of deeper and higher-aspect ratio etching is presented. While the definition of aspect ratio varies in the literature, this work will define aspect ratio of an etched hole as the final etched depth divided by the minimum feature size of the hole at the surface.

Traditionally, silicon etching is done in either a bath of wet chemicals, or in a dry reactive ion etcher. Both approaches have well characterized etch rates and standard masks. However, both approaches also have severe limitations when a deep, anisotropic, high-aspect ratio hole is required. To solve this limitation a method known as the Bosch process as been instituted in deep etching. At this time, it would be advantageous to discuss in brief how Inductively Coupled Plasma (ICP) and the Bosch process works.

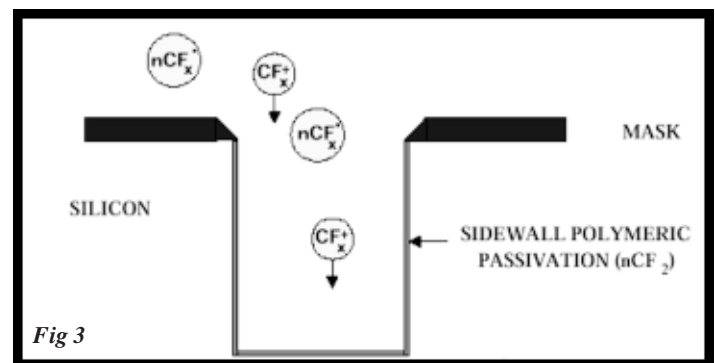
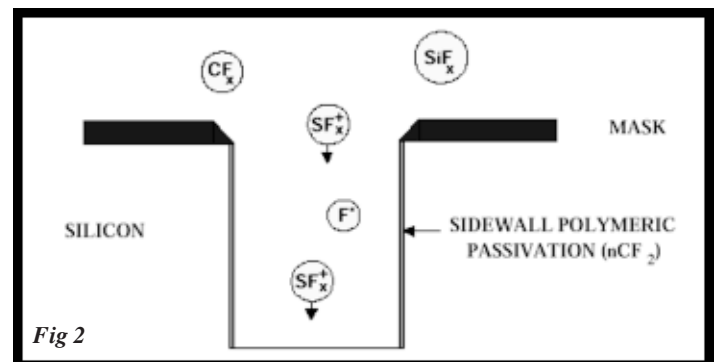
An Inductively Coupled Plasma etch machine is shown in Figure 1. On the sides, inductor coils are raised to high voltage controlled



by a RF source. This produces the plasma, and controls its density. A separate RF voltage attached to the wafer electrode controls the ion bombardment energy. By separately controlling the inductor and wafer bias, one can achieve high anisotropy in the etch.

The Bosch Process plasma etching process that permits very deep (up to through-wafer) high-aspect ratio holes (up to ~ 40:1) to be etched in silicon with only 20 μm of photoresist. Significantly higher aspect ratios are achieved by using a time-multiplexed process which continuously switches between passivation and etching steps. A fluorinated gas (SF_6) is used to etch the silicon (Figure 2), with a high top power for high etch rates ($> 600\text{W}$) and low bottom power (10W) to maintain excellent silicon to resist selectivity (60:1). After a few seconds, SF_6 is pumped out of the chamber and C_4F_8 pumped in. A thin Teflon like passivation layer is deposited on the wafer, including the base and sidewalls of the previously etched hole (Figure 3). Then SF_6 is pumped in again.

The fluorine radicals are able to break through the passivation more readily if they are ion-assisted. Since the bottom power drives ions vertically, the sidewalls are not bombarded directly, while the base of the hole is. Hence, the passivation is removed from the bottom of the hole first, and the fluorine attacks the silicon there.



This continued switching between passivation and etching steps permits increased anisotropy ($\sim 90^\circ$) with high-rates (1-5 $\mu\text{m}/\text{min}$). Stanford runs the BOSCH process on a commercial ICP etcher manufactured by Surface Technology Systems (STS). As a new tool on the market in 1997, new characterization data was needed to determine what its capabilities were for very deep silicon etching.

The goal of the experiment was to examine how the aspect ratio affects the etch rates and to provide a full characterization of different geometries and depths that they are etched to. All data will be plotted for easy use in the lab.

Experiment:

A test mask was prepared with various sizes of squares, rectangles and trenches. After etching labels into the silicon to aid in identification of the test structures, 10 μm photoresist masks were used to etch the test pattern in 500 μm . Three recipes provided by the manufacturer were used for varying etch times. All etches were made on the aforementioned STS DRIE machine. Die densities were also varied between 5 and 15%. After processing, the wafers were sawed and cleaved, and etch result cross-sections were viewed on a SEM. The depth vs. width of the trench, square and rectangle were plotted on a logarithmic scale (Figure 4).

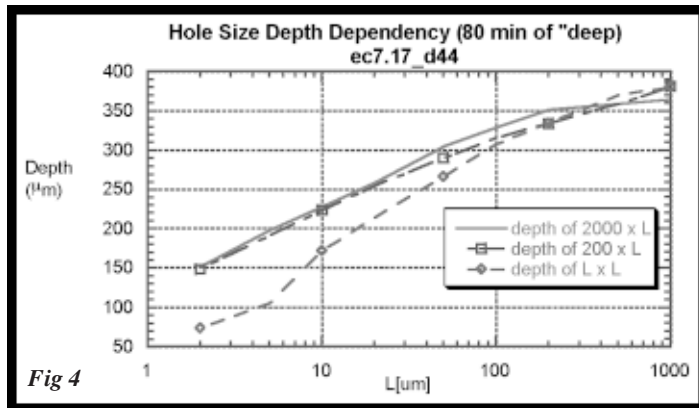


Fig 4

Results:

As in Figure 4, plots of the etch depth took on a linear trend on a log scale. Around 100 μm the lines flatten out and have a slope of approximately zero after that. As the aspect ratio decreases, the amount of fluorinated gas and ion flux accessible to the bottom of the trench decreases. This in turn reduces the amount of silicon that can be etched. Hence, the smaller the aspect ratio is, the slower and more shallow the etches are. In addition to aspect ratio characterization, effects of loading can be seen (Figure 5).

Loading occurs when the density of the die is increased thereby reducing the amount of fluorine gas that each trench can use. A complete table with all etch parameters will be graphed (loading and aspect ratio dependent etches) by October 2000.

Acknowledgements:

I would like to thank my mentor Eugene Chow for the wafer processing and SEM advice that he gave me over the summer. I would also like to thank Dr. James McVittie for guidance over the summer.

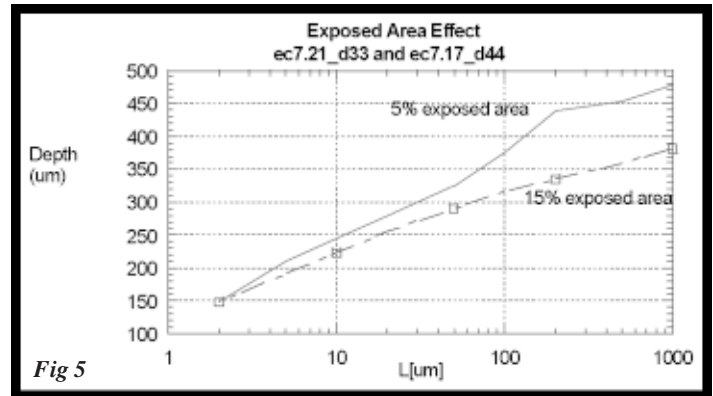


Fig 5

this page has intentionally been left blank

University of California Santa Barbara 2000 REU Participants



REU Intern

School Affiliation

Principal Investigator

Front Row:

| | | |
|-----------------------------------|--------------------------------|-----------------|
| Mr. Steven Charles | Brigham Young University | David Clarke |
| Mr. Jesus Angel Tena Guzman | UCSB | Umesh Mishra |
| Mr. Austin Brown | Harvey Mudd College | Elizabeth Gwinn |
| Ms. Nathalie Guébels | UCSB | David Awschalom |
| Mr. Christopher Utley | UCSB | Kimberly Turner |

Back Row:

| | | |
|--|--|--|
| Mr. Charlie Alexander Collins II | Lincoln University | Geoffrey Strouse |
| Mr. Alfred Flink | UCSB Quest | UCSB REU Mentor |
| Mr. Nicarter Gordon | University of the Virgin Islands | Samir Mitragotri |
| Ms. Evelyn Hu | UCSB | UCSB-Nanofabrication Facility Director |
| Ms. Kieche Meleson | UCSB | Jacob Israelachvili |
| Mr. Andrew Gapin | Georgia Inst of Technology | Pierre Petroff |

Spin Transport Across Interfaces

REU Intern: Austin Brown, Physics, Harvey Mudd College

Principal Investigator: Elisabeth Gwinn, Physics, UCSB, bgwinn@physics.ucsb.edu

Mentor: Ted Kreutz, Physics, UCSB

Abstract:

Producing and reading currents with coherent spin is the foundation of a new field known as “spintronics.” The aim is to inject carriers into a semiconductor substrate from a ferromagnet, which can act as a spin polarized source. The easiest way for a ferromagnet to be sufficiently spin-polarized is for it to be single domain, in which case all of its component atoms’ magnetic moments are aligned.

Investigating the problems associated with small magnet creation was the focus of this project. Manganese Arsenide, a room temperature ferromagnet, was grown on Gallium Arsenide by molecular beam epitaxy (MBE), then etched with photolithographic techniques to produce small, high aspect ratio (10:1) rectangular magnets. The domain structure was then investigated with magnetic force microscopy. Problems with processing prevented conclusive results until new samples are made, or a new technique is developed.

Procedures:

The Manganese Arsenide wafer was grown before my arrival, and we etched it soon after. The etching itself was done with a diluted 1 part HCl, 1 part HNO₃ solution. First, we spun photoresist on to the wafer, then exposed it to UV light and developed it to produce the array of magnets we wanted.

The first thing we noticed upon examining the etch under optical microscope was that the magnets appeared very rough and spotty. Also, some of the smaller magnets (less than 30 μm on the short side) were completely etched away.

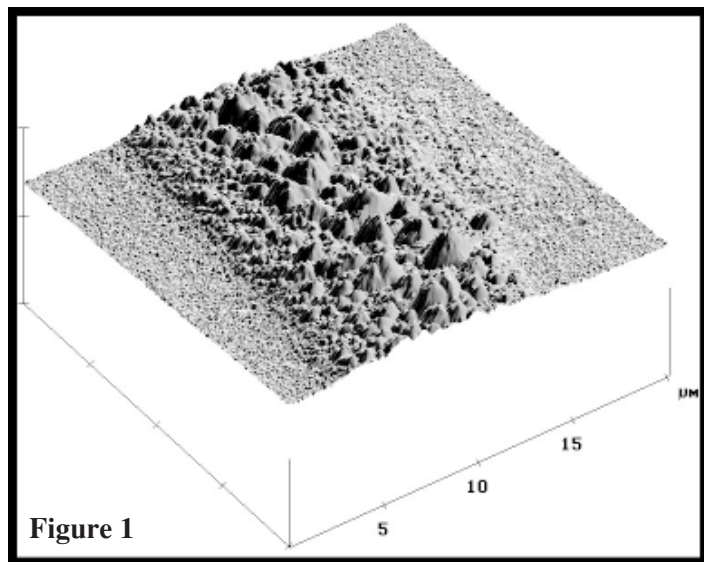
For magnetic analysis of the samples, I used a Digital Instruments atomic force microscope. The atomic force microscope functions by tapping the surface of the sample with a tip attached to an oscillating cantilever. The deflections of a laser reflecting off the tip translate into a height map of the surface. In this manner, high-resolution topographic maps of samples can be obtained.

For magnetic domain analysis, I used a magnetic tip in place of the standard tapping tips. Then, I ran the microscope in what is called interleaved mode. Basically, the tip makes two passes for each location: one in tapping mode to establish the topography, and then a second at a fixed height above the surface. Since the tip is magnetic, it feels a force from any magnetic field emitted by the sample. The cantilever oscillates like a spring, and the force either stiffens or relaxes it, changing its oscillating frequency.

The ideal data to take is a phase plot to correspond to the height plot of the same area. Each domain of a magnet will appear in the phase plot as a bright patch and a dark patch paired together, where the two patches are the poles of the domain. This is because the magnet will feel one kind of force when above one pole, and a

force in the opposite direction when over the other.

Resolution in magnetic force microscopy is usually limited by the lift height. Too large a lift height means that smaller features can’t be resolved, and the force felt is much weaker. Too small a lift height can result in crashing the magnet into the surface. I found that the best plots of our samples were taken with a lift height of about 35 nm, which is 15 nm above the minimum operating height.



Results and Conclusions:

A perspective view of one magnet is shown in figure 1, from which we can see the surface roughness. The height and phase plots of a section of the same magnet are shown in figures 2 and 3. The plot in figure 2 was taken on an upward pass of the microscope, and the one in figure 3 on a downward pass. The pattern of light and dark patches demonstrates that the magnets etched successfully were almost certainly not single domain. The height plot also reveals a roughness far in excess of what it was before etching. Furthermore, the disparity between the two (taken in succession) indicates that the magnetic tip was altering the sample.

Though the magnets we could examine were not single domain, their large size and relatively few domains implies that a smaller magnet may well be single domain with a similar growth and etching method. Further investigation is required in this matter.

For future work, the most important factor is to get better magnet etching. A different photolithographic process should be used,

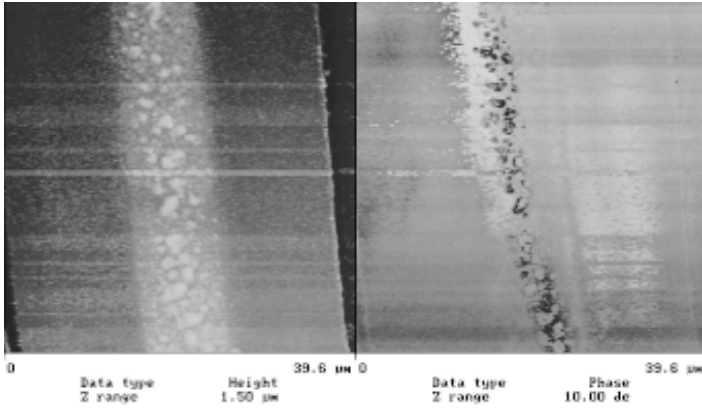


Figure 2: An upward pass of the microscope.

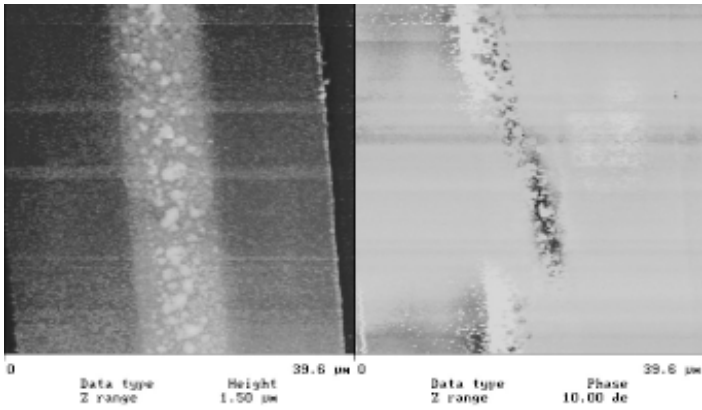


Figure 3: A downward pass of the microscope.

including different photoresist and etching solution. More successful etching would allow us to examine smaller magnets and reduce surface roughness, which obscures results with topographic effects. Others will continue to work on the etching process.

Another line of future work involves examining the magnet's behavior in an applied magnetic field. To this end, I constructed a platform to hold the sample in the microscope that has a small electromagnet on one end. Using this, it will be possible to apply a variable field and note the effects.

We would also like to investigate the effect of the tip on the sample. We have ordered several tips with varying strengths, and hopefully a lower magnetization tip will have less of a perturbing influence on the sample.

Acknowledgments:

I'd especially like to thank Professor Elisabeth Gwinn and my mentor, Ted Kreutz for their endless assistance and patience. Also, thanks to all of the folks in Gwinn Group (a.k.a. breakfast club) at UCSB for making work fun (and tasty).

Stress in Thick GaN-Films

REU Intern: Steven Charles, Mechanical Engineering, Brigham Young University

Principal Investigator: David Clarke, Materials Dept, UC Santa Barbara, clarke@engineering.ucsb.edu

Mentor: Ed Etzkorn, Materials Department, UC Santa Barbara

Abstract:

Thick GaN-films grown by heteroepitaxy are often subject to large biaxial stresses. Using Raman spectroscopy, a number of stress measurements were made on different films of varying thickness, crack density, and growth technique. Most notably, it was determined that while MOCVD templates are in more compression than are HVPE templates, thick films grown on MOCVD and HVPE templates exhibit no difference in stress. In addition, it is shown that for thick films grown on HVPE templates, the film is under more compression at the interface than at the free surface.

Introduction:

As a wide-bandgap III-V semiconductor material, GaN (gallium nitride) has found many applications in electronic and optical devices. Thin GaN films are used in blue and green LED's, and it is currently possible to grow thin GaN-films ($< 5 \mu\text{m}$) with excellent material properties. For many applications, however, including blue lasers, use of a thick GaN-layer as a growth-template (5-200 μm) would improve device performance. Many thick films exhibit large biaxial stresses, causing degradation in the film's electronic and mechanical properties.

One such degradation is crack formation, which impairs the flow of carriers and decreases the film's structural stability. In an ongoing effort to understand the development of stresses in thick GaN-films, a number of different Raman spectroscopy measurements were made of the shift in the E_2 phonon peak. There have been efforts to correlate this shift to the actual stresses present in the sample.

One correlation was established in 1998 in our laboratory to be approx. $4.4 \text{ cm}^{-1}/\text{GPa}$ [1]. Also in 1998, Ager et al. proposed a lower value of approx. $2.4 \text{ cm}^{-1}/\text{GPa}$ [2]. Because this correlation is still under investigation, little attempt is made in this paper to relate the measured E_2 peak shifts to stress. Below is a brief description of the experimental procedures and results of four of these measurements.

Experimental Procedure and Results:

1) MOCVD vs. HVPE:

a) A thick film grown by HVPE on an MOCVD template was compared to a thick film grown by HVPE on an HVPE template. Using Raman spectroscopy, it was found that there was no detectable difference in the shift of the E_2 phonon peaks of the two samples, indicating that there is no stress difference between the two samples. However, a statistical difference was detected in the full width at

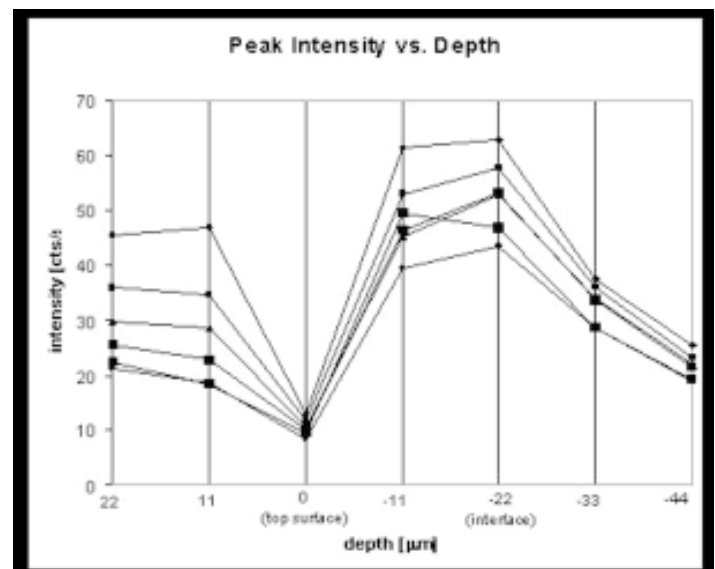
half maximum (FWHM) of the E_2 peaks. It was found that the FWHM of the E_2 peak of the film grown on the MOCVD template was larger than that of the film grown on the HVPE template by $0.178 \pm 0.057 \text{ Rcm}^{-1}$, signifying that there may be a difference in the stress gradient.

b) An MOCVD template was compared to an HVPE template. Raman spectroscopy measurements on the top surface showed that the shift of the E_2 peak of the MOCVD template was greater than that of the HVPE template by $1.404 \pm 0.064 \text{ Rcm}^{-1}$, meaning that the MOCVD template is in more compression by $320 \pm 15 \text{ MPa}$ (using the shift-stress relationship from our lab). In addition, the FWHM of the E_2 peak of the MOCVD template was found to be smaller than that of the HVPE template by $0.9 \pm 0.1 \text{ Rcm}^{-1}$.

2) Stress Variation Through the Film Thickness:

By focusing on sequentially lower layers, starting above the film surface and descending beyond the film-substrate interface into the substrate, the variation of stress throughout the thickness of a film was determined. The film under investigation was a $22 \mu\text{m}$ thick, largely uncracked film grown by HVPE. Raman measurements were taken from $22 \mu\text{m}$ above the film surface to $22 \mu\text{m}$ below the film-substrate interface, in $11 \mu\text{m}$ intervals.

It was found that the E_2 peaks of the measurements taken on the top surface were less shifted than those taken at the film-substrate interface by $0.249 \pm 0.035 \text{ Rcm}^{-1}$, meaning that the top surface is



under less compression than the film-substrate interface. Also, an abnormality in the behavior of the peak intensity was observed (Figure 1 shows measurements at 6 different spots on the sample).

Not only does the peak intensity drop to a minimum at the top surface of the film, but the spread of intensities of different measurements is also a minimum there. To our knowledge, there is currently no satisfactory explanation for this behavior, and further investigation is underway.

3) Cracked vs. Uncracked:

A thick, relatively uncracked film was compared to a thick, heavily cracked film. Both films were grown by HVPE on sapphire substrates. Raman spectroscopy measurements on the top surface showed that the shift of the E_2 peak of the cracked film was greater than that of the uncracked film by $0.56 \pm 0.06 \text{ Rcm}^{-1}$, corresponding to higher compressive stresses in the cracked film. However, due to the large number of parameters involved in the growth of the two samples, further investigations are necessary to confirm this correlation between crack density and stress at the film surface.

Conclusions:

We have demonstrated that there is a definite difference in stress between MOCVD and HVPE templates, and that MOCVD templates exhibit larger compressive stresses than HVPE templates. This means that HVPE films experience larger tensile stresses during growth, which may account for the higher cracking densities observed in HVPE films. However, once thick films are grown on top of these templates, there is no longer a detectable difference in stress at the free surface. Also, we have demonstrated that in thick GaN-films grown by HVPE, compressive stresses found at the film-substrate interface tend to relax toward the film surface. Furthermore, the anomalous intensity behavior discussed above suggests that further thickness measurements are necessary to accurately interpret the sample-probe interaction of Raman spectroscopy on GaN films.

Acknowledgements:

Funding from the National Science Foundation.

References:

- [1] "Laser Enhanced Debonding of Nitride Semiconductor Films", Lezlie Potter (Advising Professor: Dr. David Clarke). Materials Dept., University of California at Santa Barbara, 1998.
- [2] "Stress Gradients in Heteroepitaxial Gallium Nitride Films", J. W. Ager III, G. Conti, L. T. Romano, and C. Kisielowski. Nitride Semiconductors Symposium, Materials Research Society, Pittsburgh, 1998. pp. 769-774.

Synthesis and Characterization of Low-Dimensional Materials Using Non-Lithographic Techniques

REU Intern: Charlies A. Collins II, Chemistry, Lincoln University, Pennsylvania

Principal Investigator: Geoff Strouse, Chemistry, UC Santa Barbara, strouse@chem.ucsb.edu

Mentor: Khalid Hanif, Chemistry, University of California Santa Barbara

Abstract:

The focus of this project is to synthesize and characterize Cadmium Selenide (CdSe) quantum dots and dope them with different metals (Eu, Mg, Cu, etc.). Doping controls the optical and magnetic properties of these metals. If there is a magnetic spin then these doped CdSe quantum dots can be useful in computers for data storage in the future.

Introduction:

Nanotechnology is a new term that was used no more than 13 years ago, but the prediction of its creator, Eric Drexler, was ahead of his time. He predicted that factory production lines would be replaced by self-regenerating nanoscale 'assemblers' and that humans would be the dominant life forms of the entire planet. But in the new millenium, nanotechnology has taken the science field by storm and it is just getting started.

My research is just one of the many new and groundbreaking techniques of nanotechnology in this millenium. By using an organometallic process, one can make very small particles that can be used in electronics. Then, one is able to dope these small particles — quantum dots — with metals to control their precise arrangements in space. This type of nanotechnology can help with a consumer's craving appetite for larger data storage capabilities within computers.

Experimental Procedures:

In order to make the CdSe quantum dot; one has to make the $(\text{Me}_4\text{N})_4[\text{Se}_4\text{Cd}_{10}(\text{SPh})_{16}]$ precursor.

$(\text{Me}_4\text{N})_2[\text{Cd}_4(\text{SPh})_{10}]$

- Place 21 grams of Cadmium nitrate tetrahydrate in methanol (60 ml) and add to a well-stirred solution of benzenethiol (19ml) and triethylamine (25ml) in methanol (60ml) at room temperature.
- Followed by the addition of a solution of tetramethylammonium chloride (8.4g) in methanol (40ml).
- Stir the mixture until all precipitates have dissolved, then let stand undisturbed at 0°C.
- Pour crystals into filter and wash the crystals with methanol and ethyl ether.
- Transfer the crystals to a round-bottom flask and vacuum the sample.

$(\text{Me}_4\text{N})_4[\text{Se}_4\text{Cd}_{10}(\text{SPh})_{16}]$

- Place black selenium powder (.701g) to a one-portion solution

of the $(\text{Me}_4\text{N})_2[\text{Cd}_4(\text{SPh})_{10}]$ (15g) in acetonitrile (20ml) and let it stir for about three hours.

- After the three hours, heat the mixture to 75°C and add acetonitrile until all solid has dissolved (leaving a yellowish solution).
- The yellow solution is then allowed to cool slowly. Rotovap this yellowish solution, leaving only small amount of solution and a white solid.
- Filter through, wash with acetonitrile, and vacuum dry the white solid.

CdSe Quantum Dots Doped with Cu:

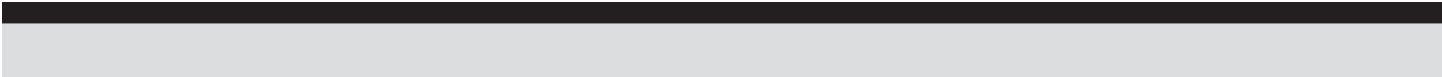
- Measure out $(\text{Me}_4\text{N})_4[\text{Se}_4\text{Cd}_{10}(\text{SPh})_{16}]$ (~ 2g) and place in a three-neck round bottom flask with 2/3 of it filled with 1-Hexadecylamine (HDA).
- Heat the reaction (slowly), then place about 1/10 the amount of Copper to the amount of $(\text{Me}_4\text{N})_4[\text{Se}_4\text{Cd}_{10}(\text{SPh})_{16}]$ in reaction.
- After the reaction has reached the 160°C, take samples of the reaction to do different characterizations of the CdSe quantum dots.

Results and Conclusion:

The results of my research shows that I have successfully made the CdSe quantum dots, while at the same time showing that I have also doped them with the Copper metal. This research is very helpful within the group in determining what metals would be good doping materials with the CdSe quantum dots. Now more extensive research can be done in trying to get these dots to be size selective and to see how much magnetic spin these doped dots have.

The instruments that can be used for characterization of the CdSe quantum dots are Transmission Electron Microscopy (TEM), Emissions, Absorption, X-ray powder diffraction, Superconducting Quantum Interference Device (SQUID), Atomic Absorption and Electron Paramagnetic Resonance (EPR). These instruments determine the size, size distribution, band gaps, amount of defects, doping structure, crystallinity and even magnetic properties.

Considering the length of time to perform this type of research, one had to work diligently in trying to assist in the cause of this groundbreaking research. Yet, researchers continue to work on these problems, no matter how time-consuming or daunting to come up with results that can be used in today's high-tech world. Eventually, researchers will be able to use this research to set the foundation in nanotechnology and take us into the 22nd Century.



Acknowledgements:

Dr. Geoff Strouse and the entire Strouse Research Group.

(No photographs were provided for this report.)

Fabrication of Ordered Arrays of InAs Quantum Dots

REU Intern: Andrew Gapin, Materials Engineering, Georgia Tech

Principal Investigator: Pierre Petroff, Materials Engineering, UCSB, petroff@engineering.ucsb.edu

Mentor: Brian Gerardot, Materials Engineering, UCSB, gerardot@engineering.ucsb.edu

Abstract:

The objective of this project is to examine the nucleation of InAs quantum dots on a patterned GaAs substrate. The sample was prepared by first placing a square pattern of depressions approximately 50 nm deep and 100 nm wide spaced 4 μm apart on the GaAs substrate using electron beam lithography. Following patterning, the InAs quantum dots were grown by the Stranski-Krastanow method using molecular beam epitaxy. After preparation the samples were examined with an atomic force microscope using the tapping mode. Statistics were then taken on the number of quantum dots present in each depression in reference to the depression position within the sample.

Evaluation of the data indicates that the quantum dots tended to form preferentially toward the center of the sample. This was contrary to previous research that showed that the quantum dots tend to concentrate more toward the edges of the sample. Upon further examination this inconsistency was most likely caused by a particularly large concentration of defects on the sample surface which function as sites for preferential nucleation of the quantum dots.

Introduction:

Quantum dots (QDs) are small regions of a narrow band gap material sandwiched by a wide band gap material that can confine electrons. Typically, QDs are on the order of 10-20 nm high by 30-100 nm in diameter and they contain a specific number of electrons in well-defined energy states. Due to their behavior, quantum dots are often referred to as artificial atoms because they function similarly to way an individual atom would. Research in this area has indicated that QDs may have the potential to dramatically increase the efficiency of electronic devices while simultaneously allowing for a reduction in size. For this reason, QDs have recently become the focus of many research efforts to study the mechanisms of their formation since that knowledge would be crucial to the production of any devices utilizing quantum dot technology.

Procedure:

The sample that was examined in this project contained a GaAs substrate with depressions in which the InAs quantum dots form. The depressions were formed in the GaAs substrate using electron beam lithography. In the sample that was examined for this project, a 76 μm square pattern of depressions with a spacing of 4 μm was formed. After the surface of the sample was patterned in this manner, the quantum dots were grown with molecular beam epitaxy using the Stranski-Krastanow method. Once the sample was produced, it

was examined using an atomic force microscope (AFM) in tapping mode. Square 8 μm images of the sample showing four depressions at a time were taken over various positions on the sample. Two sample images of these scans are shown in Figures 1 and 2. Statistics were then compiled on the concentration of quantum dots in the depressions according to the depression position in the sample.

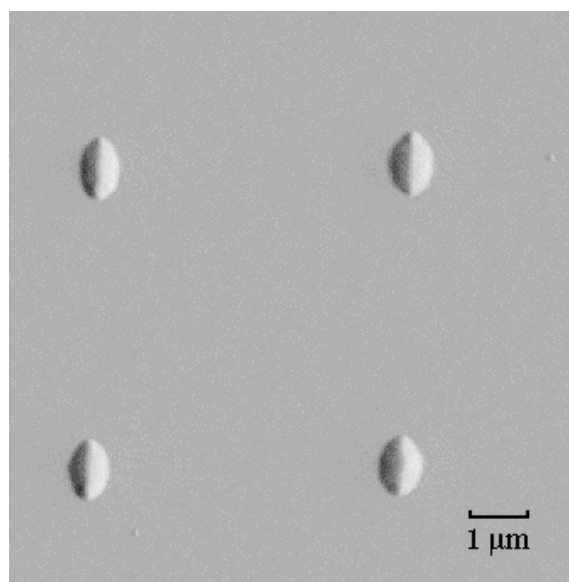


Figure 1: 8 μm AFM amplitude image of four depressions without QDs

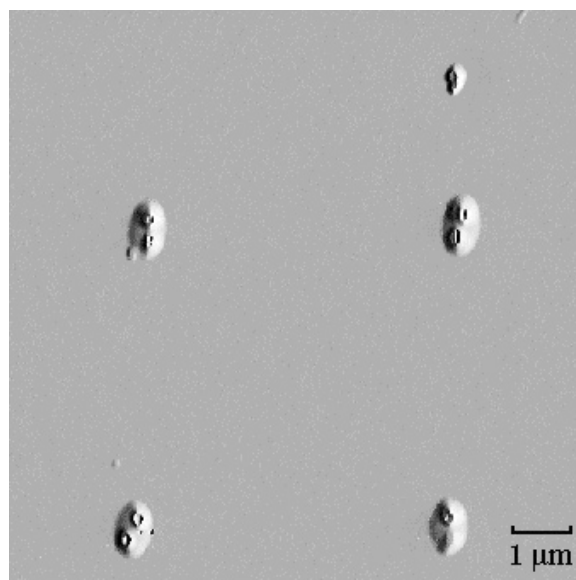


Figure 2: 8 μm AFM amplitude image showing nucleation of QDs within the depressions

Results and Conclusions:

The statistics that were gathered on the quantum dot concentration within the depressions showed that there tended to be more quantum dots present in the depressions toward the center of sample than there were at the edges. After compiling all the statistical data, the surface map of the sample, shown in Figure 3, was produced.

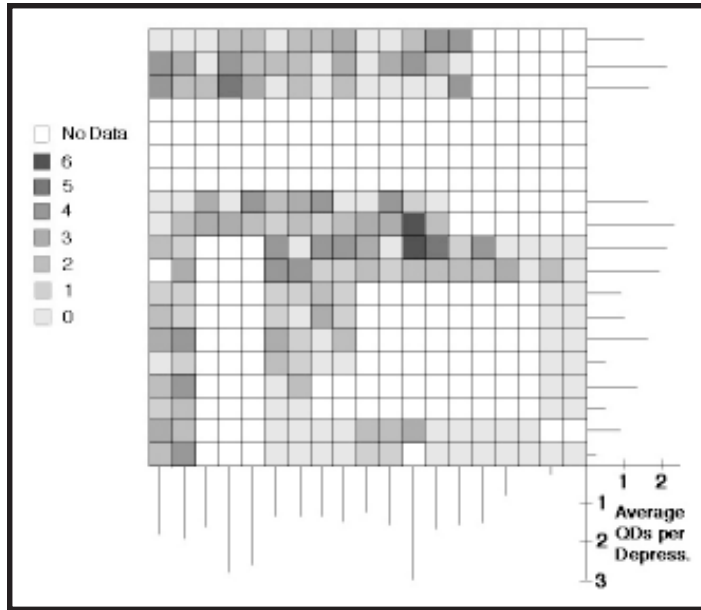


Figure 3: Surface map of the sample showing the concentration of QDs within the depressions

Figure 3 represents data from 48% of the sample surface and the data appears to be consistent as a general trend can be seen. By looking at the chart, it is seen that there are more depressions without any quantum dots on the right edge and bottom of the sample. As the depression position moves more toward the center of the sample, there is a larger concentration of QDs per depression — several depressions had four, five, or six quantum dots. The bar graphs on the right and bottom edges of the chart indicate the average number of quantum dots per depression for the respective row or column of depressions. This too shows the larger concentration of QDs at the center of the sample.

The results of this project were rather disappointing because they conflicted with results from previous research. The work from the previous research indicated that more quantum dots form preferentially at the edges of the sample compared to at the center. Table 1 shows a comparison between the statistical data from the sample that was examined in this project with that of a sample with a depression spacing of $1\ \mu\text{m}$ that was examined in the previous research.

Table 1: Comparison of Results to Previous Research

| | | |
|---------------------------------------|--------------------------------|--------------------------------|
| Depression Spacing | $1\ \mu\text{m}$ Spacing | $4\ \mu\text{m}$ Spacing |
| Average # of Dots per Depression | 7.70 | 1.53 |
| Standard Deviation | 2.24 | 1.52 |
| Edge to Center Ratio | 1.20 | 0.61 |

In examining the images that were taken with the AFM, it can be seen that in many of the regions there are a large number of defects on the sample surface between the depressions. There are regions on the sample where there are defects containing quantum dots that are located right next to empty depressions. Figure 4 shows an AFM image of one of these types of regions.

Analysis of all the AFM images indicates that the defects act as preferential nucleation sites for the quantum dots because they contain a larger chemical potential gradient than the depressions for the indium atoms. This just emphasizes the important dependence that quantum dot formation has on thermodynamics and the difficulties that are inherent in producing devices that utilize quantum dot technology.

Acknowledgements:

First, I would like to thank Dr. Petroff for selecting me to participate in the NNUN program and to work in his laboratory at UCSB this summer. I would also like to thank my mentor Brian Gerardot who helped me through my work this summer and provided much support in helping me to understand what I was working on. Brian also helped me to adjust to life at UCSB allowing me to have a very fun summer in Santa Barbara.

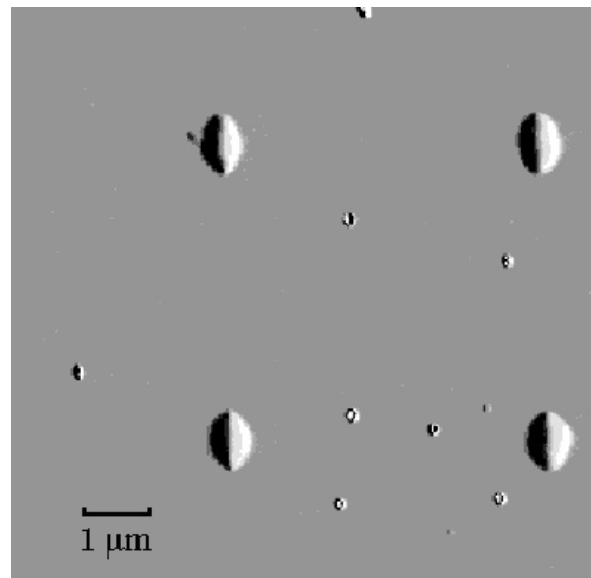


Figure 4: $8\ \mu\text{m}$ AFM amplitude image showing QD formation in defects.

Self Assembled Monolayers of Alkanethiols on Gold Substrates

REU Intern: Nicarter Gordon, Biology, University of the Virgin Islands

Principal Investigator: Samir Mitragotri, Chemical Engineering, UCSB, samir@engineering.ucsb.edu

Mentors: Jagganathan Sunduram, Ahmet Tezel, UCSB

Abstract:

Self assembled monolayers (SAMs) are molecular units that are spontaneously formed upon certain substrates such as Au, Si, etc, when immersed in an organic solvent. When formed, these SAMs have very unique surface properties that are able to be changed whenever needed. The intended purpose of our research is in creating SAMs for use as a drug delivery mechanism when appropriately needed. The drugs will be released with the application of an electric potential.

The focus of my research was in standardizing the technique in making these alkanethiol monolayers so that we could always get reproducible results. We used gold deposited on silicon as a substrate for the monolayers to assemble upon. They were then cleaned with a strong oxidizer. The Au/Si wafer were immersed in a solvent solution with alkanethiols ranging in length from C₁₀, C₁₁, and C₁₆, then set for 24 hours for adhesion to Au surface.

Introduction:

Surface engineering is a field that has brought us many advancements in technology today. We take for granted things such as light induced surfaces, pH switchable ordered monolayers and photo switchable biomaterials which were made possible through the hard work of surface engineers. Today, most organic thin films that are used in technology have predetermined surfaces. Therefore much research is currently moving ahead in developing “novel surfaces” that are able to be changed. The medical field could benefit tremendously from this field due to novel methods of delivering drugs whenever necessary.

Now it has been observed that monolayers can spontaneously form when certain substrates are immersed in an organic solvent containing active surfactants. A monolayer is an assembly of molecules that is basically one molecular layer thick. The monolayer is composed of an ordered array of molecules that is densely packed. The typical molecule in a monolayer has three parts. The head group which attaches itself to a substrate, the alkyl chains which are hydrophobic, and a terminal group upon which

drugs could be attached to. Order and proper length of the alkyl chains are very important issues when it comes to producing these monolayers. Shorter chains tend to be less ordered while longer chains tend to be harder to bend. These factors are important in that an ordered array of molecules with sufficient ease in bending would be necessary if an electric potential was used in order to release drugs.

Procedures:

First, 1000 Å of gold deposited on silicon substrates were cleaned with pirana solution in order to remove any form of organic contaminants. Then vials were vacuumed and cleaned with Ar. The Au/Si wafers were carefully placed inside of these vials. Then the vials were filled with ethanol through Ar displacement. Alkanethiols of C-10, C-11, and C-16 were weighed out and then placed in vials that were labeled with their lengths. The bottles were then left for 24 hours for the monolayers to adsorb itself to the surface.

After 24 hours the wafers were removed from the vials and washed with ethanol as to remove any extra monolayers that may have formed upon each other. The wafers were then put back into a bottle with fresh ethanol and taken to an ellipsometer and a gnomometer to show the existence of a monolayer by measuring parameters involving thickness and orientation.

Results:

Ellipsometry was used to measure the length of alkanethiols to see if its length agreed with what other scientists reported in previous literature. The values for the ellipsometry had a margin of error of plus or minus two. From ellipsometry data, with the exception of the first sample, the values that we got for the C-10 alkanethiol agreed with the values that were reported in literature. However, all of the samples of C-11 alkanethiol gave unexpectedly low values. The C-16 values also tended to agree more with what scientists in the field had gotten as result.

Table 1: Ellipsometric Data.

| CARBON CHAIN | EXPECTED VALUES | SAMPLE: | | |
|--------------|-----------------|---------|--------|---------|
| | | 1 | 2 | 3 |
| C10 | 15Å | 9 Å (*) | 13Å | 13Å |
| C11 | 17Å | 10Å (*) | 7Å (*) | 10Å (*) |
| C16 | 22Å | 23Å | 25Å | 19Å |

(* = Unexpected values.)

Table 2: Contact Angles.

| SAMPLES | Qa | Qs | Qr |
|---------|-----|-----|----|
| C10-1 | 100 | 100 | 51 |
| C10-2 | 102 | 99 | 89 |
| C10-3 | 100 | 98 | 51 |

Contact angles were used to measure how close the advancing angle of droplet water on the wafer got to 110 degrees due to the hydrophobic carbon chains. The closer that the angle was to 110 degrees the better was the formation of the monolayer. The data that we got for the C-10 alkanethiols agreed with the fact that the monolayers were very hydrophobic because their Q_a were all close to 110 degrees. The C-11 samples continued to show problems because their Q_a were far less than 110 degrees. The C-16 samples had Q_a values that were lower than the C-10 values possibly because they along with C-11 samples had acidic terminal groups.

Table 3: Contact Angles.

| SAMPLES | Q_a | Q_s | Q_r |
|-------------|----------|----------|-------|
| C11-1 | 75 | 30 | 10 |
| C11-2 | 40 | 35 | 2 |

Conclusion:

1. The ellipsometry results with the exception of the C-10 molecule agreed with the literature values.
2. The contact angle results also agreed with the literature values.
3. We plan to use AFM to further measure the monolayer.
4. In the future, we intend to use various chemicals that form monolayers in the hopes of bending them with the application of an electric potential.

Acknowledgements:

I would like to give special thanks to the following people:

1. Samir Mitragotri, Advisor
2. Jaganathan Sunduram, Mentor
3. Ahmet Tezel, Grad. Student

Table 4: Contact Angles.

| SAMPLES | Q_a | Q_s | Q_r |
|-------------|----------|----------|-------|
| C16-1 | 90 | 69 | 45 |
| C16-2 | 85 | 75 | 50 |
| C16-3 | 70 | 37 | 25 |

(No photographs were provided for this report.)

Ferromagnetic Clusters and Annealed GaMnAs

REU Intern: Nathalie Guébels, Electrical Engineering, University of California, Santa Barbara

Principal Investigator: David Awschalom, Department of Physics, UCSB, awsch@physics.ucsb.edu

Mentors: Roland Kawakami, Ezekiel Johnston-Halperin, Department of Physics, UCSB

Abstract:

Ferromagnetic clusters within a GaAs host are obtained by annealing a (Ga,Mn)As digital superlattice. Characterization by x-ray diffraction (XRD) demonstrates structural changes after annealing, and superconducting quantum interference device (SQUID) magnetometry reveals an increase in Curie temperature (T_c) to 325°C after annealing for 10s at 850°C. This suggests the possibility of obtaining room temperature ferromagnetism in an ordered array of clusters.

Introduction:

For the past 50 years, semiconductors have been used for a variety of applications based on the manipulation of electronic charge. Ferromagnetic semiconductors have recently received attention for their promise of integrating this versatility with traditional magnetism based applications such as non-volatile memory. However, much remains to be learned about these materials in order to realize this goal. With this motivation, the aim of this project is to investigate assemblies of ferromagnetic clusters within a GaAs host. Ferromagnetic clusters were generated by rapid thermal annealing (RTA) of (Ga,Mn)As digital ferromagnetic heterostructures (DFH) [1] and characterized using x-ray diffraction (XRD) and superconducting quantum interference device (SQUID) magnetometry.

The DFH samples used here are grown via molecular beam epitaxy at substrate temperatures of 280°C by depositing λ ML of MnAs followed by several ML of GaAs forming a superlattice structure. We use the notation $(10,0.5)_{100}$ to refer to a 10 ML GaAs spacer separating λ ML of MnAs repeated for 100 periods.

In this study, templates of $(10,0.5)_{100}$, $(50,0.5)_{20}$, and $(100,0.5)_{10}$ are used for annealing. In contrast to previous work [2-3], the DFH template presents the possibility of controlling the ordering of clusters along the growth direction.

Clusters are generated by RTA. This technique consists of rapidly heating (200°C/s) and cooling (40°C/s) the template. Annealing temperatures are varied between 300°C and 850°C and the duration of the anneal is varied between 10 seconds and 7.5 minutes in a forming gas environment (90% N_2 , 10% H_2). During the anneals, the samples are covered with GaAs substrates to avoid As loss. We annealed a total of 24 samples with the best results obtained at higher annealing temperatures (750°C and 850°C) for an annealing time of 10 seconds.

X-ray diffraction is used to determine structural changes due to annealing. The peak positions give the periodicity of the crystal structure and therefore the lattice spacing of the atoms within the structure as well as the superlattice spacing (labeled ± 1 in Fig. 1).

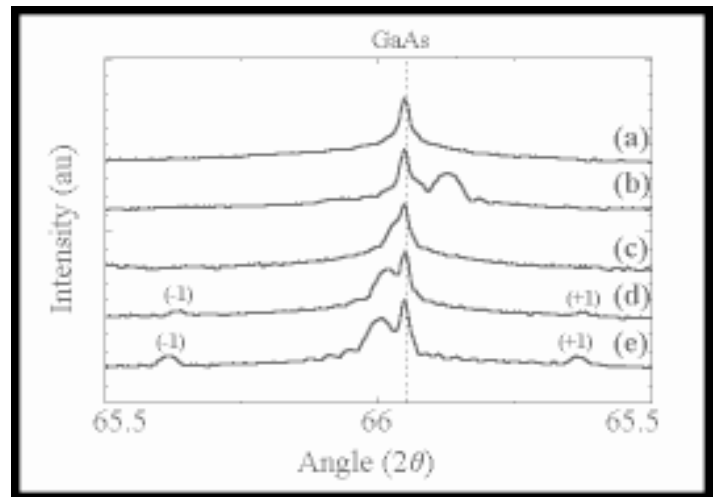


Figure 1: θ - 2θ XRD scan of a $(100,0.5)_{10}$ DFH before and after annealing for 10s. (a) annealed at 850°C, (b) annealed at 750°C, (c) annealed at 650°C, (d) annealed at 550°C, and (e) unannealed.

X-ray data taken on the annealed samples suggests structural changes after annealing. At higher annealing temperatures the superlattice peaks disappear and the central DFH peak approaches the substrate peak, suggesting a reduction in strain as As is taken out of the lattice.

Results and Conclusions:

As previous studies indicate that the DFH structures are ferromagnetic [1], SQUID magnetometry is used to investigate the magnetic properties of the annealed samples in contrast to the unannealed templates. To investigate the temperature dependence of the magnetization of the annealed samples, the magnetization is measured as the temperature is varied from 5 to 340K. The data reveal an increase in Curie temperature (T_c) with increasing annealing temperature. Figures 2 (a), (b) and (c) show T_c of 50K, 284K and 325K for anneals of 10s at 650°C, 750°C and 850°C, respectively.

This reveals a T_c almost 300K higher than in the unannealed samples ($T_c \sim 50$ K) for the highest temperature anneal. Given the T_c of MnAs is 318 K and of GaMn is higher than 400K, Figure 2b strongly suggests the presence of ferromagnetic clusters of either or both these materials.

Hysteresis loops are also measured for samples annealed at 400°C, 750°C and 850°C at a temperature of 5 K. The loops of the annealed structures demonstrate hysteresis, with the magnetic field applied along the (100) in-plane axis (Figure 3).

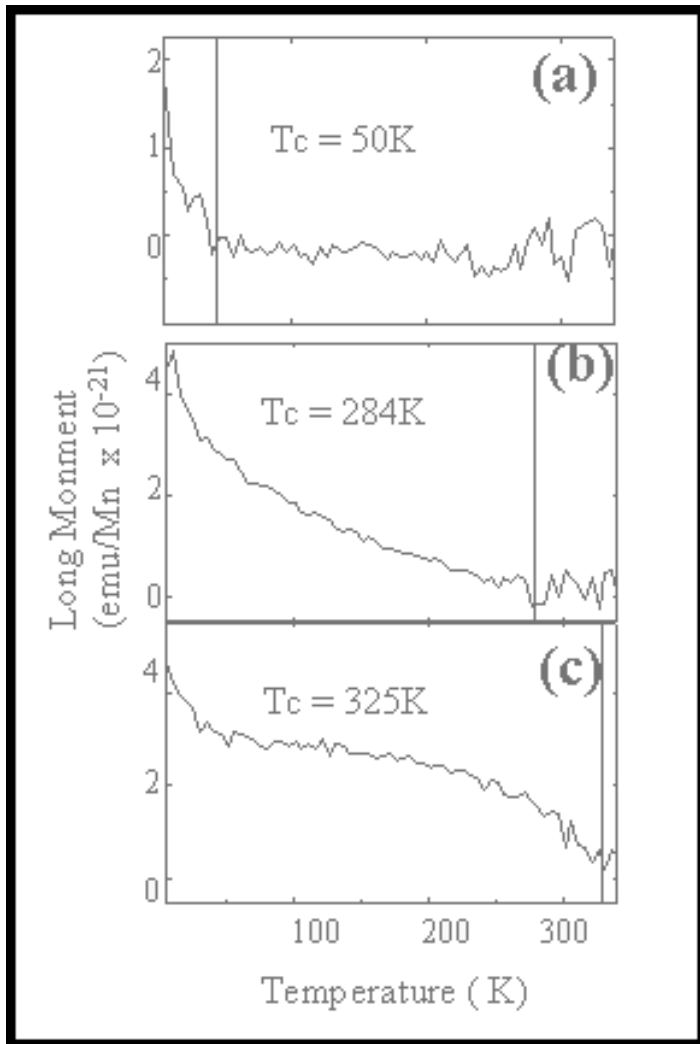


Figure 2: Increasing T_c after annealing a $(50,0.5)_{20}$ DFH for 10s at (a) 650°C, (b) 750°C and (c) 850°C.

Differences between the annealed and unannealed samples may be due to either a change in easy axis orientation upon annealing and/or inhomogeneity in the cluster size.

Future plans include continued investigation of the microscopic structure through XRD, cross-sectional transmission electron microscopy, and atomic force microscopy; and investigation of the magnetic properties using SQUID and magnetic force microscopy. Additionally, as several annealing recipes yielded T_c of room temperature or higher, these structures may be interesting for future device applications such as giant magneto-resistance based devices and spin manipulation.

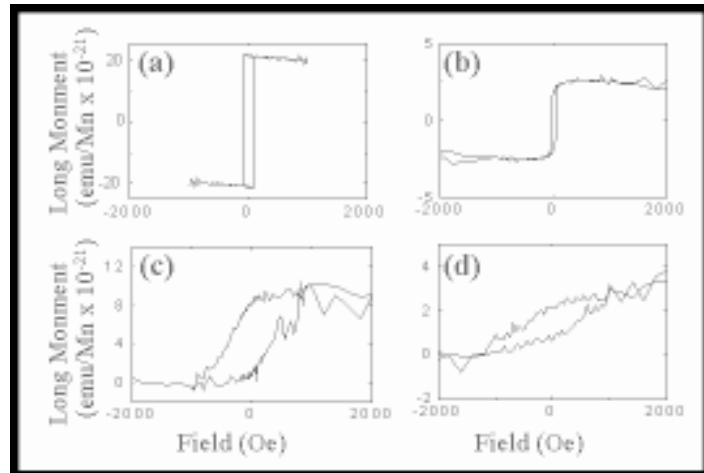


Figure 3: In-plane SQUID hysteresis loops taken at $T = 5K$ for (a) $(10,0.5)_{100}$ DFH unannealed, (b) $(10,0.5)_{100}$ DFH annealed for 30s at 400°C, (c) $(50,0.5)_{20}$ DFH annealed for 10s at 750°C, (d) $(50,0.5)_{20}$ DFH annealed for 10s at 850°C.

All structures show hysteresis, demonstrating ferromagnetism.

References:

- [1] Kawakami et al., Appl. Phys. Lett. (submitted).
- [2] Shi et al., Nature 377, 707 (1995).
- [3] Wellmann et al., Appl. Phys. Lett. 71, 2532 (1997)

Acknowledgements:

I would like to thank Noey Turk, and everyone from Quest and NNUN for all the help and good advice and for making this summer very instructive and enjoyable. This work was supported by the NSF and DARPA/ONR N00014-99-1-1096.

Characterization of InGaAs Oxide Aperture HBTs

REU Intern: Jesus Guzman, Electrical Engineering, UC Santa Barbara

Principal Investigator: Umesh Mishra, Electrical Engineering, UC Santa Barbara, Mishra@ece.ucsb.edu

Mentor: James Champlain, Electrical Engineering, UC Santa Barbara, Jgchamp@indy.ece.ucsb.edu

Abstract:

The purpose of this project is to design a new Heterojunction Bipolar Transistor (HBT) with a high switching speed. The devices were designed in a collector-up configuration which is intended to reduce the base collector capacitance (C_{BC}). However, collector-up devices suffer from increased recombination in the base and to counteract this undesired effect an oxide aperture was introduced in the emitter.

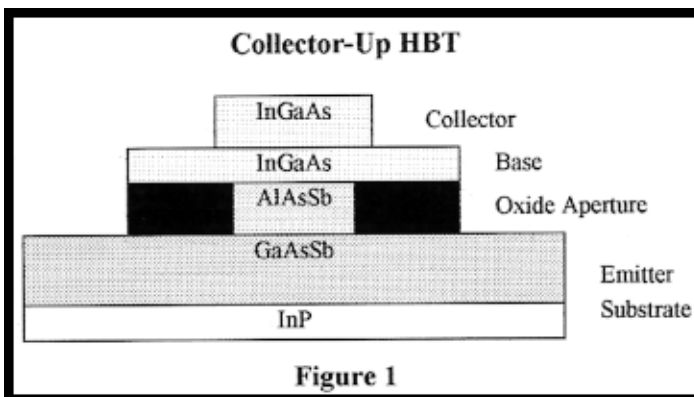
The HBTs were grown with InGaAs in the base and collector, and a two-stage emitter which consisted of AlAsSb in the first stage and GaAsSb in the second stage. AlAsSb was used to form the oxide aperture since it is easily oxidized. After testing the first batch of HBTs, it was found that they are not operating properly since the gain was constantly measured at less than unity.

Introduction:

This project is aimed at developing a new Heterojunction Bipolar Transistor (HBT) with a high switching speed. A high switching speed HBT can be used for a variety of purposes, including high frequency receivers and DACs. To increase the switching speed, it was attempted to reduce the base collector capacitance (C_{BC}). The designed HBT would also have a low power/low voltage requirement to make it adequate for use in portable electronics. For this reason, the materials chosen to grow the device were InGaAs and GaAsSb which are small bandgap materials.

HBT Design:

Since one of the main concerns was to reduce the base collector capacitance, it was decided that the HBT would be grown in a collector-up configuration which means that the collector is physically on top (see Figure 1 below). This configuration has a smaller base collector junction area and C_{BC} is reduced because capacitance is proportional to the junction area.



Although collector-up devices have been investigated in the past, they are not widely used because they suffer from higher recombination in the base which reduces the current gain. To circumvent this drawback, the concept of an oxide aperture in the Collector-Up HBT emitter was considered. As shown in Figure 1, the purpose of the oxide aperture is to make the base emitter junction smaller than or equal to the base collector junction so that the electron flow is limited by the size of the base emitter junction. The collector and the base were made with $\text{In}_{0.53}\text{Ga}_{0.47}\text{As}$ and the emitter with $\text{AlAs}_{0.56}\text{Sb}_{0.44}$ and $\text{GaAs}_{0.49}\text{Sb}_{0.51}$.

Procedure:

The HBTs were made using conventional photolithography techniques with a wet etch. The special step in the procedure would be the formation of the oxide aperture which was easily done by steam oxidization of the AlAsSb into Al_2O_3 in the furnace at a temperature of 325°C . When the first batch of devices was finished it was time to test them. There are two figures of merit for high-speed HBTs and they are the Current Gain Cutoff Frequency (f_T) and the Maximum Frequency of Oscillation (f_{max}) which are shown in Figure 2 below.

Figures of Merit

$$f_T = \frac{1}{2\pi} (\tau_E + \tau_B + \tau_C + \tau_{CC})^{-1}$$

$$f_{\text{max}} = \sqrt{\frac{f_T}{8\pi R_B C_{BC}}}$$

where:

τ_E = Emitter - Charging Time

τ_B = Base Transit Time

τ_C = Collector Transit Time

τ_{CC} = Collector - Charging Time

R_B = Base Resistance

C_{BC} = Base Collector Capacitance

Figure 2

The expected value for f_T is about 200 GHz and about 500 GHz for f_{max} . In order to measure the figures of merit, it was necessary to take the s-parameter readings first. Once you have the s-parameter characterization, f_T and f_{max} can be calculated. The network analyzer used to take the s-parameters can only go up to about 40 MHz. However, an acceptable gain curve that exceeds the network analyzer's capabilities would indicate that the devices are operating properly and further testing can be done.

Results and Discussion:

The test results for the devices were not as expected. The current gain was well below unity at all frequencies. This means that there is something fundamentally wrong with the devices and changes need to be made.

At this point my mentor is trying to figure out exactly what went wrong. Some of the possibilities are that maybe the base is too highly doped ($5 \times 10^{19} \text{ cm}^{-3}$), or maybe it has something to do with the GaAsSb and AlAsSb since these are new materials and they have not been thoroughly studied for our purposes.

In order to advance this project, the problem has to be identified, revisions done to the original design, and new devices grown and tested.

The Dynamic Phase Behavior of a Biological Monolayer System

REU Intern: Kieche Meleson, Chemistry, University of California, Santa Barbara

Principal Investigator: Jacob Israelachvili, Chemical Engineering, UCSB, jacob@engineering.ucsb.edu

Mentor: Yufang Hu, Department of Chemical Engineering, UCSB, yufang@mrl.ucsb.edu

Abstract:

Monolayers are self-assembled thin films at the air-water interface that are one molecule thick. A two-dimensional lipid monolayer provides a simple model system for the study of biological membranes. Here we use a monolayer to investigate the thermodynamic phase behavior of two important lipids: dimyristoylphosphatidylcholine (DMPC) and cholesterol.

Specifically, we are interested in the Ostwald ripening of domains formed in this lipid monolayer. Experiments were performed using a Langmuir-Blodgett trough equipped with a fluorescence microscope to witness the phase separation of the more densely packed domains from the more fluid regions.

Thus far, our observations confirmed that the mean radius of the domains grew larger while the number density of domains decreased over time. This observation is in agreement with theory. Next, we will quantify the rate of ripening using advanced image analysis techniques. Ultimately, we would like to reveal the effect of electrostatic dipole repulsion vs. line tension on the mean radius of these domains.

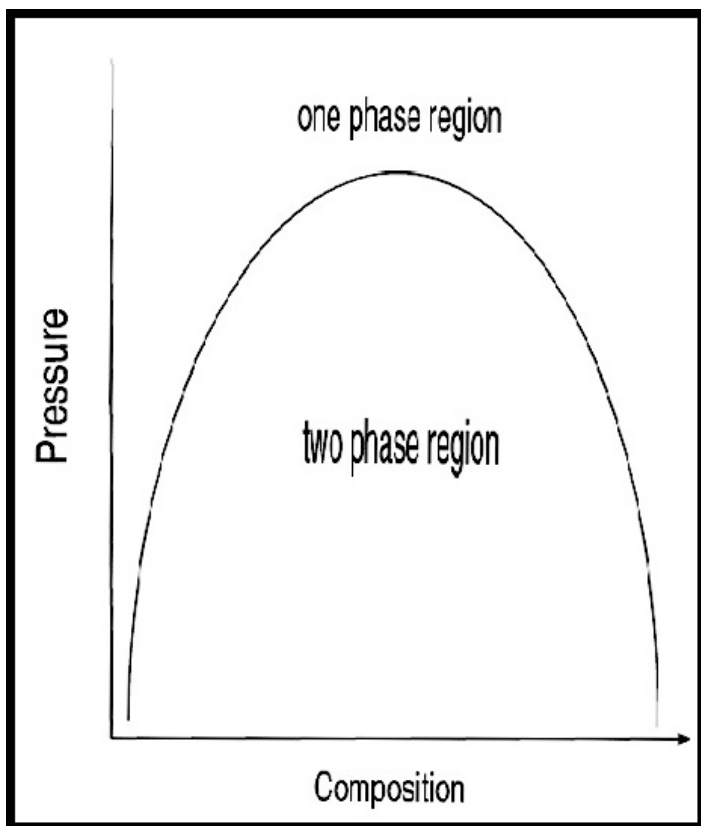


Figure 1: A phase diagram for a binary system.

Introduction:

A phase is defined as uniform thermodynamic properties, such as pressure or temperature. With this definition in mind, Figure 1 illustrates a typical phase diagram for a binary system. By adjusting the pressure at a fixed composition, the system can move from the one-phase region to the two-phase region.

Upon entering the two-phase region, clusters of molecules begin to form. Nucleation of the molecule clusters begins by accretion from the bulk fluid [1]. Domains of the new phase grow as a function of time — smaller phase domains coalesce with the larger ones, resulting in fewer but larger phase domains. The process of phase separation and domain shape and growth are governed by such forces as Brownian motion, line tension and electrostatic dipole repulsion — all of which are described by the theory of Ostwald ripening. The ultimate goal of this experiment is to quantitatively describe this phenomenon for a binary system composed of lipids present in biological membranes.

A nice model for investigating the dynamic phase behavior of such a system is an amphiphilic monolayer film, because it is a simple two-dimensional analogue of more complex structures like cell membranes. We studied the lipid monolayer with a Langmuir-Blodgett trough and fluorescence microscopy.

Experimental Procedure:

A solution of 88.5% molecular weight dimyristoylphosphatidylcholine (DMPC), 10% molecular weight dihydrocholesterol and 1.5% molecular weight of an amphiphilic fluorescent probe called Texas Red was made by dissolving the powder form of the above components in chloroform. Approximately 3.3mL of the solution is placed on the surface of distilled water inside a miniature Langmuir-Blodgett trough by syringe. The trough remained uncovered for 10 minutes to allow the chloroform to evaporate, leaving the monolayer behind.

Image analysis is achieved by fluorescence microscopy — the mini-trough is placed on the stage of the microscope in a dark room and the images are captured by a CCD camera and transferred to a video monitor and VCR.

Once the desired images are recorded, they are then transferred to a software program for image analysis. The program transforms the grayscale areas into a binary image of black and white pixels that can be calculated in order to obtain the mean radius of the domains as well as count how many domains are present in a given frame.

Results:

Although our results are currently incomplete, the phase behavior of the domains appeared to be in agreement with Ostwald ripening. Figure 2 shows a series of images taken from past experiments to demonstrate domain growth over 60 hours. Most of the experiments performed in the past 9 weeks were to develop a protocol for gaining meaningful data.

The fluorescent probe molecule we used for the experiments was old which caused problems such as changing the structure of the domains and bleaching.

Bleaching is apparent when the light areas are not as bright upon initial application and when exposed to any light source, the molecules dim rapidly. A new batch of the fluorescent molecule was ordered and tested too late to include in this report. In addition, a new method for cleaning the trough was utilized due to problems with contaminants, such as lipid residue from prior experiments and impurities in the water container. A test run was performed and proved to be effective.

By trial and error, and looking to past experiments, we developed an experimental method to reduce contaminants and increase video resolution.

Future experiments will allow us to use this method to gain useful data for image analysis. We will also research a method for quantifying the ripening process, by examining the rate of domain growth.

References:

- [1] Adamson, Arthur W., *Physical Chemistry of Surfaces*, (328), 6th Edition, Wiley, New York.

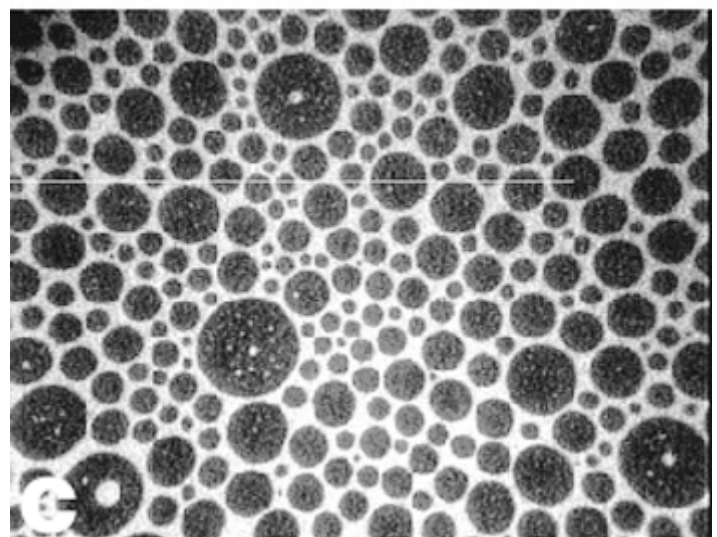
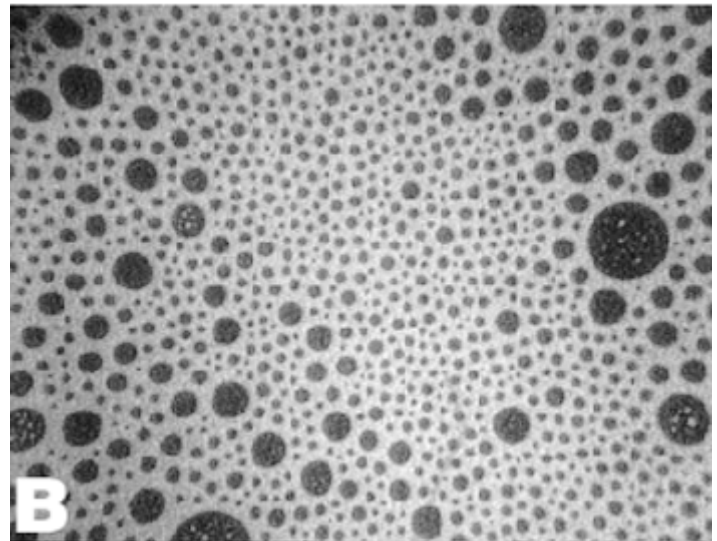
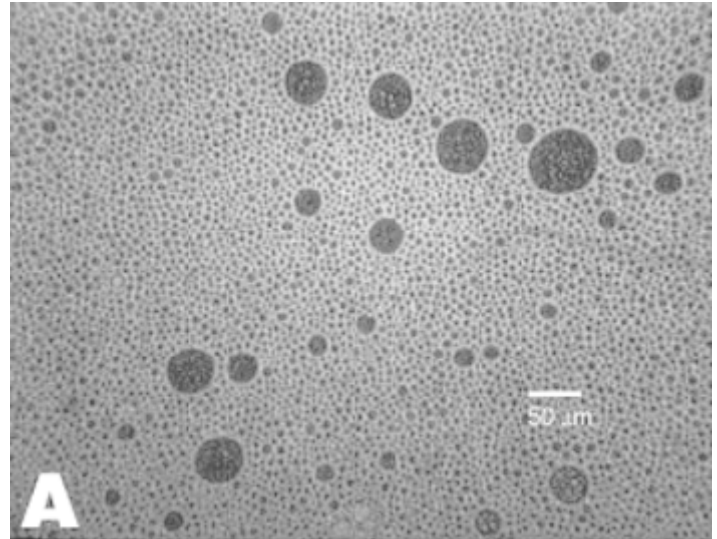


Figure 2:(A) nucleation begins at time0. The dark circular domains are the cholesterol-rich regions while the surrounding white area contains the DMPC-rich region. (B). This image was taken approximately 12 hours later. (C). 60 hours later, it is apparent that the domains are much larger.

400-500 μm Etching of Silicon

REU Intern: Christopher Utley, EE, University of California at Santa Barbara

Principal Investigator: Kimberly Turner, Mechanical Engr, UCSB, turner@engineering.ucsb.edu

Mentor: Rajashree Baskaran, Mechanical Engineering, University of California at Santa Barbara

Abstract:

Controlling the characteristics of side walls in silicon etching while etching deep is very important when building MicroElectro-Mechanical Systems. Using the Plasma Therm Deep Reactive Ion Etcher, it is possible to etch deep into the silicon while controlling the side walls. Initial results show that it is possible to get deep into the wafer while controlling the side walls. The results also show that it will be necessary to use an Oxide mask in order to get deeper than 100 μm .

Introduction:

Current production techniques that are used in the construction of MicroElectroMechanical Systems (MEMS) were developed out of the integrated circuit industry. The problem is that IC's don't gain much from having features that are deep in the silicon. This is not the case with MEMS. Features that extend 400-500 μm in the silicon have the potential for being sensors with greater sensitivity, and actuators that can provide greater forces. Deep features are possible through the use of wet etches, but they are often very slow and it's hard to control the side wall characteristics.

The important side wall characteristics are the angling of the walls and smoothness. The angling can take on three different forms. Tapering occurs when the feature gets smaller at the bottom versus the top. Undercutting is the opposite, the etch makes the feature wider deeper down. Finally, there could be no angling which would give straight side walls.

The machine that is making this possible is the PlasmaTherm Deep Reactive Ion Etcher (DRIE). One benefit of this machine is that it uses two voltage sources to excite the plasma and then directs the plasma to hit the wafer at a 90° angle. This means that most of the energy is used only on removing silicon that is exposed at the horizontal surfaces of the wafer. The second benefit is that the process is actually composed of smaller steps. The entire process used in the DRIE is called the Bosch process. This process switches between etch and a sidewall protective layer deposition. The deposition protects the sidewalls while the rest of the wafer is being etched.

Procedure:

The processing will be done on four inch silicon wafers. Standard photolithography is preformed to transfer the pattern of squares onto the wafer. The test pattern is set up with one set of squares being 64 μm from center to center. The second set has a spacing of 32 μm . Within both of these groups, there are eight groups of squares with varying side wall thicknesses. The side wall thickness was varied from 1 to 5 μm .

Once the pattern is transferred to the photo resist, the Plasma Therm DRIE is used. To examine the results of the etching, the wafers are cleaved and viewed under an optical microscope.

Results:

The first data that was taken, looked at the top of the wafers to see which side walls survived. On every test run the 1 and 1.5 μm side walls were destroyed by the etching. Once the wafers were cleaved, it was possible to look at side wall depth and shape. The deepest etch that was achieved using the photoresist turned out to be about 90 μm . The parameters on the DRIE were varied with the goal of tapering the side walls. The results show tapering until the last five microns where there is a rapid increase in the size of the beam. (Fig 1)



Figure 1

Conclusions:

The last etch that was performed showed that at 100 μm , there was definite tapering in the side walls, and it appeared that they were fairly smooth. In this etch, the photoresist mask was used up. In order to go deeper, it will be necessary to go with an oxide mask. In creating the mask, it would be best to use a plasma reactive etcher since it will give straight side walls. The problem is that the RIE also has a tendency to burn the photoresist. HF is another possibility, but that will have a tendency to undercut the mask and that will really hurt the smaller side walls. Future experiments will look at developing a way to produce a mask that will have a greater selectivity than the current photoresist mask.

Acknowledgements:

I would like to thank the following people for all of their help during the summer: Kimberly Turner, Raji Baskaran, Mike Anzlowar, Bob Hill, the rest of the clean room staff, and all of the summer interns.

this page has intentionally been left blank

Index

A

| | |
|--------------------------------|----|
| Ahle, Karen | 54 |
| Alekseyev, Leonid | 6 |
| Allara, David | 46 |
| Asanbaeva, Anna | 56 |
| Ast, Dieter, | 6 |
| Awschalom, David | 90 |

B

| | |
|------------------------------------|----|
| Badillo Torres, David | 40 |
| Barnes, Amy | 40 |
| Baskaran, Rajashree | 96 |
| Batt, Carl | 12 |
| Björnsson, Per | 72 |
| Blakely, Jack | 22 |
| Brown, Austin | 80 |
| Brown, Kwanza Nicole | 42 |
| Burton, Molly | 8 |

C

| | |
|-------------------------------------|--------|
| Campagnolo, Christine | 12 |
| Cayetano, Van Ortega | 58 |
| Champlain, James | 92 |
| Chang, Kee-Chul | 22 |
| Charles, Steven | 82 |
| Chen, Danny | 6 |
| Clarke, David | 82 |
| Clemens, Bruce | 68 |
| Collins II, Charles A. | 84 |
| Cruz-Rivera, Luis J. | 60 |
| Cuiffi, Joseph D. | 42, 44 |

D

| | |
|----------------------------|----|
| Diallo, Mamadou | 36 |
| Dinh, Nga N. | 44 |
| Douglas, Erik | 62 |

E

| | |
|------------------------|----|
| Esber, Christine | 68 |
| Etzkorn, Ed | 82 |

F

| | |
|--------------------------------|--------|
| Fadgen, William | 46 |
| Felsovalyi, Flora | 10 |
| Fonash, Stephen | 42, 44 |

G

| | |
|--------------------------------|----|
| Gapin, Andrew | 86 |
| Gerardot, Brian | 86 |
| Gordon, Nicarter | 88 |
| Griffin, James | 36 |
| Griffin, Peter B. | 66 |
| Guébels, Nathalie | 90 |
| Guzman, Jesus | 92 |
| Gwinn, Elisabeth | 80 |

H

| | |
|-------------------------------|------------|
| Hanif, Khalid | 84 |
| Harris, Corey | 64 |
| Harris, Gary L. | 30, 34, 36 |
| Harris, James S., Jr. | 54, 74 |
| Harrison, Scott | 66 |
| Hawkins, Tamisha | 30 |
| Hayes, Daniel J. | 42, 44 |
| Haynie, Brendan | 48 |
| Hoff, Jeremy | 12 |
| Hong, Jonathan | 14 |
| Hu, Yufang | 94 |
| Hwang, Jesse | 68 |

I

| | |
|----------------------------|----|
| Israelachvili, Jacob | 94 |
|----------------------------|----|

J

| | |
|----------------------------------|----|
| Johnson, Jevon J. | 48 |
| Johnston-Halperin, Ezekiel | 90 |

K

| | |
|------------------------|----|
| Kawakami, Roland | 90 |
| Kpissay, Armah | 8 |
| Kreutz, Ted | 80 |

L

| | |
|-------------------------------|----|
| Lee, Doohan | 22 |
| Lewis, Andrea N. | 32 |
| Lin, Chien-chung | 74 |

M

| | |
|-------------------------------------|--------|
| Maeda, Wendi | 16 |
| Malliaras, George | 20 |
| McLaughlin, Jenéa | 34 |
| McVittie, James | 70, 76 |
| Meleson, Kieche | 94 |
| Mishra, Umesh | 92 |
| Mitragotri, Samir | 88 |
| Moler, Kathryn A. | 58, 72 |
| Mordovanaki, Aghapi G. | 70 |

| | |
|--------------------------------|-----------|
| N | |
| Neves, Hercules, | 10 |
| Newman, Catherine | 18 |
| Nguyen, Ly | 50 |

| | |
|-------------------------|----|
| O | |
| Ober, Christopher | 26 |
| Oliver, Antonio | 22 |

| | |
|------------------------|----|
| P | |
| Palmer, Andre | 32 |
| Pantano, Carlo G. | 40 |
| Pease, R. Fabian | 60 |
| Petroff, Pierre | 86 |
| Phillips, Mark | 68 |
| Pinguet, Thierry | 54 |
| Plummer, James | 64 |

| | |
|-------------------------------|-----------|
| R | |
| Rodriguez, Sasha | 36 |

| | |
|--------------------------------|-----------|
| S | |
| Saltzman, W. Mark | 14 |
| Schmaljohann, Dirk | 26 |
| Singh, Jogender | 50 |
| Skvarla, Michael | 16 |
| Slinker, Jason | 20 |
| Sogah, Dotsevi | 8 |
| Solomon, Glenn | 74 |
| Soong, Ricky | 10 |
| Speller, Sharelle | 22 |
| Spencer, Michael | 18 |
| Starke, Virginia | 24 |
| Straver, Eric W. J. | 58 |
| Strouse, Geoff | 84 |
| Sui, Jennifer | 26 |
| Sunduram, Jagganathan | 88 |

| | |
|------------------------------|-----------|
| T | |
| Takamura, Yayoi | 64 |
| Taketatsu, Eric | 72 |
| Tan, Jian | 14 |
| Tang, Mary | 56, 62 |
| Tao, Andrea | 74 |
| Tezel, Ahmet | 88 |
| Tiwari, Sandip | 24 |
| Turner, Kimberly | 96 |

| | |
|---------------------------------|-----------|
| U | |
| Utley, Christopher | 96 |

| | |
|------------------------------|-----------|
| W | |
| Walker, Amy | 48 |
| Williams, James | 76 |
| Winograd, Nicholas | 48 |

| | |
|-------------------|----|
| X | |
| Xia, Maggie | 20 |